Competing Phases in Two-Dimensional Quantum Many-Body Systems

by

James M. Murray

A dissertation submitted to The Johns Hopkins University in conformity with the requirements for the degree of Doctor of Philosophy.

Baltimore, Maryland

July, 2013

Abstract

Quantum many-body systems exhibit a wide array of possible ordered phases at low temperatures. In this thesis, several such phases and the transitions between them are theoretically studied in the context of recent experimental results. I first present an investigation of fluctuation phenomena in layered superconductors in high magnetic fields. In order to account for the important effects of coupling between layers, which enhances the superconducting fluctuations and allows for a finite-temperature phase transition, a novel expansion in the number of coupled layers is used. This expansion leads to a two-dimensional effective Ginzburg–Landau theory, which allows for a controlled calculation of thermodynamic and transport properties such as magnetization and conductivity. Next, a microscopic mean-field analysis of the recently synthesized mixed-valency material KNi_2Se_2 is presented. Due to the noninteger number of localized electrons per unit cell and substantial degree of electron interactions, this material exhibits a tendency toward charge ordering, which competes with a heavy-fermion phase exhibiting an enhanced effective electron mass. Beginning from a microscopic Hamiltonian and applying mean-field

ABSTRACT

theory, a reentrant charge-order transition is shown to exist theoretically, in apparent agreement with recent experimental observations. Finally, a renormalization group analysis is applied to the study of competing orders in bilayer graphene. In addition to the previously suggested nematic and antiferromagnetic phases, unconventional superconductivity is shown to arise generically in the presence of a nonzero chemical potential, even for the case where the bare interactions are entirely repulsive. The implications of these results on the general understanding of competition between particle-hole and superconducting orders are discussed in detail.

Primary Reader: Oleg Tchernyshyov

Secondary Reader: N. Peter Armitage

Committee: Howard Katz, Nina Markovic, David Yarkony, Tyrel McQueen (alternate)

Acknowledgments

I would like to begin by thanking Zlatko Tešanović, who served as my advisor until his untimely death last summer. If there's anything worth taking seriously in the work presented here, it's due in large part to his expert guidance and the exceptional example that he set as a physicist during the years that I was his student.

During the last year, a number of others have graciously stepped up as supporters, collaborators, and mentors. Tyrel McQueen, Jamie Neilson, and especially Oleg Tchernyshyov have all gone well beyond the call of duty in their willingness to offer guidance and assistance for issues scientific and otherwise. I have also been fortunate during the past year to develop a fruitful collaboration with Oskar Vafek, whose intense focus and keen insight into the world of physics have made him an extremely valuable collaborator and mentor.

I have benefitted both scientifically and personally from discussions and interactions with many of my fellow students at Hopkins over the years, including Jian Kang, Wei Liu, Valentin Stanev, Yuan Wan, and many others. I also owe a great deal of thanks to our group's two former postdocs: Adrian Del Maestro, who was

a close collaborator during his year at Hopkins and has remained a valuable friend and ally since, and Vladimir Cvetkovic, who was an inspiring late-night presence in the department during my first years as a grad student, and with whom I have been pleased to cross paths again more recently in Tallahassee.

Finally, thanks to my parents and to my siblings—I wouldn't be who I am today without each of you. And thanks especially to Maya for her boundless love and support, and for being a good sport about my thesis beard and everything that it symbolized.

Dedication

To my parents, Michael and Denise,

for setting a fine example and putting family first.

Contents

List of Tables

List of Figures

Chapter 1

Introduction

1.1 The Theory of Everything

As pointed out by Laughlin and Pines [1], the Theory of Everything forming the microscopic basis for nearly all of the physics of everyday human experience can be written in just a couple of lines:

$$i\hbar\frac{\partial}{\partial t}|\psi(t)\rangle = H|\psi(t)\rangle, \tag{1.1}$$

where

$$H = -\sum_i \frac{\hbar^2}{2m}\nabla_i^2 - \sum_\alpha \frac{\hbar^2}{2M_\alpha}\nabla_\alpha^2 + \sum_{i,j}\frac{e^2}{|r_i - r_j|^2} + \sum_{\alpha,\beta}\frac{Z_\alpha Z_\beta e^2}{|R_\alpha - R_\beta|^2} + \sum_{i,\alpha}\frac{Z_\alpha e^2}{|r_i - R_\alpha|^2}. \tag{1.2}$$

The above equations describe the motions and interactions of electrons at positions r_i and atomic nuclei at positions R_α. The other parameters are the masses of the electrons and nuclei (m and M_α, respectively), as well as their corresponding electric charges (e and $Z_\alpha e$). While these equations may not include the effects of gravity, nuclear reactions, or

a handful of other exotic phenomena that become relevant in studying cosmology or high-energy collisions in particle accelerators, they are perfectly sufficient for the description of ordinary solids, liquids, and gasses.

If the physicist's only job were to deduce the fundamental equations governing physical laws, then, after writing down (1.1) and (1.2), many of us would have little left to do but turn to elementary particle theory or device engineering. However, we know from experience that such extreme reductionism is not necessarily the appropriate view. In particular, by considering a larger and larger number of interacting particles, one finds that they can together display new, *emergent* behaviors that cannot be deduced from the properties of any single particle. In his famous essay "More is Different," Anderson sums up this idea neatly [2]: "The ability to reduce everything to simple fundamental laws does not imply the ability to start from those laws and reconstruct the universe."

In addition to underlying chemistry and ultimately human life, the equations (1.1) and (1.2) form a basis for a number of emergent, quantum phases of matter, including all of those studied in this thesis. Examples of such phases are superconductivity, in which electrons form pairs with one another and develop macroscopic quantum phase coherence, leading to phenomena such as perfect electrical conductivity and the expulsion of magnetic fields; magnetic phases, in which electron spins spontaneously align or anti-align along a particular direction; and charge ordering, in which electrons avoid repulsion with one another by organizing themselves into a spatially repeating pattern. Generally, such phases are realized only below a certain critical temperature, which can range from above room temperature (as in the antiferromagnetic phase of the cuprate superconductors) to nanoKelvin

scales (as in the superfluid phase of cold atomic gasses). In addition to temperature, a number of other parameters can be varied to further characterize a physical system, including electric and magnetic fields, applied pressure, and chemical doping.

The role of the experimentalist is thus clear: by studying the experimental response of a material to variations in such parameters, much can be learned about the nature of the material and the effects of interactions between the constituent particles. What, then, is the role of the theorist, given that the fundamental equations (1.1) and (1.2) are already known? The basic difficulty stems from the fact that, while these equations are perfectly complete and accurate, they become hopelessly complicated for any physical system consisting of more than just a few particles. The theorist's task is therefore to develop and apply a framework for understanding the important properties of a physical system in a way that distills the important aspects while ignoring many of the details that lead to unnecessary complication.

The remainder of this Introduction reviews the key aspects of three such paradigmatic frameworks for describing the collective behaviors of many-body quantum systems, all of which have been applied widely to various problems in condensed matter physics over the years. In Section 1.2, the phenomenological approach of Ginzburg and Landau is reviewed. In Section 1.3, we discuss the microscopic mean-field approach, presenting the BCS theory of superconductivity as a canonical example. Finally, in Section 1.4 we review the renormalization group approach. These three formalisms will then be applied in modelling the physical properties of existing materials in the remaining chapters of this thesis.

1.2 The Ginzburg–Landau approach: Effective field theory

First introduced in 1950, the phenomenological theory proposed by Ginzburg and Landau (GL) [3] has since become a paradigm for thinking about the role of symmetry and competing phases in physics. Although the theory was originally proposed to explain superconductivity, the effective field theory approach is much more general and can be readily applied to a wide array of other phenomena in condensed matter physics, such as magnetism and nematic phases. Here we shall focus exclusively on the application of GL theory to superconductivity, which was the original context in which the theory was proposed. The results of the GL theory of superconductivity presented here will be applied in Chapter 2 to the study of fluctuation phenomena in superconductors in strong magnetic fields.

1.2.1 The Ginzburg–Landau free energy

The phenomenological GL theory predated the microscopic theory of superconductivity by several years. Lacking a detailed picture of precisely what the electrons in a superconductor are up to, Ginzburg and Landau were nonetheless able to make a great deal of progress by postulating that the superconductivity could be described by a complex *order parameter* $\psi(x)$, with $|\psi(x)|^2$ being proportional to the density of superconducting electrons.[1] It is further assumed that the free energy can be expressed as a power series in

[1] Due to the fact that the superconducting order parameter is not a gauge-invariant quantity, the question of whether a local order parameter can be defined at all is rather subtle [4]. With a proper choice of gauge and under appropriate conditions, however, it can be shown rigorously that the usual notions of spontaneous symmetry breaking, as described by the GL theory, apply to superconductivity [5].

the order parameter, coupled to an electromagnetic vector potential:

$$F = F_0 + \int d^d x \left[\frac{1}{2m^*} \left| \left(-i\hbar\nabla - \frac{e^*}{c}\mathbf{A} \right) \psi(x) \right|^2 + \alpha|\psi(x)|^2 + \frac{\beta}{2}|\psi(x)|^4 + \frac{1}{8\pi}|\nabla \times \mathbf{A}|^2 \right] \quad (1.3)$$

Equation (1.3) defines an effective field theory, which is characterized by the phenomenological coefficients α and β, as well as the effective mass m^* and charge e^*. All of these parameters are *a priori* unknown, but can in principle be fixed by either relating quantities calculated within GL theory to experimental measurements, or deriving GL theory from the microscopic BCS theory, as was first done by Gor'kov in 1959 [6].

One of the greatest advantages of the GL approach versus calculations from a microscopic Hamiltonian is the relative ease with which it can be applied to problems in which the order parameter is spatially varying. In order to see this, consider the full equations obtained by varying (1.3) with respect to ψ^* and $\mathbf{A}$:

$$0 = \frac{1}{2m^*} \left(-i\hbar\nabla - \frac{e^*}{c}\mathbf{A} \right)^2 \psi + \alpha\psi + \beta|\psi|^2\psi \quad (1.4)$$

$$0 = -\frac{e^{*2}}{m^*c^2}|\psi|^2\mathbf{A} + \frac{i\hbar e^*}{2m^*c}(\psi\nabla\psi^* - \psi^*\nabla\psi) - \frac{1}{4\pi}\nabla \times \nabla \times \mathbf{A}. \quad (1.5)$$

A great deal can be deduced about the phenomenology of superconductors just from these two equations. For instance, in the absence of spatial gradients and magnetic field, (1.4) can easily be minimized to give $|\psi_0|^2 = 0$ for $\alpha > 0$, and $|\psi_0|^2 = -\alpha/\beta$ for $\alpha < 0$. The quantity $|\psi|^2$ is proportional to the superfluid density, and since the presence of superconductivity depends on the sign of α in this way, we infer that $\alpha \sim T - T_c$, where T_c is the critical temperature of the superconductor.

Suppose that the superfluid density can be taken to be arbitrarily small, as may happen at a domain boundary or near the upper critical magnetic field at which super-

conductivity is destroyed. In this case, the last term in (1.4) may be ignored, and again neglecting the vector potential, the equation becomes

$$\nabla^2\psi = \frac{2m^*\alpha}{\hbar^2}\psi, \tag{1.6}$$

which makes it convenient to define the characteristic length

$$\xi \equiv \frac{\hbar}{\sqrt{2m^*|\alpha|}}. \tag{1.7}$$

The quantity ξ is known as the *coherence length*, and gives a measure of the typical distance over which the superfluid density changes appreciably.

Another intrinsic length scale characterizing a superconductor can be obtained from the second variational equation (1.5). Taking the curl of this equation and using $\nabla \times \mathbf{A} = \mathbf{B}$, this equation becomes

$$\nabla^2\mathbf{B} = \frac{4\pi e^{*2}}{m^*c^2}|\psi|^2\mathbf{B}. \tag{1.8}$$

This equation underlies the Meissner effect, the defining property of a superconductor, according to which a magnetic field is screened exponentially from the bulk of a superconducting sample. The length associated with this screening is known as the *penetration depth*:

$$\lambda = \left(\frac{m^*c^2}{4\pi e^{*2}|\psi_0|^2}\right)^{1/2}, \tag{1.9}$$

where it has been assumed that $|\psi|^2 \approx |\psi_0|^2$ takes approximately its bulk value.

1.2.2 Superconductors in high magnetic fields

The behavior of a superconductor in a magnetic field depends in a crucial way on the Ginzburg–Landau parameter $\kappa \equiv \lambda/\xi$ associated with that superconductor. For

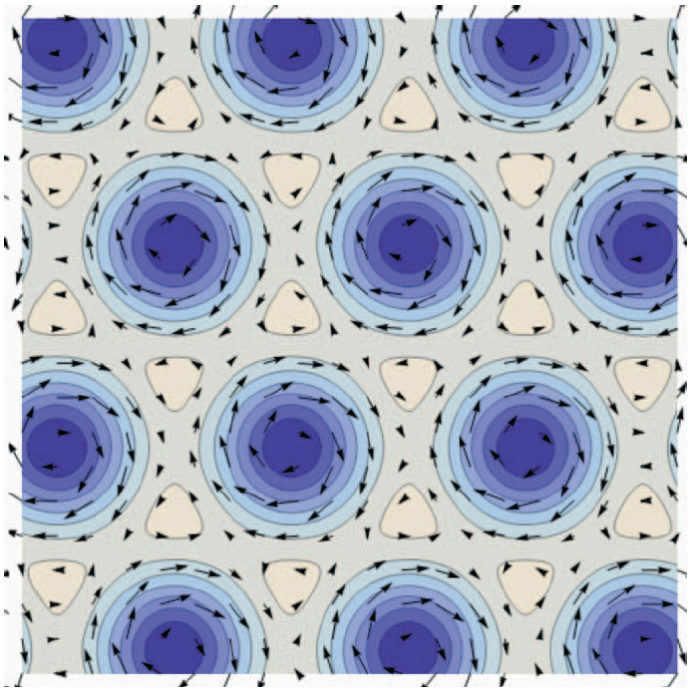

Figure 1.1: Contour plot showing superfluid density, which vanishes at the vortex cores, in the Abrikosov vortex lattice phase. Arrows show the direction of circulating supercurrent.

$\kappa < 1/\sqrt{2}$—so-called type-I materials—the magnetic field is completely expelled from the superconductor except where it penetrates to a distance $\sim \lambda$ at the sample edges. For type-II materials in which $\kappa > 1/\sqrt{2}$, on the other hand, the magnetic field penetrates the bulk of the sample in quantized bundles of flux, with superconducting vortices forming at these locations, as shown in Figure 1.1.[2] These vortices are the primary degrees of freedom for a type-II superconductor in a magnetic field, fluctuating due to their thermal energy, and repelling one another due to electromagnetic interaction. At sufficiently high fields and low temperatures, the vortices form a periodic lattice, as first described by Abrikosov [7]. All of the high-temperature superconductors that have been discovered so far, including

[2]The basic reason for the difference is that, due to the fact that ξ is relatively smaller in type-II superconductors, the superconductor does not lose too much condensation energy by allowing the magnetic field to penetrate, so it is energetically less costly to allow vortices than to force the magnetic field out of the entire sample.

the iron-based superconductors studied in Chapter 2, have been members of the type-II family, and henceforth we shall focus our attention on these materials. Much of the analysis in Chapter 2 will involve the study of type-II superconductors in high magnetic fields. In order to set the stage, we derive here some basic results that shall be relevant later on.

Supposing that we are sufficiently near the upper critical magnetic field at which superconductivity disappears, and focusing on the case of $d = 2$ spatial dimensions, we can linearize the GL equation (1.4) as before:

$$\begin{aligned} 0 &= \frac{1}{2m^*}\left[\left(-i\hbar\nabla - \frac{e^*}{c}\mathbf{A}\right)^2 - \frac{\hbar^2}{\xi^2}\right]\psi(x,y) \\ &= \left[-\frac{\hbar^2}{2m^*}\frac{d^2}{dx^2} + \frac{m^*}{2}\left(\frac{e^*H}{m^*c}\right)^2\left(x - \frac{ck_y}{e^*H}\right)^2 - \frac{\hbar^2}{2m^*\xi^2}\right]\psi(x), \end{aligned} \tag{1.10}$$

where it has been assumed that $\mathbf{A} = (0, Hx, 0)$, corresponding to a magnetic field in the z-direction, and that $\psi(x,y) = e^{ik_y y}\psi(x)$. Recognizing (1.10) as just the one-dimensional harmonic oscillator equation with frequency $\omega_c = e^*H/m^*c$ and coordinate shifted by $x_0 = ck_y/e^*B$, we can read off the solution as

$$\frac{\hbar^2}{2m^*\xi^2} = \hbar\omega_c(n + \frac{1}{2}), \tag{1.11}$$

with $n = 0, 1, 2, \ldots$. This is the familiar Landau level spectrum for the quantum mechanics problem of a charged particle in a magnetic field.[3] Evidently, the largest possible field $H = H_{c2}$ that still provides a solution to (1.11) occurs for $n = 0$ and is given by

$$H_{c2} = \frac{\phi_0}{2\pi\xi^2}, \tag{1.12}$$

where $\phi_0 = hc/2e$ is the flux quantum, which is the amount of magnetic flux penetrating a single vortex (it has been assumed that $e^* = 2e$, corresponding to the effective charge of

[3]Though it may seem unphysical that solutions should exist only for *discrete* values of magnetic field, this is in fact an artifact of our linearization of the problem. Once the quartic term is included, it is found that solutions exist for any value of magnetic field below H_{c2} [8].

a Cooper pair of superconducting electrons). Since ξ^2 is roughly the size of a single vortex core, (1.12) tells us that superconductivity disappears once the vortices become so dense that they begin to overlap.

In Chapter 2 we shall make the approximation that only the lowest Landau level (LLL) is occupied. In order for this to be the case, the thermal energy must be small compared to the excitation energy to the second Landau level, i.e. $T \ll \hbar\omega_c$ (throughout this thesis we shall use units in which the Boltzmann constant $k_B = 1$). Recalling that $\xi^{-2} \sim T - T_c$, the LLL ($n = 0$) condition from (1.11) can be written as

$$0 = t + h - 1, \tag{1.13}$$

where we have defined $h = H/H_{c2}(0)$ as the magnetic field normalized by the upper critical field at $T = 0$, as well as $t = T/T_c$. From (1.13) and the above arguments it is clear that a superconducting solution can only exist for $t + h < 1$, so that this equation defines the superconducting-to-normal phase boundary in the LLL approximation. Thus, assuming that the magnetic field is sufficiently large such that the higher-energy Landau levels can be projected out, the effective free energy in the LLL approximation can be written as

$$F = \int d^2x \left[\alpha_0(t + h - 1)|\psi|^2 + \frac{\beta}{2}|\psi|^4\right]. \tag{1.14}$$

If we wish to include fluctuations of the order parameter in our theory, we can do so by defining the partition function as

$$Z = \int D(\bar{\psi}, \psi) e^{-S[\bar{\psi},\psi]}, \tag{1.15}$$

where the action is given in this case by

$$S[\bar{\psi}, \psi] = \frac{1}{T} \int d^2x \left[\alpha_0(t + h - 1)|\psi|^2 + \frac{\beta}{2}|\psi|^4\right]. \tag{1.16}$$

The functional integration in (1.15) indicates that all possible configurations of the field ψ are integrated over, with those configurations minimizing the action contributing the most to the partition function. The free energy is then given by $F = -T \ln Z$, and we see that we recover our earlier result (1.14) in the case that the fields assume their mean-field values, i.e. when fluctuation effects are small. Fluctuation effects will in general be important, however, in the critical region of the phase diagram, defined by (1.13). The action given in (1.16) will serve as our starting point in describing fluctuation effects in layered superconductors in strong magnetic fields in Chapter 2.

1.3 The Hartree–Fock approach: Microscopic mean-field theory

While the GL theory described in the previous section is extremely successful in describing many phenomenological aspects of various low-temperature phases, it fails to provide an understanding of how and why the underlying particles form these phases in the first place. In order to gain such an understanding, one would like to begin from a Hamiltonian describing the particles and their interactions, along the lines of the Theory of Everything (1.2) described above. Although solving such a Hamiltonian exactly is an impossible task for all but the very smallest systems, a number of shrewd approximations can be employed to make the problem more tractable, for example exploiting the smallness of the interactions if the system is weakly coupled. Such approaches can often lead to models with remarkable quantitative accuracy.

In this section we outline the Hartree–Fock approach for electronic systems, in which each electron, rather than interacting directly with other individual electrons, instead

interact with a *mean field* created by the other electrons. This approach can be applied to many types of electronic systems, with different mean fields corresponding to different types of ordered phases. For example, the mean field in a ferromagnet is the average effective magnetic field experienced by each electron, while the mean field in a charge-ordered phase is the staggered charge density. Here we outline perhaps the most successful application of Hartree–Fock to many-body physics: the theory of superconductivity proposed in 1957 by Bardeen, Cooper, and Schrieffer [9,10]. In this theory, the role of the mean field is played by the superconducting condensate, which, as shown by Gor'kov [6] soon after the BCS theory was introduced, is proportional to the GL order parameter ψ that was described in Section 1.2. In addition to providing an underpinning for the GL theory used to describe layered superconductors in Chapter 2, a Hartree–Fock approach analogous to the one presented here will be used to describe various types of non-superconducting phases in the material KNi_2Se_2 in Chapter 3. The BCS theory shall also make a reappearance (this time recast in the language of quantum field theory) in the description of d-wave superconductivity in the bilayer honeycomb lattice studied in Chapter 4.

Let us consider a Hamiltonian describing electrons with an attractive contact interaction:

$$H = \sum_{\mathbf{k}\sigma} \varepsilon_{\mathbf{k}} c^\dagger_{\mathbf{k}\sigma} c_{\mathbf{k}\sigma} - \frac{g}{V} \sum_{\mathbf{k},\mathbf{k}',\mathbf{q}} c^\dagger_{\mathbf{k}+\mathbf{q},\uparrow} c^\dagger_{-\mathbf{k},\downarrow} c_{-\mathbf{k}'+\mathbf{q},\downarrow} c_{\mathbf{k}',\uparrow}, \tag{1.17}$$

where $\varepsilon_{\mathbf{k}}$ gives the energy of a non-interacting electron with momentum $\mathbf{k}$, V is the system volume, and $g > 0$ describes the strength of the attractive interaction. In the original formulation of BCS theory, the attraction is an effective interaction mediated by a distortion of the positively charged lattice ions. A question of great current interest is the possibility

that purely repulsive interactions can also give rise to superconductivity—an issue that we take up in our study of the bilayer honeycomb model in Chapter 4. For the time being, however, we shall simply assume that an attractive interaction exists and work out the consequences.

The physical picture in BCS theory is that of electrons in time-reversed states (i.e. having opposite momentum and spin) from one another forming "Cooper pairs." These bosonic composite objects then condense into their ground state at temperatures below the critical temperature T_c. Let us begin by *assuming* that the following expectation value is nonzero in the superconducting phase:

$$\begin{aligned} \Delta &\equiv g\langle\Omega|c_{i\downarrow}c_{i\uparrow}|\Omega\rangle \\ &= \frac{g}{V}\sum_{\mathbf{k}}\langle\Omega|c_{-\mathbf{k}\downarrow}c_{\mathbf{k}\uparrow}|\Omega\rangle, \end{aligned} \tag{1.18}$$

where $|\Omega\rangle$ is the ground state wave function. We shall then proceed to justify our assumption by showing that the ground-state energy is lower in the superconducting ($\Delta \neq 0$) phase relative to the free electron gas. The mean field Δ is the superconducting order parameter (i.e. it vanishes outside of the superconducting phase and is nonzero inside of it), and is proportional to ψ from the GL theory introduced in Section 1.2.

In order to implement the mean-field approximation, let

$$\sum_{\mathbf{k}} c_{-\mathbf{k}+\mathbf{q}\downarrow}c_{\mathbf{k}\uparrow} = \frac{V}{g}\Delta + \underbrace{\sum_{\mathbf{k}} c_{-\mathbf{k}+\mathbf{q}\downarrow}c_{\mathbf{k}\uparrow} - \frac{V}{g}\Delta}_{\delta}. \tag{1.19}$$

We then expect that, if (1.18) is indeed the correct mean field and fluctuations are not too large, then δ should be small. We can then substitute (1.19) into the BCS Hamiltonian (1.17) and keep terms only up to linear order in δ. Including the chemical potential μ, this

leads to the following mean-field Hamiltonian:

$$H - \mu N = \sum_{\mathbf{k}\sigma} \xi_{\mathbf{k}} c^\dagger_{\mathbf{k}\sigma} c_{\mathbf{k}\sigma} - \sum_{\mathbf{k}} (\Delta^* c_{-\mathbf{k}\downarrow} c_{\mathbf{k}\uparrow} + \Delta c^\dagger_{\mathbf{k}\uparrow} c^\dagger_{-\mathbf{k}\downarrow}) + \frac{V}{g}|\Delta|^2. \tag{1.20}$$

Here we have defined $\xi_{\mathbf{k}} \equiv \varepsilon_{\mathbf{k}} - \mu$.

Being bilinear in electron operators, (1.20) can be readily diagonalized. This is most easily accomplished by introducing the Nambu spinor:

$$\Psi_{\mathbf{k}} = \begin{pmatrix} c_{\mathbf{k}\uparrow} \\ c^\dagger_{-\mathbf{k}\downarrow} \end{pmatrix}, \tag{1.21}$$

in which case (1.20) can be written in matrix form:

$$H - \mu N = \sum_{\mathbf{k}} \Psi^\dagger_{\mathbf{k}} \begin{pmatrix} \xi_{\mathbf{k}} & -\Delta \\ -\Delta^* & -\xi_{\mathbf{k}} \end{pmatrix} \Psi_{\mathbf{k}} + \frac{V}{g}|\Delta|^2 \tag{1.22}$$

This equation can be diagonalized via a unitary Bogoliubov transformation. Let

$$U_{\mathbf{k}} = \begin{pmatrix} \cos\theta_{\mathbf{k}} & \sin\theta_{\mathbf{k}} \\ \sin\theta_{\mathbf{k}} & -\cos\theta_{\mathbf{k}}, \end{pmatrix}, \tag{1.23}$$

which satisfies the unitary condition $U^\dagger_{\mathbf{k}} U_{\mathbf{k}} = \mathbf{1}$. Now define new fermionic operators as

$$\begin{pmatrix} \gamma_{\mathbf{k}\uparrow} \\ \gamma^\dagger_{-\mathbf{k}\downarrow} \end{pmatrix} = U_{\mathbf{k}} \Psi_{\mathbf{k}}. \tag{1.24}$$

It can be checked that this transformation preserves the fermionic anticommutation relations, i.e. $\{c_{\mathbf{k}\sigma}, c^\dagger_{\mathbf{k}'\sigma'}\} = \delta_{\mathbf{k}\mathbf{k}'}\delta_{\sigma\sigma'} \Rightarrow \{\gamma_{\mathbf{k}\sigma}, \gamma^\dagger_{\mathbf{k}'\sigma'}\} = \delta_{\mathbf{k}\mathbf{k}'}\delta_{\sigma\sigma'}$. We can choose $\theta_{\mathbf{k}}$ such that the Hamiltonian matrix is diagonalized:

$$U_{\mathbf{k}} \begin{pmatrix} \xi_{\mathbf{k}} & -\Delta \\ -\Delta^* & -\xi_{\mathbf{k}} \end{pmatrix} U^\dagger_{\mathbf{k}} = \begin{pmatrix} E_{\mathbf{k}} & 0 \\ 0 & -E_{\mathbf{k}} \end{pmatrix}, \tag{1.25}$$

which occurs for

$$\begin{aligned} \cos 2\theta_{\mathbf{k}} &= \frac{\xi_{\mathbf{k}}}{E_{\mathbf{k}}} \\ \sin 2\theta_{\mathbf{k}} &= \frac{-\Delta}{E_{\mathbf{k}}}, \end{aligned} \tag{1.26}$$

where the energy eigenvalues are

$$E_{\mathbf{k}} = \sqrt{\xi_{\mathbf{k}}^2 + \Delta^2}. \tag{1.27}$$

The transformed Hamiltonian thus becomes

$$H - \mu N = \sum_{\mathbf{k},\sigma} E_{\mathbf{k}} \gamma_{\mathbf{k}\sigma}^\dagger \gamma_{\mathbf{k}\sigma} + \sum_{\mathbf{k}} (\xi_{\mathbf{k}} - E_{\mathbf{k}}) + \frac{V}{g} |\Delta|^2. \tag{1.28}$$

The quasiparticle excitations created by the fermionic operator $\gamma_{\mathbf{k}\sigma}^\dagger$ are superpositions of electron and hole excitations. Since $E_{\mathbf{k}} > 0$, the energy cost to create one of these excitations is positive, and we conclude that $\langle \gamma_{\mathbf{k}\sigma}^\dagger \gamma_{\mathbf{k}\sigma} \rangle = 0$ in the ground state, which is satisfied uniquely by the famous BCS wave function:

$$|\Omega\rangle = \prod_{\mathbf{k}} \gamma_{-\mathbf{k}\downarrow} \gamma_{\mathbf{k}\uparrow} |0\rangle \sim \prod_{\mathbf{k}} (\cos\theta_{\mathbf{k}} - \sin\theta_{\mathbf{k}} c_{-\mathbf{k}\downarrow}^\dagger c_{\mathbf{k}\uparrow}^\dagger)|0\rangle, \tag{1.29}$$

where $|0\rangle$ is the vacuum state for the fermionic operators, satisfying $c_{\mathbf{k}\sigma}|0\rangle = 0$. The energy of the superconducting ground state is thus given by the last two terms in (1.28), and it is straightforward to show that this is lower than the energy of the Fermi gas without superconductivity, $E_0 = 2\sum_{\mathbf{k}} \xi_{\mathbf{k}}$, indicating that the superconducting phase is stable.

Finally, by returning to the definition of Δ in (1.18), expressing the original fermionic operators $c_{\mathbf{k}\sigma}$ in terms of the quasiparticle operators $\gamma_{\mathbf{k}\sigma}$, and using the fact that $\gamma_{\mathbf{k}\sigma}|\Omega\rangle = 0$, we obtain the following self consistency relation (the so-called "gap equation")

determining the value of Δ:

$$\begin{aligned}\Delta &= -\frac{g}{V}\sum_{\mathbf{k}}\sin\theta_{\mathbf{k}}\cos\theta_{\mathbf{k}} \\ &= \frac{g}{2V}\sum_{\mathbf{k}}\frac{\Delta}{\sqrt{\xi_{\mathbf{k}}^2+\Delta^2}} \\ &= \frac{g}{2}\int_{-\omega_D}^{\omega_D} d\xi \frac{\nu(\xi)\Delta}{\sqrt{\xi^2+\Delta^2}}.\end{aligned} \tag{1.30}$$

Here $\nu(\xi)$ is the density of states for the noninteracting system, and the integral is cut off by the characteristic phonon frequency ω_D. This equation can be generalized to finite temperature by noting that the fermionic quasiparticle states are occupied according to $\langle\gamma_{\mathbf{k}\sigma}^\dagger\gamma_{\mathbf{k}\sigma}\rangle = n_F(E_{\mathbf{k}})$, where $n_F(\epsilon) = 1/(1+e^{\epsilon/T})$ is the Fermi distribution function. In this case (1.30) becomes

$$\Delta = \frac{g}{2}\int_{-\omega_D}^{\omega_D} d\xi \frac{\nu(\xi)\Delta}{\sqrt{\xi^2+\Delta^2}}\tanh\left(\frac{\sqrt{\xi^2+\Delta^2}}{2T}\right). \tag{1.31}$$

In addition to the trivial solution $\Delta = 0$, which occurs for $T > T_c$, this equation can be solve approximately or numerically to obtain a nontrivial solution $\Delta(T)$ for $T < T_c$.

The procedure outlined above for the mean-field description of superconductors will be employed in much the same way, generalized to include multiple species of fermions and different types of order, in Chapter 3, where we investigate charge order and heavy-fermion behavior in the material KNi_2Se_2.

1.4 The Wilson approach: Renormalization group

The first explorations of the renormalization group (RG) concept were made by Stueckelberg and Petermann [11] and Gell-Mann and Low [12]. The problem that these

researchers were addressing was that of ultraviolet divergences in various physical quantities calculated within the framework of quantum field theory. The solution that they discovered was to cut off all divergences by an arbitrary momentum Λ, and then to take the couplings in the theory to be functions of this cutoff. These couplings $\alpha(\Lambda)$ are then chosen in a way such that all of the divergences are cancelled out when physical quantities (e.g. scattering cross-sections) are calculated. Quantum field theories for which this procedure can be successfully applied are known as *renormalizable*, with quantum electrodynamics being a canonical example of such a theory.

The more modern view of the RG was developed in large part by Wilson [13, 14] in the early 1970s. Rather than eliminating ultraviolet divergences from quantum field theories, the Wilsonian version of the RG instead took this cutoff seriously and proceeded to focus on the low-energy, long-wavelength behavior of a system. The basic idea is to systematically eliminate the high-energy modes of a system, thereby arriving at a low-energy effective theory, where the parameters of this effective theory depend in some way on the high-energy fluctuations that were integrated out. In Chapter 4 this program will be applied to the study of competing phases of fermions on the bilayer honeycomb lattice. Below we illustrate the procedure in the relatively simple context of a single bosonic field, which allows us to establish the important aspects of the RG framework while avoiding many of the technical complications that arise in fermionic systems.

1.4.1 Field theory formulation of the renormalization group

In this section we outline the general RG procedure in the language of quantum field theory, illustrating how large-momentum degrees of freedom are integrated out to yield

an effective low-energy theory. Although the procedure illustrated in this section is valid for both bosonic and fermionic theories, for concreteness we can consider a bosonic field theory defined by the following action for a complex scalar field φ in $d+1$ spacetime dimensions:

$$S[\bar{\varphi},\varphi] = \int d^{d+1}x \left[|\partial\varphi(x)|^2 + r|\varphi(x)|^2 + \frac{g}{2}|\varphi(x)|^4 \right], \tag{1.32}$$

where, for simplicity, the theory is assumed to be Lorentz invariant. The coordinates are given by $x = (\tau, \mathbf{x})$, where $\tau = it$ denotes imaginary time. In momentum space, the above action can be written as $S[\bar{\varphi},\varphi] = S_0[\bar{\varphi},\varphi] + S_{\text{int}}[\bar{\varphi},\varphi]$, where

$$S_0[\bar{\varphi},\varphi] = \int^{\Lambda} \frac{d^{d+1}k}{(2\pi)^{d+1}} (k^2 + r)|\varphi(k)|^2 \tag{1.33}$$

and

$$S_{\text{int}}[\bar{\varphi},\varphi] = \frac{g}{2} \int_{1234}^{\Lambda} \bar{\varphi}(1)\bar{\varphi}(2)\varphi(3)\varphi(4). \tag{1.34}$$

In these equations, the upper integration limit Λ indicates that we are only integrating over momenta with magnitude less than this UV cutoff. In the interaction term, we have defined the shorthand $\varphi(i) = \varphi(k_i)$, as well as

$$\int_{1234}^{\Lambda} \equiv \int^{\Lambda} \prod_{i=1}^{4} \frac{d^{d+1}k_i}{(2\pi)^{d+1}} \delta(k_1 + k_2 - k_3 - k_4). \tag{1.35}$$

In order to carry out the RG, we separate the momenta into "fast" and "slow" modes by letting

$$\varphi(k) = \varphi_s(k) + \varphi_f(k), \tag{1.36}$$

where $\varphi_s(k)$ has support (i.e. is nonzero) only for $0 < |k| < e^{-l}\Lambda$, and $\varphi_f(k)$ has support only for $e^{-l}\Lambda < |k| < \Lambda$, with $l > 0$. The noninteracting part of the action then separates

into a slow piece and a fast piece:

$$\begin{aligned} S_0[\bar{\varphi},\varphi] &= S_0[\bar{\varphi}_s,\varphi_s] + S_0[\bar{\varphi}_f,\varphi_f] \\ &\equiv S_0[s] + S_0[f]. \end{aligned} \tag{1.37}$$

Note that there is no mixing term $\sim \bar{\varphi}_s\varphi_f$, since such a term vanishes for both fast and slow momenta. The interacting part of the action meanwhile becomes

$$S_{\rm int}[\bar{\varphi},\varphi] = S_{\rm int}[s] + S_{\rm int}[f] + S_{\rm int}[s,f], \tag{1.38}$$

where the term mixing slow and fast modes is, upon rearranging momentum indices,

$$S_{\rm int}[s,f] = 2g\int_{1234}^{\Lambda} \bar{\varphi}_s(1)\varphi_s(2)\bar{\varphi}_f(3)\varphi_f(4). \tag{1.39}$$

[Looking ahead to the fact that we will be interested in the expectation value of (1.39), we have ignored terms containing an odd number of fast modes, as well as the term of the form $\sim (\bar{\varphi}_s\bar{\varphi}_s\varphi_f\varphi_f + c.c.)$, since these terms will vanish by symmetry.]

In calculating any physical observables, the chief object of interest will be the partition function:

$$\begin{aligned} Z &= \int D(\bar{\varphi},\varphi)e^{-S[\bar{\varphi},\varphi]} \\ &= \int D(\bar{\varphi}_s,\varphi_s)e^{-S_0[s]-S_{\rm int}[s]}\int D(\bar{\varphi}_f,\varphi_f)e^{-S_0[f]-S_{\rm int}[f]-S_{\rm int}[s,f]}. \end{aligned} \tag{1.40}$$

Let us define the expectation value over fast modes:

$$\langle\ldots\rangle_f = \frac{\int D(\bar{\varphi}_f,\varphi_f)(\ldots)e^{-S_0[f]}}{\int D(\bar{\varphi}_f,\varphi_f)e^{-S_0[f]}}. \tag{1.41}$$

We shall also make use of the cumulant expansion:

$$\langle e^{-S}\rangle = e^{-\langle S\rangle + \frac{1}{2}\left(\langle S^2\rangle - \langle S\rangle^2\right)+\ldots}, \tag{1.42}$$

which can be verified by Taylor expanding both sides of (1.42) and matching the terms at each order.

Using (1.41) and (1.42), we find that, to second order in the cumulant expansion, the partition function (1.40) becomes

$$Z \approx \int D(\bar{\varphi}_s, \varphi_s) e^{-S_0[s]-S_{\rm int}[s]-\delta S[s]} \int D(\bar{\varphi}_f, \varphi_f) e^{-S_0[f]-S_{\rm int}[f]}, \tag{1.43}$$

where the modification to the low-energy effective action that comes from integrating out the fast modes is given by

$$\delta S[s] = \langle S_{\rm int}[s,f] \rangle_f - \frac{1}{2} \left(\langle S_{\rm int}^2[s,f] \rangle_f - \langle S_{\rm int}[s,f] \rangle_f^2 \right) + \ldots . \tag{1.44}$$

In most cases, the second integral in (1.43) can be ignored since it just adds an overall constant to the free energy. The interesting part of (1.43) is the effective action for the slow modes,

$$S_{\rm eff}[s] = S_0[s] + S_{\rm int}[s] + \delta S[s], \tag{1.45}$$

which includes a new contribution that comes from eliminating the high-energy degrees of freedom from the theory.

1.4.2 Derivation of the flow equations for the bosonic theory

The RG results derived above can now be used to determine the way in which the coupling constants are modified upon running the RG. As in the previous section, we continue focus exclusively on the the bosonic theory defined by the action (1.32), which will serve as a warm-up for the fermionic RG in Chapter 4.

In the previous section we derived the effective action (1.45) describing the low-energy behavior of the theory. However, we cannot directly compare the original action (1.32) with the new effective action (1.45) in a meaningful way due to the fact that the latter describes a theory with a different UV cutoff $\Lambda' = e^{-l}\Lambda$ and is written in terms of fields $\varphi_s(k)$ rather than the original fields $\varphi(k)$. Rescaling the momenta as $k' = e^l k$ and the fields as $\varphi_s(k) = e^{(d+3)l/2}\varphi'(k')$, the action $S_0[s]$ becomes

$$\int^{\Lambda} \frac{d^{d+1}k'}{(2\pi)^{d+1}}(k'^2 + e^{2l}r)|\varphi'(k')|^2. \tag{1.46}$$

From this we see that, after dropping the primes on the momentum and field variables, we recover the original action (1.33), but with the "mass term" r replaced by $r_l = e^{2l}r$. Performing the same rescaling procedure for the interaction term in (1.45) gives

$$\frac{g}{2}e^{(3-d)l}\int^{\Lambda}\prod_{i=1}^{4}\frac{d^{d+1}k'_i}{(s\pi)^{d+1}}\delta(k'_1+k'_2-k'_3-k'_4)\bar{\varphi}'(k'_1)\bar{\varphi}'(k'_2)\varphi'(k'_3)\varphi'(k'_4), \tag{1.47}$$

which, again dropping the primes, assumes the same form as (1.34) provided we replace the coupling g by $g_l = e^{(3-d)l}g$.

Putting these results together, we find that the mass term r and the quartic coupling g satisfy the following "tree level" flow equations:

$$\begin{aligned}\frac{dr_l}{dl} &= 2r_l \\ \frac{dg_l}{dl} &= (3-d)g_l.\end{aligned} \tag{1.48}$$

Thus we see already at this order that eliminating the fast modes with momentum $e^{-l}\Lambda < |k| < \Lambda$ and rescaling lengths has left us with a low-energy effective theory with couplings that flow with the RG parameter l. From the first flow equation in (1.48), we see that r_l always grows under RG transformation, and so is referred to as a *relevant* variable. The

flow equation for g_l, on the other hand, indicates that g is relevant for spatial dimension $d < 3$ and irrelevant for $d > 3$. For the case $d = 3$, the coupling becomes neither larger nor smaller under RG (at least at this order in the perturbative expansion) and is said to be *marginal*.

Additional contributions to the flow equations (1.48) come from the last term in the effective action (1.45), which can be computed perturbatively via the cumulant expansion (1.44). The first term in this expansion gives

$$\begin{aligned}\delta S^{(1)}[s] &= 2g \int_{1234}^{\Lambda} \bar{\varphi}_s(1)\varphi_s(2)\langle\bar{\varphi}_f(3)\varphi_f(4)\rangle_f \\ &= 2g \int_{k_<} |\varphi_s(k)|^2 \int_{q_>} G_0(q) \\ &= 2g \frac{\mathcal{S}_{d+1}}{(2\pi)^{d+1}} \frac{\Lambda^{d+1}}{\Lambda^2 + r} dl \int_{k_<} |\varphi_s(k)|^2,\end{aligned} \tag{1.49}$$

where we have introduced the shorthand $\int_{k_<}$ and $\int_{k_>}$ for integrals over slow and fast modes, respectively, and taken the RG step dl to be infinitesimally small. The noninteracting Green function in (1.49) is given by $G_0(q) = (q^2 + r)^{-1}$, and the factor $\mathcal{S}_{d+1}$ is the surface area of a unit sphere in $d + 1$ dimensions (in particular, $\mathcal{S}_3 = 4\pi$ and $\mathcal{S}_4 = 2\pi^2$). If we are interested in behavior near the critical point, as is often the case in RG calculations, then to the order at which we are working, we can set $r \to 0$ in the denominator of (1.49). Then, upon rescaling the momentum k and field $\varphi(k)$ as before, we see that (1.49) gives the following correction to the mass term in our low-energy effective action:

$$\delta r_l = 2g_l \frac{\mathcal{S}_{d+1}\Lambda^{d-1}}{(2\pi)^{d+1}} dl. \tag{1.50}$$

This contribution to the flow of the mass term is shown diagrammatically in the first part of Figure 1.2.

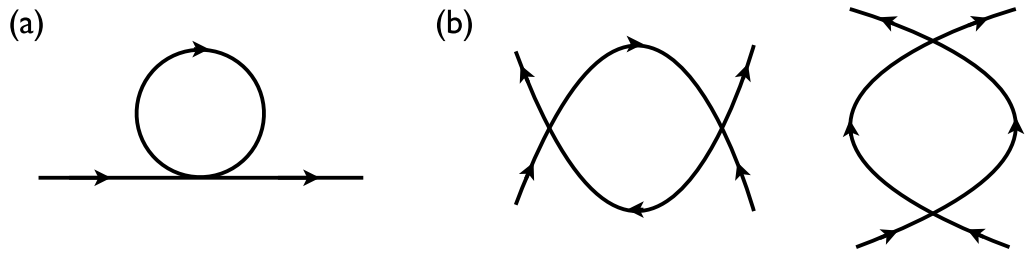

Figure 1.2: Diagrammatic representation of the contributions to the flow equations for (a) the mass term r, and (b) interaction g. In both cases, the internal lines are integrated over fast momenta only, i.e. $e^{-l}\Lambda < |k| < \Lambda$, while the external legs correspond to slow momenta $|k| < e^{-l}\Lambda$.

In order to compute the flow of the interaction g, we need to turn to the second order term in the cumulant expansion (1.44):

$$\delta S^{(2)}[s] = -\frac{1}{2}\left(\langle S_{\rm int}^2[s,f]\rangle_f - \langle S_{\rm int}[s,f]\rangle_f^2\right), \tag{1.51}$$

where $S_{\rm int}$ is given by (1.34). In diagrammatic language, as shown in Figure 1.2, corrections to the interaction term come from one-loop diagrams with four external legs. (Note that the second term in (1.51) cancels the disconnected diagrams.) Mathematically we have

$$\begin{aligned}\delta S^{(2)}[s] = -\frac{1}{2}\left(\frac{g}{2}\right)^2 \int_{1234}\int_{5678}\Big[&16\bar\varphi_s(1)\bar\varphi_s(5)\varphi_s(3)\varphi_s(7)\langle\bar\varphi_f(2)\varphi_f(8)\rangle_f\langle\bar\varphi_f(6)\varphi_f(4)\rangle_f \\ &+ 4\bar\varphi_s(1)\bar\varphi_s(2)\varphi_s(7)\varphi_s(8)\langle\bar\varphi_f(5)\varphi_f(3)\rangle_f\langle\bar\varphi_f(6)\varphi_f(4)\rangle_f\Big],\end{aligned} \tag{1.52}$$

where the prefactors account for the number of possible permutations in taking the contractions. Once the fast momenta of the contracted fields are integrated over, this equation is of the same form as the original interaction term, with the coupling constant replaced by some function $\delta g(k)$, which we can imagine expanding in a Taylor series $\delta g(k) = \delta g(0) + \delta g^{(1)}k^2 + \ldots$. According to our previous tree-level analysis, however, the momentum-dependent terms would all rescale to smaller values under RG for $d \geq 2$, i.e. they would be irrelevant. Thus we are justified in keeping only the k-independent part of

δg, which corresponds to setting the momenta of the external legs to zero in Figure 1.2(b). Thus from (1.52) we have

$$\begin{aligned} \delta g &= -5g^2 \int_{k_>} G_0^2(k) \\ &\approx -5g^2 \frac{\mathcal{S}_{d+1}\Lambda^{d-3}}{(2\pi)^{d+1}} dl. \end{aligned} \tag{1.53}$$

Putting together the results from the tree-level rescaling (1.48) with the one-loop contributions (1.50) and (1.53), the flow equations are

$$\begin{aligned} \frac{dr_l}{dl} &= 2r_l + 2\frac{\mathcal{S}_{d+1}\Lambda^{d-1}}{(2\pi)^{d+1}} g_l \\ \frac{dg_l}{dl} &= (3-d)g_l - 5\frac{\mathcal{S}_{d+1}\Lambda^{d-3}}{(2\pi)^{d+1}} g_l^2. \end{aligned} \tag{1.54}$$

These flow equations contain a great deal of information about the field theory, with the flow of the couplings under the RG procedure indicating the importance of these various couplings at low energies. In particular, noting that the bosonic theory is only stable for $g_l > 0$, one sees from the second equation that interactions are always marginally irrelevant in $d = 3$ dimensions, with $g_l \to 0$ under RG. For $d < 3$, however, the theory has a stable fixed point at

$$\begin{aligned} r^* &= -\frac{3-d}{5}\Lambda^2 \\ g^* &= \frac{(3-d)(2\pi)^{d+1}}{5\mathcal{S}_{d+1}\Lambda^{d-3}}, \end{aligned} \tag{1.55}$$

with this fixed point controlling the low-energy behavior of the theory. In addition, as we have already seen, this approach provides justification for a theory that keeps only some terms while discarding others. The reason why it is not necessary to include terms $\sim k^2|\varphi|^4$ or $\sim |\varphi|^6$ is because these terms are irrelevant, meaning that they matter less and less as one probes the system at lower energies. In this way, Wilsonian RG provides a formal justification for theories such as those studied in Sections 1.2 and 1.3.

In Chapter 4, flow equations analogous to (1.54) for a system of interacting fermions will be derived by following essentially the same procedure as the one shown here for the bosonic theory. The equations in that case will be more complicated due to the fact that there are many allowed couplings g_i. In a fermionic theory it is also possible to have $g_i < 0$, in which case one obtains a runaway flow in which $g_i \to -\infty$. As we saw in Section 1.3, such negative fermionic couplings lead to superconductivity, which is what we shall find in Section 4. While the theory for the bilayer honeycomb lattice will not possess any nontrivial fixed points such as (1.55), in general it will be found that the couplings approach fixed ratios, with $g_i(l)/g_j(l) \to const.$ as $l \to \infty$, and the values of these ratios allow one to determine the nature of the phase transition.

1.5 Thesis outline and relation to published works

In Chapter 2, the Ginzburg-Landau formalism introduced in Section 1.2 is applied to study fluctuation effects near the critical temperature for a system of weakly coupled superconducting layers in a strong magnetic field. We apply a novel expansion in the number of coupled layers, which allows us to recast the problem as an effective theory of a single two-dimensional superconducting layer. In addition to calculating thermodynamic and transport properties from this effective theory, we find a transition to an Abrikosov vortex lattice phase, which is forbidden in a strictly two-dimensional superconductor but arises in our theory due to the interlayer coupling. Most of the work presented in this chapter was first published in Ref. [15]. An extension of this approach, which applies the same type of "large d" expansion to a general class of quantum critical systems, was

published in Ref. [16], and those results are also briefly discussed.

In Chapter 3, we present a study the mixed-valency material KNi_2Se_2, which was first synthesized and studied experimentally in Ref. [17], describing the material theoretically via a microscopic mean-field analysis along the lines of that described in Section 1.3. This material appears to display a host of interesting behaviors, including charge ordering and heavy-fermion-like behavior. Beginning from a microscopic theory that includes Coulomb repulsion between localized d-electrons and hybridization between these localized electrons and conduction electrons, we find a reentrant charge density wave transition in which a charge-ordered phase gives way to a heavy Fermi liquid as temperature is lowered, in agreement with the experimental results. The main results of this chapter were published in Ref. [18].

In Chapter 4, competing ordered phases for interacting fermions on the bilayer honeycomb lattice are studied using a renormalization group scheme analogous to the one presented in Section 1.4. This model also has a physical realization as bilayer graphene, which has been intensely studied both experimentally and theoretically. The presence of Fermi surface nesting allows for the possibility of many types of ordered phases to potentially form, which make it an ideal arena for the application of the RG method. In particular, away from half filling it is found that either particle-hole (e.g. nematic or antiferromagnetic) or particle-particle (e.g. d-wave or f-wave superconductivity) can be realized, with the winning phase depending on the competition between temperature and chemical potential to be the most relevant variable under RG. Thus, in addition to being relevant to experimental studies of bilayer graphene, the approach also allows one to draw some more general conclusions

about the nature of competing particle-hole and particle-particle (superconducting) orders, which are ubiquitous in condensed matter physics. The results of this work can be found in Refs. [19, 20].

For the purpose of keeping the subject matter somewhat unified, some work has been left out of this thesis. As mentioned above, the work on quantum criticality using the "large d" approach of Chapter 2, originally published as Ref. [16], has been substantially compressed, with only the main results being presented in Section 2.4. In addition, a study of vortices in p-wave superconductors using the "holographic" AdS/CFT correspondence, published as Ref. [21], has not been included. In both of these cases, the desire in ommiting the material was to avoid a long, detailed exposition of largely formal theories, preferring instead to focus on theories of competing phases with direct experimental relevance.

Chapter 2

Fluctuation Effects in Layered Superconductors

2.1 Introduction

The discovery of high-temperature superconductivity in iron-pnictides [22, 23] has led to a renewed interest in the physics of layered compounds and the role of superconducting fluctuations. In older high-T_c superconducting cuprates, due in large part to their extreme anisotropy, the fluctuations have taken center stage, particularly in a magnetic field [8, 24]. At present, a rather good understanding of such fluctations is available in two-dimensional (2D) and three-dimensional (3D) systems. However, the intermediate regime, where the interlayer coupling is too weak to be ignored and yet not strong enough to render the system fully 3D, remains an important challenge. Although most theoretical models of pnictides so far have focused on the 2D nature of these materials [25–29], experimental

evidence frequently suggests a pronounced quasi 3D behavior [30,31], especially within the so-called 122 family [32]. Thus, the iron-pnictides apparently belong to this in-between regime.

More generally, it is often a challenge to describe systems that simultaneously feature strong correlations within layers, but weak coupling between layers (or weakly coupled chains in quasi-1D systems). This is especially true in the vicinity of phase transitions, where the dimensionality of the system plays a crucial role. In addressing this problem, some insight can be gleaned from dynamical mean field theory (DMFT), where the hopping between sites is treated in a self-consistent mean-field approximation, while dynamical correlations on a single site are retained [33]. The resulting theory of decoupled sites includes quantum—but not spatial—fluctuations. This approach is known to become exact in the limit of large connectivity, i.e. for each site coupled to a large number of nearest neighbors.

In this chapter, we introduce a theoretical approach that allows for an explicit approximate solution to the problem of superconducting fluctuations in this challenging intermediate situation. First, we show that the Josephson coupling between superconducting layers in a magnetic field can be recast as a contribution to the effective "on-site" Ginzburg-Landau (GL) free energy of a *single* layer, in the limit of a *large* number of neighboring layers. The system is thus described by an *effective* 2D GL theory, which – for practical purposes – can be treated exactly, by solving a set of non-linear, self-consistent equations, in combination with a solution for the purely 2D case [34–37]. Second, we show that this theory – unlike the 2D one – possesses *two* phase transitions, reflecting the *crucial* role of Josephson coupling. Finally, we apply our theory to study fluctuation effects around

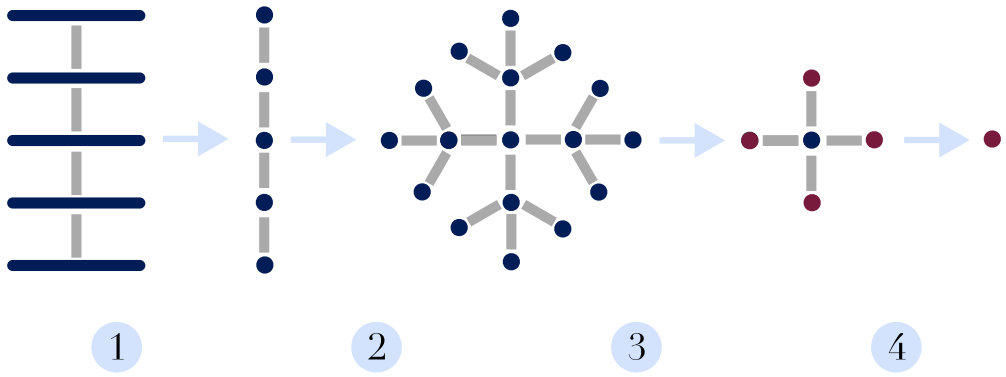

Figure 2.1: Schematic illustration of the self-consistent procedure used to recast the system of coupled superconducting layers as an effective theory of a single layer.

the upper critical field $H_{c2}(T)$ and compare the results to recent experimental data on the iron-pnictide superconductors.

2.2 Derivation of the 2D effective action

The general approach for our "large-d" expansion[1] is shown schematically in Figure 2.1. First, we schematically represent each layer as a single "site," keeping in mind that each such site actually corresponds to a fully interacting 2D superconducting layer. Second, we take the number of nearest-neighbor layers d to be large (where $d = 2$ is the physical case), with the layers occupying an infinite Bethe lattice, as shown in Figure 2.1. Third, we *assume* that it is possible to integrate out further neighbor contributions, leading to an effective 2D action for the layers shown in red. Finally, the nearest neighbors are explicitly integrated out, allowing for the self-consistent determination of the effective action describing a single layer. This procedure will be described in detail as it applies to the specific case of a layered

[1]Note that d refers to the connectivity of the graph shown in Figure 2.1, and is not to be confused with the spatial dimension.

superconductor in the remainder of this section. In Section 2.4, the same procedure will be applied to a general class of quantum critical field theories.

As a model, we consider a general Josephson-coupled layered system, with an individual layer described by the GL model [38]. The partition function is

$$Z = \prod_i \int D(\bar{\psi}_i, \psi_i) e^{-S_0(i) - \sum_{j(i)} S_{\rm int}(i,j)}, \tag{2.1}$$

where $\psi_i \in$ LLL is the fluctuating GL order parameter in the ith layer; LLL denotes the lowest Landau level for charge $2e$; and j is summed over nearest neighbors of layer i. The corresponding action is

$$S_0(i) = \frac{s}{T} \int d^2r \left(\alpha |\psi_i(\mathbf{r})|^2 + \frac{\beta}{2} |\psi_i(\mathbf{r})|^4 \right) , \tag{2.2}$$

where s is the distance between layers, and $\alpha = \alpha_0(t - t_{c2}(h))$, where $t = T/T_c(0)$ and $h = H/H_{c2}(0)$ are the dimensionless temperature and magnetic field, respectively. The interlayer portion of the GL-LLL action (2.1) is

$$S_{\rm int}(i,j) = -\frac{s}{T} \sum_{j=1}^{d} \int d^2r \frac{\eta}{2} \left[\bar{\psi}_i(\mathbf{r}) \psi_j(\mathbf{r}) + \bar{\psi}_j(\mathbf{r}) \psi_i(\mathbf{r}) \right] . \tag{2.3}$$

The goal now is to integrate out the Josephson-coupled portion and obtain a partition function for the 0th layer that is entirely "local," i.e. defined on a *single* layer. As a first step, we assume that this can be done for the layers (denoted by j) that are adjacent to the 0th layer, i.e. that all couplings $S_{int}(j, j+\sigma)$, where σ denotes all layers neighboring layer j except for the 0th layer, can be integrated over, giving a correction to the "on-site" action, so that $S_0(j) \to S_0'(j)$. (When the number of layers j is very large they decouple from each other, and we are left with a Bethe lattice, where each lattice "site" is actually a 2D superconducting layer and the coordination number of the lattice is d. This is different

from the usual DMFT approach [33, 39], where each site is a 0D quantum cluster.) We obtain

$$\begin{aligned} Z(0) = &\int D(\bar{\psi}_0, \psi_0) e^{-S_0(0)} \\ &\times \prod_{j=1}^{d} \frac{1}{Z_0(j)} \int D(\bar{\psi}_j, \psi_j) e^{-S_0'(j) - S_{\rm int}(0,j)}, \end{aligned} \tag{2.4}$$

where $Z_0(j) = Z(j)|_{S_{int}=0}$. Expanding the interlayer term in (2.4), and noting that only even terms in the expansion will survive the functional integration, yields

$$\sum_n \frac{1}{(2n)!} \left(\frac{\eta s}{T} \sum_{j=1}^{d} \int d^2 r \left[\bar{\psi}_0(\mathbf{r}) \psi_j(\mathbf{r}) + \bar{\psi}_j(\mathbf{r}) \psi_0(\mathbf{r}) \right] \right)^{2n}. \tag{2.5}$$

The terms that survive the functional integral are of the form $(\bar{\psi}_0 \psi_0)^n \bar{\psi}_{j_1} \psi_{j_1} \ldots \bar{\psi}_{j_n} \psi_{j_n}$. In the $d \to \infty$ limit, the large majority of these terms has $j_1 \neq j_2 \neq \cdots \neq j_n$. There are $(2n)!$ of each term of this type. Since each involves n pairs, and since there are d possible pairs to choose from, the total number of all such terms (note that j's are indistinguishable) is $(2n)!\binom{d}{n} \xrightarrow{d\to\infty} (2n)! d^n/n!$.

Thus, in the large-d limit (2.5) turns into

$$\begin{aligned} &\sum_n \frac{1}{(2n)!} \left(\frac{\eta s}{T} \right)^{2n} \frac{d^n (2n)!}{n!} \left(\int D(\bar{\psi}_j, \psi_j) e^{-S_0'(j)} \right)^{d-n} \\ &\times \left(\int D(\bar{\psi}_j, \psi_j) e^{-S_0'(j)} \int d^2 r \int d^2 r' \bar{\psi}_0(\mathbf{r}) \psi_0(\mathbf{r}') \bar{\psi}_j(\mathbf{r}) \psi_j(\mathbf{r}') \right)^n. \end{aligned} \tag{2.6}$$

This expression can now be inserted into Eq. (2.4), where, noting that the factors of $(2n)!$ cancel and that the normalization factor cancels the first product of functional integrals in (2.6), the sum over n can be re-exponentiated, giving

$$\begin{aligned} Z^{(1)}(0) = &\int D(\bar{\psi}, \psi) e^{-S_0} \\ &\times \exp\left[\left(\frac{\tilde{\eta} s}{T} \right)^2 \int d^2 r \int d^2 r' \bar{\psi}(\mathbf{r}) \psi(\mathbf{r}') \left\langle \bar{\psi}(\mathbf{r}) \psi(\mathbf{r}') \right\rangle \right]. \end{aligned} \tag{2.7}$$

The superscript in $Z^{(1)}(0)$ signifies that this is the leading term in a large-d expansion. Here we have defined $\tilde{\eta} \equiv \eta\sqrt{d}$ as the new interlayer coupling, which remains finite as $\eta \to 0$ and $d \to \infty$. The j index has been dropped, since all layers are equivalent and are no longer coupled. The general correlation function is defined as

$$\langle \dots \rangle \equiv \frac{\int D(\bar{\psi},\psi)(\dots)e^{-S_0'}}{\int D(\bar{\psi},\psi)e^{-S_0'}}. \tag{2.8}$$

In the symmetric gauge, the correlation function in (2.7) is

$$\left\langle \bar{\psi}(\mathbf{r})\psi(\mathbf{r}')\right\rangle = \frac{T}{2\pi l^2 s\tilde{\alpha}} e^{-(|z|^2+|z'|^2)/4+\bar{z}z'/2}. \tag{2.9}$$

where $z = (x+iy)/l$ is the complex coordinate within a single layer, $l = \sqrt{\phi_0/2\pi H}$ is the magnetic length, and $\tilde{\alpha}$ is defined later. The integral in Eq. (2.7) is thus

$$\begin{aligned} &\frac{1}{\tilde{\alpha}} \int d^2r \int d^2r' \bar{\psi}(\mathbf{r})\psi(\mathbf{r}') e^{-(|z|^2+|z'|^2)/4+\bar{z}z'/2} \\ &= \frac{2\pi l^2}{\tilde{\alpha}} \int d^2r |\psi(\mathbf{r})|^2. \end{aligned} \tag{2.10}$$

The last equality follows from $\psi \in$ LLL.

Following Ref. [35], we make the change of variables $\psi(\mathbf{r}) = \Phi \prod_i (z - z_i) e^{-|z|^2/4}$, where $\{z_i\}$ are the positions of vortices. The interaction of $\{z_i\}$ is set by $U^{-1} \equiv \sqrt{\langle \beta_A \rangle}$, where $\beta_A(\{z_i\}) \equiv \overline{|\psi|^4}/\overline{|\psi|^2}^2$ is the Abrikosov ratio for *arbitrary* $\{z_i\}$ ($\overline{\cdots}$ denotes a spatial average). The partition function for the zeroth layer becomes

$$\begin{aligned} Z^{(1)}(0) &= \int d\Phi^* d\Phi \int dU e^{Ns(U)} e^{-S_{\text{eff}}} \\ S_{\text{eff}} &= \frac{2\pi l^2 sN}{T}\left(\alpha'|\Phi|^2 + \frac{\beta}{2U^2}|\Phi|^4\right) - N\ln(2\pi l^2 s|\Phi|^2) \end{aligned} \tag{2.11}$$

Here N is the number of vortices $\{z_i\}$ and $\alpha' \equiv \alpha - \tilde{\eta}^2/\tilde{\alpha}$. The entropy function $s(U)$ contains all the effects of lateral correlations among vortices $\{z_i\}$, and knowledge of its exact form is equivalent to the exact solution for the thermodynamics of a single layer [35].

In the thermodynamic limit $N \to \infty$, the saddle point method can be applied to integrals over Φ and U in Eq. (2.11). Minimizing with respect to $|\Phi|^2$ gives

$$|\Phi_0|^2 = \frac{1}{2}\left[-\frac{\alpha' U^2}{\beta} + \sqrt{\left(\frac{\alpha' U^2}{\beta}\right)^2 + \frac{4TU^2}{2\pi l^2 s\beta}}\right]. \tag{2.12}$$

In order for this expression to be useful, we must determine the form of $\tilde{\alpha}$, as well as U.

From Eq. (2.9), we have $\tilde{\alpha}^{-1} = (2\pi l^2 s/T)\left\langle\bar{\psi}(0)\psi(0)\right\rangle$. Using this along with Eqs. (2.8) and (2.12), we obtain the following self-consistent expression for $\tilde{\alpha}$:

$$\tilde{\alpha} = \alpha - \frac{\tilde{\eta}^2}{\tilde{\alpha}} + \frac{\beta T}{2\pi l^2 s\tilde{\alpha}U^2}. \tag{2.13}$$

Solving this for $\tilde{\alpha}$, and substituting the result into our expression for α', we get

$$\alpha' = \alpha\left[1 - \frac{2\left(\frac{\tilde{\eta}}{\alpha}\right)^2}{1 + \mathrm{sgn}(\alpha)\sqrt{1 + \frac{2}{\alpha^2}\left(\frac{\beta T}{\pi l^2 sU^2} - 2\tilde{\eta}^2\right)}}\right]. \tag{2.14}$$

In solving for this expression, we must assume $\beta' \equiv \beta - 2\tilde{\eta}^2(\pi l^2 sU^2/T) > 0$. $\beta' < 0$ leads to $\tilde{\alpha} < 0$, which is clearly unphysical. The implications of $\beta' \to 0^+$ at finite T are important and are discussed shortly. Eq. (2.14) constitutes our main theoretical result, allowing us to describe the system of *coupled* layers with a 2D GL-LLL action, albeit with $\alpha \to \alpha'$. Its innocent appearance notwithstanding, the change $\alpha \to \alpha'$ actually entails an elaborate self-consistent calculation to determine the ultimate dependence on T and H. Note that the next term in the large-d expansion – arising from terms in (2.5) with one index repeated four times – modifies the quartic term β in the 2D GL action. It is important to systematically incorporate such finite-d corrections when addressing the details of interlayer correlations in real materials.

Evaluating Eq. (2.11) at its saddle point and using Eq. (2.12), we obtain for the

free energy density

$$\begin{aligned}\frac{F}{V} =& \frac{HT}{\phi_0 s}\left[\frac{1}{2} - \frac{1}{2}g^2U^2 + \frac{1}{2}gU\sqrt{2+g^2U^2}\right. \\ & \left. - \ln\left(-gU^2 + U\sqrt{2+g^2U^2}\right) - \frac{1}{2}\ln\frac{\pi l^2 sT}{\beta}\right],\end{aligned} \tag{2.15}$$

where $g \equiv \alpha'\sqrt{2\pi l^2 s/(2\beta T)}$ can be expressed using Eq. (2.14) as

$$g = g_0\frac{t - t_{c2}(h)}{\sqrt{ht}}\left[1 - \frac{\frac{2}{(t-t_{c2}(h))^2}\left(\frac{\tilde{\eta}}{\alpha_0}\right)^2}{\mathrm{sgn}(\alpha)\Xi(h,t)+1}\right]. \tag{2.16}$$

In the above equation $g_0 \equiv \sqrt{s\phi_0 H_{c2}(0)/16\pi\kappa^2 T_c(0)}$,

$$\Xi(h,t) \equiv \left[1 + \frac{4}{(t-t_{c2}(h))^2}\left(\frac{ht}{2g_0^2U^2(g)} - \left(\frac{\tilde{\eta}}{\alpha_0}\right)^2\right)\right]^{1/2}, \tag{2.17}$$

and we used the GL result $\alpha_0^2/\beta = H_{c2}^2(0)/8\pi\kappa^2$ [40].

$g(t,h)$ (2.16) is the scaling variable of our theory. Since $\Xi(h,t)$ depends on $U(g)$, Eq. (2.16) has the form $g = g(U(g))$. $U(g)$ is the same as in a purely 2D problem, but there $g(t,h) = g_0(t - t_{c2}(h))/\sqrt{ht}$, so the t and h dependencies in our case are very different. $U(g)$ follows from minimization of (2.11) and relies on knowledge of $s(U)$. Here we can turn the problem around and exploit the fact that $\beta_A(g)$ interpolates between its high- and low-T limits of 2 and $\beta_\Delta \equiv 1.159$, respectively. In particular,

$$U(g) = 0.818 - 0.110\,\tanh\left(\frac{g+c_1}{c_2}\right), \tag{2.18}$$

suggested in Ref. [35], where $c_1 = 1.60$ and $c_2 = 2.66$ from the fit to the Monte Carlo results of Ref. [41], yields a virtually exact solution for fluctuation thermodynamics [2]. This expression for $U(g)$ can then be used to solve self-consistently for g in Eq. (2.16).

[2]The thermodynamics thus obtained is within $1 \sim 2\%$ of that from numerical simulations. Even better accuracy may be obtained by using a more elaborate form of $U(g)$, including one that allows for a 2D vortex liquid-to-solid transition at $g = g_M \sim -7$. See Refs. [41–43].

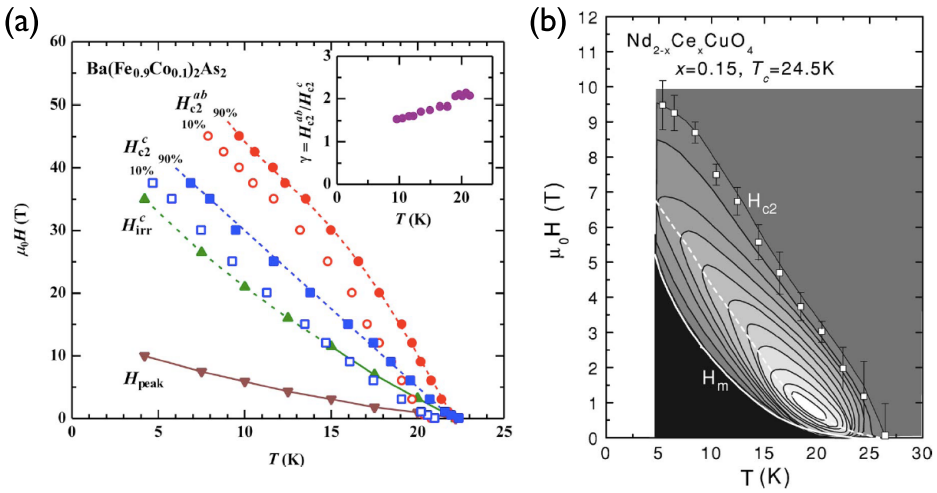

Figure 2.2: Experimental phase diagrams showing magnetic field versus temperature for different types of layered superconductor. The iron-based superconductor $Ba(Fe_{0.9}Co_{0.1})_2As_2$ shown in (a) shows the upper critical field H_{c2} and irreversibility field $H_{\rm irr}$, the latter of which is expected to closely follow the vortex melting transition discussed in the text (data from Ref. [44]). The cuprate superconductor $Nd_{1.85}Ce_{0.15}CuO_4$ shown in (b) has a wider vortex liquid region between the upper critical field and the vortex melting transition at H_m due to the larger anisotropy of this material (data from Ref. [45]).

It is now clear that the divergence in Eq. (2.14), associated with $\beta' \to 0^+$, which occurs for $T \to T_\Delta = 2\pi l^2 \tilde{\eta}^2 s/(\beta\beta_\Delta)$, is endowed with special significance. As T is lowered toward T_Δ, $g \to -\infty$ (since $g \propto \alpha'$), and thus $U(g) \to 1/\sqrt{\beta_\Delta}$. Therefore, at *finite* temperature T_Δ the system undergoes a Bose-Einstein condensation transition into the Abrikosov lattice state. In a purely 2D ($\tilde{\eta} = 0$) theory, such a transition could occur only at $T = 0$. Once $\tilde{\eta} \neq 0$, this transition moves to finite T_Δ, which, over a large portion of an $H - T$ phase diagram, is far below the vortex liquid-solid transition taking place at T_M, defined by $g = g_M \sim -7$. As $H \to 0$, both T_Δ and T_M tend into $T_{c2}(H)$. This echoes the phase diagram of layered superconductors proposed in Ref. [46]. The theoretical phase diagram in Figure 2.3 shows the transition to the Abrikosov vortex lattice. Comparing with the experimental phase diagrams shown in Figure 2.2 shows that, while the theory does

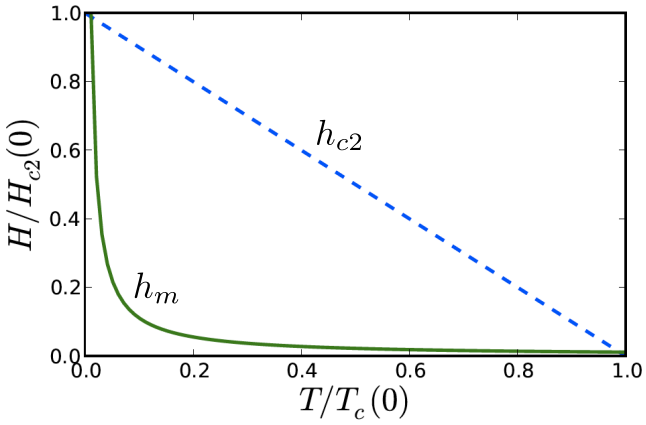

Figure 2.3: Theoretical phase diagram, with the dashed line showing the "mean field" transition line given by $t + h = 1$, which, due to the quasi-2D nature of the superconductor, corresponds not to a mean-field transition but to a crossover, where superconducting fluctuations become important. The lower line gives the melting transition, below which the vortex lattice undergoes Bose-Einstein condensation to form a rigid Abrikosov lattice, using experimental parameters as given in the text for the material $BaFe_{1.8}Co_{0.2}As_2$. Due to the LLL approximation, the lower curve should not be trusted at very low fields.

capture the characteristic upward curvature in both cases, the theoretical phase diagram much more closely resembles the data for the cuprate superconductor than the pnictide superconductor. (A similar phase diagram for the pnictide superconductor $Ba_{0.5}K_{0.5}Fe_2As_2$ has been recently obtained in Ref. [47].) This may be a consequence of the stronger vortex pinning due to impurities in pnictides [44], which tends to raise the lower transition line to higher temperatures and fields.

2.3 Calculation of thermodynamic and transport properties

We now turn our attention to fluctuation thermodynamics [35, 48, 49]. The magnetization follows from $4\pi M = -(1/V)\partial F/\partial H$, with $|\Phi_0|^2$ given in (2.12):

$$\frac{4\pi\phi_0 sM}{T_c(0)} = g_0\sqrt{ht}\left(gU^2 - U\sqrt{2+g^2U^2}\right). \tag{2.19}$$

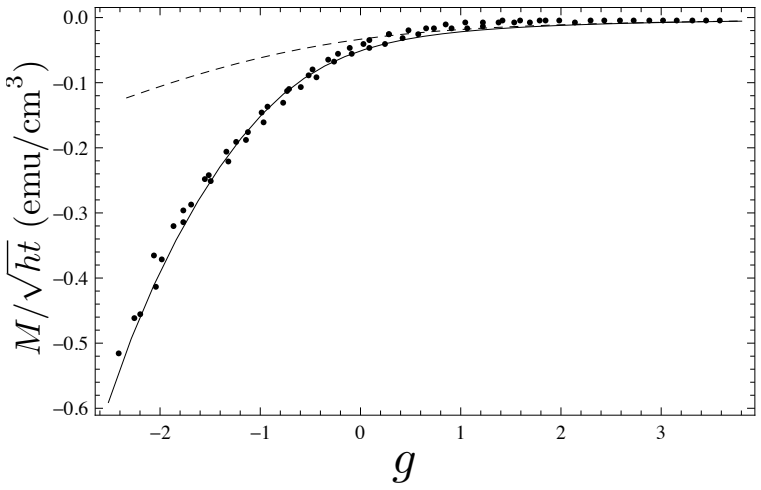

Figure 2.4: Scaled magnetization data from Ref. [31], at fields 3, 5, and 7 T, along with a theoretical fit from Eq. (2.19). The theoretical scaling function (2.19) uses fitting parameters $D_M = 0.70$ and $\tilde{\eta}/\alpha_0 = 0.034$ (solid line), with other parameters given in the text. The dashed line is the 2D case ($\tilde{\eta} = 0$).

Fig. 2.4 shows fluctuation magnetization data [31] for $BaFe_{1.8}Co_{0.2}As_2$, and a fit of Eq. (2.19) to the data. For this sample $T_c(0) = 23.6$ K; and we obtain $g_0 = 5.8$ using the values $H_{c2}(0) = 72$ T for the upper critical field, $\kappa = 44$ for the GL parameter [50], and $s = 6.65$ Å for the interlayer spacing [32]. The demagnetization factor D_M, which reduces the overall magnetization by a factor of $1 - D_M$, is not known exactly for this sample, but can be estimated as $D_M \approx 1 - \pi d/(2R)$, which is valid for a flat disk of radius R and thickness $d \ll R$ in a perpendicular magnetic field [51]. The sample used in Ref. [31] is rectangular in shape with length and width $L \approx 10d$, so we expect $D_M \approx 1 - \pi/10$. Fitting the data with respect to D_M and $\tilde{\eta}/\alpha_0$, with other parameters fixed, yields the curve in Fig. 2.4 and $D_M = 0.70$, $\tilde{\eta}/\alpha_0 = 0.034$.

We now calculate the heat capacity $C = -T\partial^2 F/\partial T^2$. From Eq. (2.15) we obtain

$$\frac{2g_0^2}{h\beta_\Delta}c = \left(2\frac{\partial g}{\partial t} + t\frac{\partial^2 g}{\partial t^2}\right)\left(2gU^2 - 2U\sqrt{2+g^2U^2}\right) + \frac{1}{2t} + 2t\left(\frac{\partial g}{\partial t}\right)^2\left(U^2 - \frac{gU^3}{\sqrt{2+g^2U^2}}\right) + 4t\left(\frac{\partial g}{\partial t}\right)^2\frac{dU}{dg}\left(gU - \frac{1+g^2U^2}{\sqrt{2+g^2U^2}}\right). \tag{2.20}$$

Here the heat capacity $c \equiv C/\Delta C_{2d}$ has been normalized to its 2D mean-field value, $\Delta C_{2d} = V\alpha_0^2 t/(s\beta\beta_\Delta) = 2VH_{c2}(0)g_0^2 t/(\phi_0 s\beta_\Delta)$, and g is given by (2.16). Fig. 2.5 shows c for three different values of $\tilde{\eta}$. As $T \to 0$, there is a divergence in the specific heat, stemming from the fact that, for $\tilde{\eta} \neq 0$, $g \to -\infty$ at *finite* $T \to T_\Delta$, as discussed before. This is suggestive of a first-order Abrikosov transition at T_Δ; to describe its details our approach needs to be augmented either by the sixth order GL term (since $\beta' \to 0^+$ at T_Δ) or finite d corrections, something left for future study. The specific heat, being a second derivative, is rather sensitive to this divergence at low T, even for small $\tilde{\eta}$, as we illustrate in the figure.

Recent experiments on $SmFeAsO_{1-x}F_x$ [52] suggest that the fluctuation conductivity follows an approximate 2D scaling behavior of the form predicted by Ref. [36] (see also Ref. [37]), where transport coefficients are derived from the time-dependent GL-LLL theory, within the Hartree-Fock approximation ($\beta_A = 2$). We follow Ref. [36] to obtain the fluctuation conductivity as

$$\sqrt{\frac{H}{T}}\Delta\sigma_{yy} = \frac{\hbar}{64\lambda_{ab}(0)\xi_{ab}(0)T_c(0)}\sqrt{\frac{\pi}{s\phi_0}}\mathcal{K}(g), \tag{2.21}$$

where, in their case, the scaling variable g has its 2D form, i.e. $\tilde{\eta} = 0$ in Eq. (2.16). In obtaining Eq. (2.21), we used the relations from the GL theory $\alpha_0 = e^2H_{c2}^2(0)\lambda_{ab}^2(0)/m_{ab}c^2\kappa^2$ and $H_{c2}(0) = \phi_0/2\pi\xi_{ab}^2(0)$, as well as the expression for the coefficient in the time-dependent GL equation $\Gamma_0^{-1} \approx \pi\hbar\alpha_0/8T_c(0)$ [40, 53]. The scaling function in (2.21) has the form

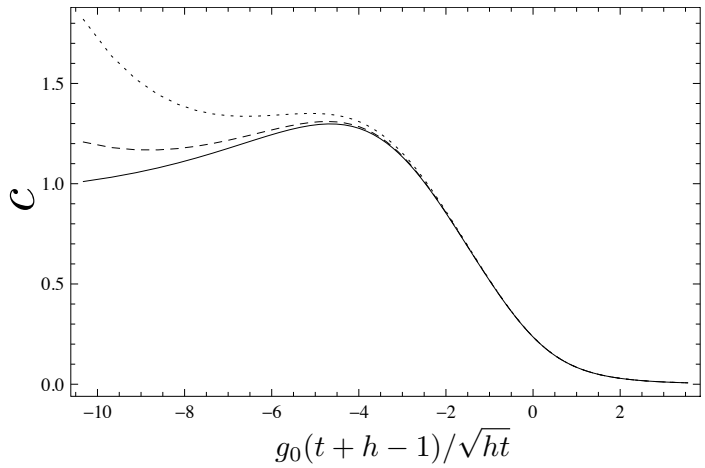

Figure 2.5: Specific heat coefficient from Eq. (2.20), with $g_0 = 3$, $h = 0.3$, and $t_{c2}(h) = 1-h$. The three curves have interlayer coupling values of $\tilde{\eta}/\alpha_0 = 0$ (solid), 0.002 (dashed), and 0.004 (dotted).

$\mathcal{K}(g) = \mathcal{K}_{2D}(g) \equiv -g/2 + \sqrt{1 + g^2/4}$, where now, of course, the scaling variable g must be changed to our Eq. (2.16), with $\tilde{\eta} \neq 0$.

Comparison of the scaling function $\mathcal{K}(g)$ to the experimental data in [52] is not entirely straightforward due to the fact that the sample is a polycrystal. To compensate for this, we replace $\xi_{ab}(0) \to (\xi_{ab}(0)^2\xi_c(0))^{1/3}$ and $\lambda_{ab}(0) \to (\lambda_{ab}(0)^2\lambda_c(0))^{1/3}$ in the prefactor in (2.21). Fig. 2.6 shows $\mathcal{K}(g)$ and the data for the optimally doped ($x = 0.15$, $T_c(0) =$ 51.5 K) sample at $H = 28$ T. The coherence length is $\xi_{ab}(0) = 24$ Å, $\xi_c(0) = 3$ Å [52]; the penetration depth $\lambda_{ab}(0) = 2000$ Å, $\lambda_c(0) = 16000$ Å [54]; the upper critical field[3] $H_{c2}(0)/T_c(0) = 7.8$ T/K, which fits snugly between $|dH_{c2}^{10\%}/dT|$ and $|dH_{c2}^{90\%}/dT|$ reported in Ref. [52]; and the interlayer separation $s = 8.45$Å [55]. One can see that the interlayer coupling leads to a strong enhancement of conductivity over its 2D form, even for modest values of $\tilde{\eta}/\alpha_0$.

In summary, it has been shown that a GL theory of coupled fluctuating super-

[3]The high value of $|dH_{c2}/dT|$ reflects a polycrystalline sample used in Ref. [52] with $\xi_c \ll \xi_{ab}$

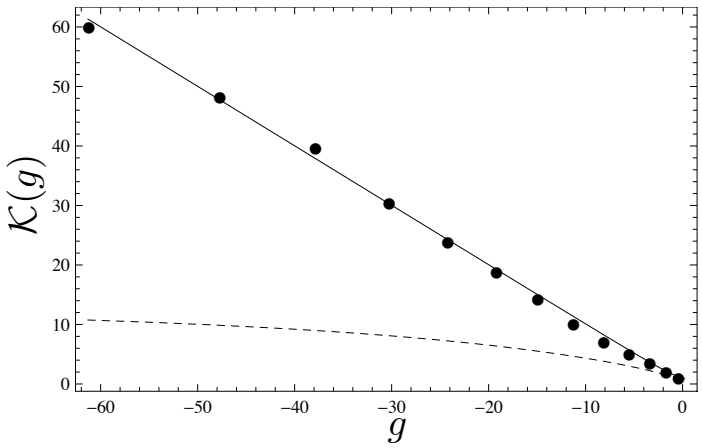

Figure 2.6: Fluctuation conductivity data from Ref. [52], along with a theoretical fit, with scaling variable g from (2.16), $g_0 = 6.37$, and $\tilde{\eta}/\alpha_0 = 0.022$ (solid line). The purely 2D curve ($\tilde{\eta} = 0$) is shown for comparison (dashed line). Other parameters are given in the text.

conducting layers in a magnetic field can be expressed as an *effective, self-consistent single* layer problem, in the limit of a large number of neighboring layers. Comparison of the theory with experimental results in the iron-pnictides is favorable, and provides a means of making the quasi 3D nature of these and similar materials more theoretically tractable. Our approach can be generalized to other 2D, 1+1D or 2+1D problems, as well as to quantum (i.e. zero temperature) phase transitions, which we analyze in the following section.

2.4 Application to quantum critical systems

More recently, the "large $d-2$" approach described in this chapter has also been used to study critical phenomena in quantum critical systems of arbitrary dimension [16]. Such a system exhibits a phase transition at zero temperature as some parameter is varied, for instance pressure or magnetic field. As before, we consider anisotropic systems which feature weak coupling along certain directions, but now with the 2D superconducting layer

replaced by a d-dimensional "extended node." In addition to layered systems, such a model might also describe coupled 1D chains, such as those found in many organic compounds [56]. We then proceed to integrate out the coupling between nodes in the same way as before, leading to an effective d-dimensional theory, whose critical behavior can be studied. Below we recount the main results of this procedure, the details of which can be found in Ref. [16].

2.4.1 Derivation of the effective action

As a model of a quantum critical system, we consider a quantum rotor model, where the action for a single d-dimensional node is given by

$$\begin{aligned} S_i[\phi_i, \lambda_i, \chi] =& \frac{1}{2}\int d^{d+1}x \phi_i^a(x)\hat{G}_0^{-1}\phi_i^a(x) - \frac{i}{2g}\int d^{d+1}x \lambda_i(x) \\ &+ \frac{i}{2}\int d^{d+1}x \lambda_i(x)\phi_i^a(x)\phi_i^a(x) + izt_0 \int d^{d+1}x \chi^a(x)\phi_i^a(x), \end{aligned} \tag{2.22}$$

where i is the node index, $\phi(x)$ is a real, N-component scalar field ($a = 1, 2, \ldots, N$, with summation over these components implicit in (2.22)), and the field $\lambda(x)$ is a Lagrange multiplier that enforces the constraint $|\phi_i(x)|^2 = 1$ at every point in space. The other Lagrange multiplier field $\chi(x)$ in (2.22) enforces the constraint $\sum_i \phi_i^a(x) = 0$, which prevents the system from condensing into the isolated low-energy state that is a special feature of Bethe lattices and leads to trivial critical behavior [16, 57]. The parameter g controls the strength of quantum fluctuations of the field $\phi(x)$, with the system exhibiting a critical point at $g = g_c$ [58, 59]. For $g > g_c$, the system is in a disordered phase with $\langle\phi\rangle = 0$, while for $g < g_c$ the system realizes an ordered phase along some direction. The propagator is given by $G_0^{-1}(p) = p^2 + r$, where $p \equiv (\omega, \mathbf{p})$ is the relativistic momentum. The quantum rotor model arises in multiple physical contexts, emerging as a low-energy effective theory for certain Heisenberg antiferromagnets ($N = 3$), as well as the Bose-Hubbard model ($N = 2$) [59]. It

also shares many universal properties with the well-studied ϕ^4 models of the type studied in Section 1.4 [60].

In addition to the single-node action (2.22), the following term, analogous to the Josephson term in (2.3), couples node i to its z nearest neighbors:

$$S_i^{\rm hop} = -\frac{t_0}{2} \sum_{j(i)=1}^{z} \int d^{d+1}x \phi_i^a(x) \phi_j^a(x), \tag{2.23}$$

where, as for the layered superconductor, we shall take the nodes to lie on a Bethe lattice with $z \to \infty$. (Because we are using d to denote the spatial dimension, in this section we refer to the number of nearest neighbors instead as z.) The total action for the system is then given by

$$S = \sum_i (S_i + S_i^{\rm hop}). \tag{2.24}$$

Again following the procedure illustrated in Figure 2.1, we find that the internode couplings can be integrated out in the limit $z \gg 1$, leading to the following effective action describing a single d-dimensional node:

$$\tilde{S}[\phi, \lambda, \chi] = S[\phi, \lambda, \chi] - \Gamma[\phi, \chi], \tag{2.25}$$

where $S[\phi, \lambda, \chi]$ is given by (2.22), and, dropping the now unnecessary node index i,

$$\exp\left(\Gamma[\phi,\chi]\right) \equiv \frac{z t_0 e^{z t_0 \int_x \langle\phi_x\rangle \phi_x} \int_x \langle\phi_x\rangle \phi_x - z t_0^2 e^{z t_0^2 \int_x \int_{x'} \phi_x \langle \phi_x \phi_{x'}\rangle \phi_{x'}} \int_x \int_{x'} \phi_x \langle \phi_x \phi_{x'}\rangle \phi_{x'}}{z t_0 \int_x \langle\phi_x\rangle \phi_x - z t_0^2 \int_x \int_{x'} \phi_x \langle \phi_x \phi_{x'}\rangle \phi_{x'}}. \tag{2.26}$$

For brevity, we have let $\phi_x \equiv \phi(x)$ and $\int_x \equiv \int d^{d+1}x$. Ideally, one would like to calculate $\langle\phi(x)\rangle$ and $\langle\phi(x)\phi(x')\rangle$ explicitly with respect to (2.25) in order to obtain a fully self-consistent effective action in terms of the fields ϕ and χ. However, the unwieldy form of (2.26) makes this prohibitively difficult in general.

Let us consider the disordered phase, in which $\langle\phi\rangle = 0$, and replace $\chi(x)$ by its mean-field value $\chi_0 = 0$. Then the effective action (2.25) simplifies substantially, becoming

$$S_{\rm eff}[\phi,\lambda] = \frac{1}{2}\int d^{d+1}x \left[\phi^a \mathcal{G}_0^{-1}\phi^a - \frac{iN}{g}\lambda + i\lambda\phi^a\phi^a\right], \tag{2.27}$$

where we have rescaled $g \to g/N$, and also defined $t \equiv \sqrt{z}t_0$, which remains finite as $z \to \infty$ and $t_0 \to 0$. The propagator in (2.27) is related to the original one via the condition

$$\mathcal{G}_0^{-1}(p) \equiv G_0^{-1}(p) - t^2\mathcal{G}(p), \tag{2.28}$$

where $\mathcal{G}(x-x')$, defined via the relation

$$\langle\phi^a(x)\phi^b(x')\rangle = \delta_{ab}\mathcal{G}(x-x') \tag{2.29}$$

is the full propagator, defined with respect to (2.27). Taken together, (2.27)–(2.29) constitute a set of self-consistent equations describing an effective theory for a single node, analogous to (2.11) and (2.13) for the layered superconductor.

2.4.2 Analysis in the large-N limit

Analyzing (2.27) in the large-N limit, we find that there is an excitation gap Δ, and that as one tunes g to approach the quantum critical point, the gap vanishes as $\Delta \sim (g-g_c)^{z\nu}$, where z and ν are critical exponents. Due to the Lorentz invariance of the theory, the dynamical critical exponent is $z = 1$, and from explicit calculation we find that $\nu = 1/2$ for dimensions $d > 2$, which establishes $d = 2$ as the upper critical dimension of the theory. Using similar arguments, the lower critical dimension is found to be $d = 0$. This can be compared with the standard mean-field results of $d = 3$ and $d = 1$ for the upper and lower critical dimension, respectively, in a system with no coupling between nodes. Thus

we see that, for the purposes of critical behavior, the large number of internode couplings have essentially the same effect as adding a single extra spatial dimension to the system.

In order to address fluctuation effects, the self-energy $\Sigma(p)$ can be computed perturbatively in powers of $1/N$. To leading order, the full propagator (2.29) including self-energy corrections is

$$\mathcal{G}(p) = \frac{2}{p^2 + r + \Sigma(p) + \sqrt{[p^2 + r + \Sigma(p)]^2 - 4t^2}}. \tag{2.30}$$

Explicit calculation of the self-energy yields the following results:

$$\Sigma(p) \approx \begin{cases} \frac{2p^2}{N}\left[\ln\left(\ln\frac{\Lambda}{r_c}\right) - \ln\left(\ln\frac{\Lambda}{r_c}\right)\right], & d = 1 \\ \frac{8p^2\ln(\Lambda/p)}{3\pi^2 N}, & d = 2. \end{cases} \tag{2.31}$$

These are in fact identical to the standard results for the theory with no internode coupling, indicating that this coupling has effectively *no influence* on the interaction-induced correlations in the theory, which are encoded in the self-energy. However, as shown above by calculating critical exponents, the internode couplings *do* change the universality class of the transition, effectively shifting the dimension by one. Had we, rather than starting with a theory of coupled nodes, instead started with a theory that was merely anisotropic along different directions, we would have obtained similar results for the critical exponents, but the self-energies would have had the forms corresponding to whatever dimension we chose to work in (including the weakly coupled direction). Thus we see that the method presented here may be useful in general for describing systems with strong correlations along some directions and weak coupling along others, leading to results that are qualitatively different from those obtained via more straightforward anisotropic models.

Chapter 3

Charge Order and Heavy-Electron Formation in KNi_2Se_2

3.1 Introduction

Heavy-fermion materials exhibit a host of fascinating collective quantum behaviors, which have made them a major focus of ongoing research for over three decades [61,62]. The "standard model" of heavy-fermion behavior, as depicted in the famed Doniach diagram [63], features competition between a magnetic phase and the heavy Fermi liquid. In this picture, the local moments, typically at a density of one moment per atomic site, behave at high temperatures as free spins. Upon cooling, these localized moments may either hybridize with the conduction electrons to form heavy quasiparticles with a large effective mass, or else they may remain localized and order magnetically. Which of these options is realized depends on the parameters of the system, which might be tunable experimentally by applied pressure,

doping, or other means. In this way one finds quite generally a competition between the heavy-fermion state and magnetic behavior in these materials.

An intriguing possibility that has received comparatively little attention is the existence of charge order, rather than the usual magnetic order, in proximity to the heavy-fermion state. Mixed-valency systems [64], which contain a variable number of localized electrons per atomic site, are a natural place to look for such competing effects. If the fractional filling takes a commensurate value, then Coulomb repulsion between electrons on nearby sites may induce charge density wave (CDW) ordering. Mixed valency has been studied recently in f-electron materials exhibiting heavy-fermion behavior [65–67], as well as in the context of the related "charge Kondo effect" [68, 69]. However, in both of those cases the emphasis has generally been on the single-site valency as hybridization or interaction between electrons is increased, rather than on the possibility of collective CDW formation and competition of this charge order with the heavy fermion phase.

The material KNi_2Se_2 has recently been shown to exhibit several remarkable physical properties [17], many of which appear to be related to its mixed-valence nature. (see also Refs. [70, 71] for recent work on related materials.) At high temperatures the material has high resistivity; the magnetic susceptibility is constant, indicating Pauli paramagnetic response; and structural analysis reveals that the material has at least three distinct subpopulations of Ni-Ni bond lengths. Upon cooling below $T_{\rm coh} \approx 20$K, the resistivity rapidly decreases, the structural distortions disappear, and the material enters a coherent heavy-fermion state with effective electron mass $m^* \sim 10m_0$, eventually giving way to superconductivity below $T_c \approx 1$ K. This material is also unusual in that an applied magnetic field

induces virtually no response in the measured specific heat and resistivity, indicating that the low-temperature coherent phase does not arise from competition with local magnetic order as in typical heavy-fermion materials. Rather, it was proposed that the coherent state competes with a *charge*-fluctuating state, facilitated by the mixed valency of the Ni ions in KNi_2Se_2 [17].

In this chapter, we present a theory that captures the key ingredients that characterize this system. At high temperatures, the quasi-localized electrons in our model form a CDW and pair with one another into singlet dimers, which explains the observed structural distortion and insensitivity to applied magnetic field. As temperature is lowered, the CDW dissolves in a first-order transition directly into a spatially uniform, correlated heavy-fermion state, without the intermediate single-ion Kondo regime that is usually observed in heavy-fermion materials. The details of this model and the main results of the calculations are presented below.

3.1.1 Review of experimental results

In this section we briefly review the relevant experimental results from Ref. [17]. The presence of charge ordering in this material is inferred from the neutron pair distribution function data shown in Figure 3.1. This data can be viewed as a histogram showing the distances between atomic sites in the crystal lattice. The peaks near 2.7 Å correspond to the distance between neighboring Ni sites. The single peak at temperatures below ~ 20 K indicates that the Ni sites form a uniform square lattice, while the multiple peaks at higher temperatures point to a lattice distortion.

The transport data for KNi_2Se_2 is shown in Figure 3.2. The formation of singlet

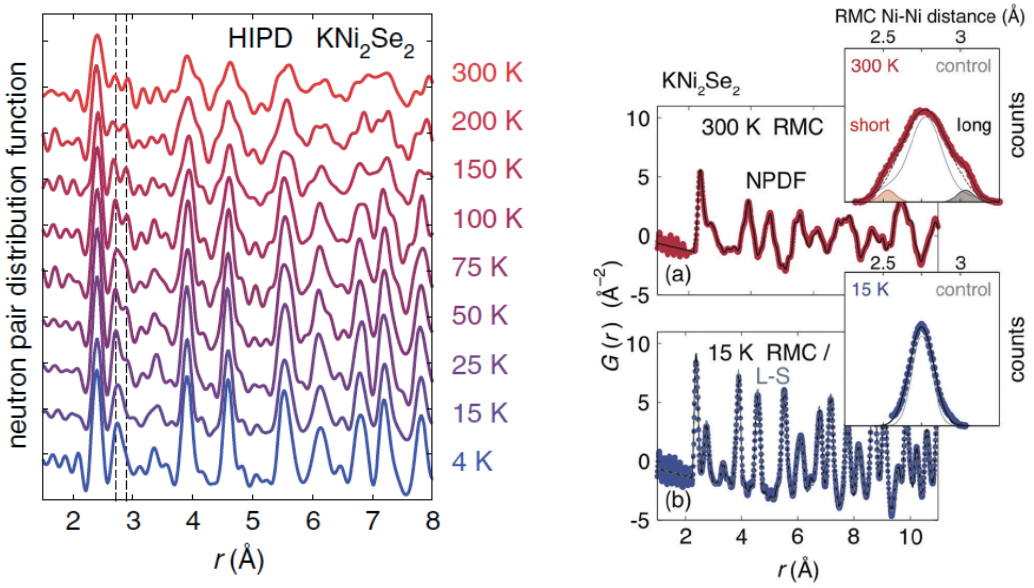

Figure 3.1: Neutron pair distribution function data for KNi_2Se_2, from Ref. [17]. Peaks correspond to interatomic distances. The left panel shows multiple peaks corresponding to nearest-neighbor Ni-Ni distances near 2.7 Å, indicating lattice distortions due to CDW behavior. The coalescence of the peaks at temperatures below $T_{\text{coh}} \sim 20$K indicates that the CDW behavior is absent at low temperatures. The right panel shows fits to the data using reverse Monte Carlo at high (top) and low (bottom) temperatures, along with histograms showing the Ni-Ni bond lengths for each fit.

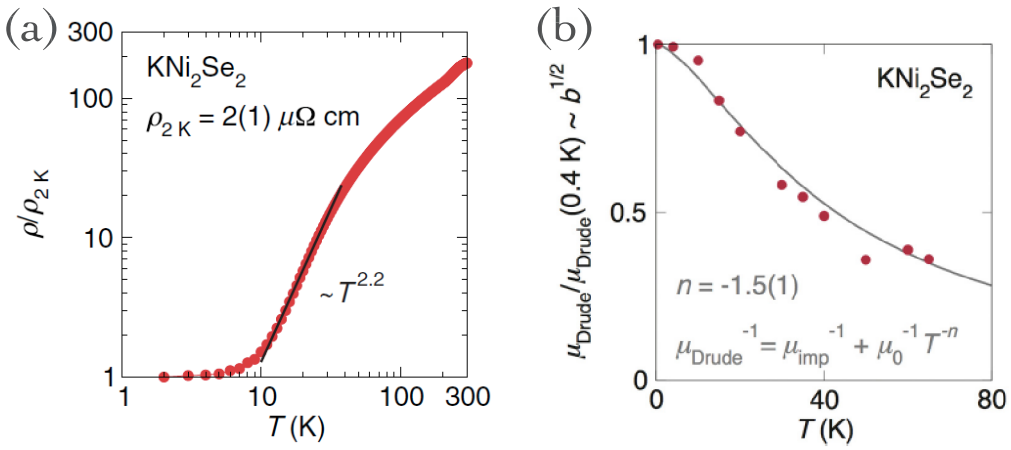

Figure 3.2: Transport for KNi_2Se_2, from Ref. [17]. (a) The resistivity drops rapidly upon cooling below $T_{\rm coh} \sim 20$K, pointing toward the formation of a coherent quantum phase at low temperatures. (b) The electron mobility is enhanced upon cooling.

dimers by the local moments (to be described in greater detail in Section 3.2) may explain the lack of a resistivity peak in measurements on KNi_2Se_2 [17]. Such a peak typically forms in heavy-fermion materials at temperatures just above the coherence temperature, where the Kondo screening clouds are not yet coherent with one another and act as spin-flip scattering centers. A direct transition from a singlet CDW phase to a coherent low-temperature phase (see Figure 3.5 below) precludes this possibility, however, and is consistent with the monotonically decreasing resistivity observed in experiment as T is lowered. In addition, the increase in the carrier mobility at low temperatures is contrary to the usual behavior expected to accompany an effective mass enhancement, and also suggests the formation of a coherent quantum phase with enhanced mobility at low temperatures.

The magnetic susceptibility is shown in Figure 3.3. The absence of a Curie-like tail $\chi \sim 1/T$ indicates that there are no free localized spins in this material at high temperature, which we address below by postulating that the localized spins form singlet pairs with one

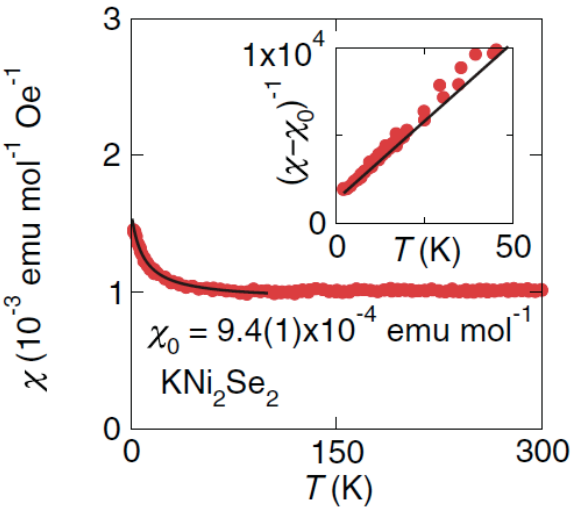

Figure 3.3: Magnetic susceptibility for KNi_2Se_2, from Ref. [17].

another, and thus don't contribute to the magnetic response. The upturn in $\chi(T)$ at low temperatures shown in Figure 3.3 may be due either to the enhanced effective mass or may be a contribution from impurities behaving as free magnetic moments. A theoretical analysis of the susceptibility will be presented below in Section 3.3.

The experimentally determined phase diagram, which summarizes the findings described above, is shown in Figure 3.4. The material shows signatures of CDW formation at temperatures above $T_{\text{coh}} \sim 20$K, and this charge order disappears upon cooling. This is contrary to the naive expectation that the charge-ordered phase ought to have lower entropy than the spatially uniform phase and so would tend to be favored at lower temperatures. The low-temperature phase is characterized by an enhanced effective electron mass, spatial homogeneity, enhanced transport properties, and lattice expansion. Below it is argued that these observations are consistent with this state being a heavy Fermi liquid, with light conduction electrons hybridizing with quasi-localized Ni electrons to form heavy quasiparticles.

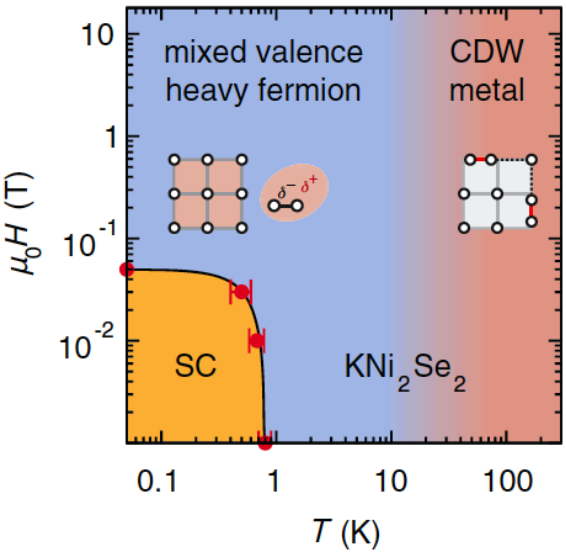

Figure 3.4: Experimental phase diagram for KNi_2Se_2, from Ref. [17]. Upon cooling below temperature $T_{\text{coh}} \sim 20$K for any value of magnetic field, lattice distortions corresponding to CDW behavior disappear. A superconducting phase, which is not included in the model presented here, occurs at at temperatures below $T_c \sim 1$K.

Ordinarily the path to the heavy Fermi liquid features an intermediate regime of single-ion Kondo behavior, in which conduction electrons form screening clouds around the local moments but coherence between these clouds is not yet established [61]. Since these clouds tend to act as scattering centers, this regime tends to feature a pronounced peak in the resistivity. And because they involve localized magnetic moments, heavy-fermion materials are typically sensitive to an applied magnetic field in this intermediate regime. The fact that the CDW transition in Figure 3.4 is independent of magnetic field is thus an unusual feature in such a system, and this will also be addressed in the theory described below.

Figure 3.5 shows a schematic comparison between the usual behavior of heavy-fermion systems as temperature is lowered and the behavior of KNi_2Se_2 described above. This picture provides a qualitative explanation for many of the experimental phenomena

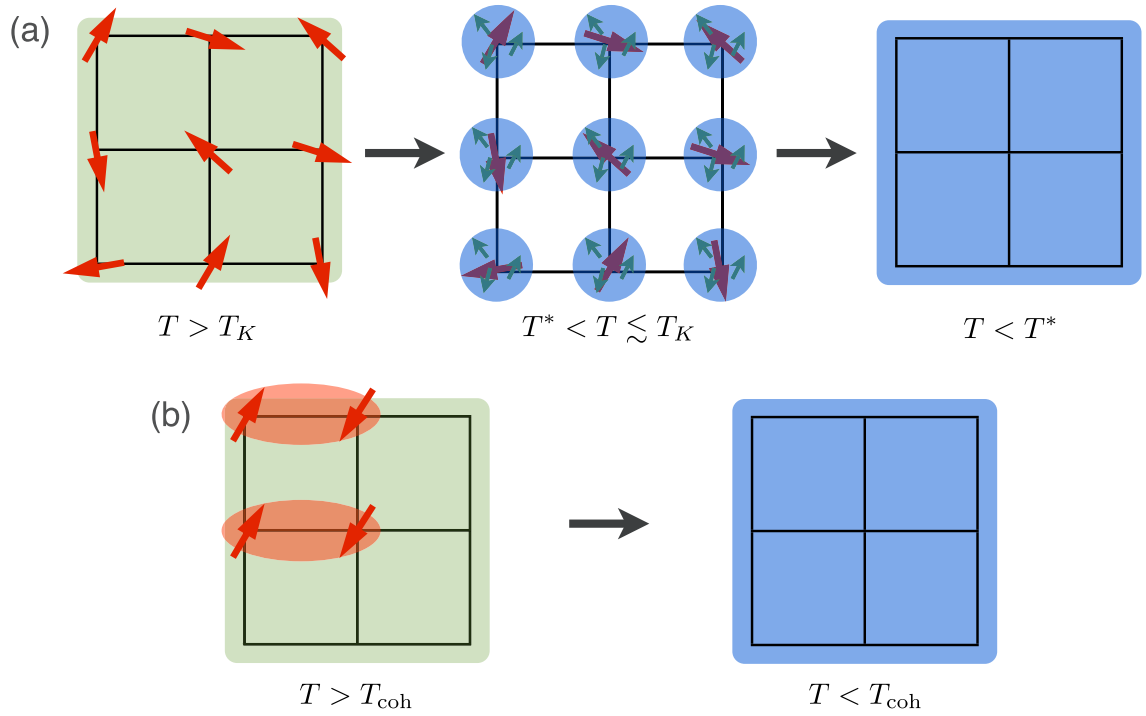

Figure 3.5: (a) In typical heavy-fermion systems, the high-temperature behavior features free localized magnetic moments along with a background of delocalized conduction electrons. Below the Kondo temperature T_K, the conduction electrons form spin singlet screening clouds around the local moments. Below temperature T^*, these screening clouds become coherent, leading to a spatially uniform Fermi liquid with enhanced quasiparticle mass. (b) In the proposed model of KNi_2Se_2, the local moments exhibit CDW behavior and form singlet dimers at high temperatures. Upon cooling below the coherence temperature T_{coh}, this CDW phase directly transitions into a heavy Fermi liquid phase.

described above, including (i) the lack of any significant magnetic response in the high-temperature phase, due to the dimer formation of the local moments; (ii) the absence of a resistivity peak, due to the absence of Kondo screening clouds acting as scattering centers; (iii) the presence of lattice distortions in the high-temperature phase, due to the charge ordering of the local moments; and (iv) the enhanced transport properties and increased quasiparticle effective mass below temperature $T_{\rm coh} \sim 20$K, due to the hybridization between the local moments and conduction electrons, leading to the formation of a heavy Fermi liquid. In the following section it will be shown that this qualitative picture can be realized within a microscopic model solved within the mean-field approximation.

3.2 Mean-field theory of the CDW transition

3.2.1 Model Hamiltonian

KNi_2Se_2 has a quasi-two-dimensional, layered structure, similar to that of heavy fermion materials such as URu_2Si_2 and the "122" family of iron-pnictide superconductors, with the Ni and Se ions alternating in checkerboard fashion on a square lattice within each layer. Consideration of the stoichiometry reveals that the effective valency of Ni in this compound is "1.5+," so that at low energies the effective degree of freedom is one quasi-localized d-electron with spin 1/2 per every two Ni sites, with a small amplitude for these electrons to hop to neighboring Ni sites. These quasi-localized electrons originate primarily from the Ni $d_{x^2-y^2}$ orbitals [17]. Conduction electron bands are formed from the other Ni and Se orbitals and have a significantly greater bandwidth than the quasi-localized d-electrons.

With this picture in mind, the following Hamiltonian describing the "extended periodic Anderson model" provides a useful starting point:

$$\begin{aligned} H_{\mathrm{EA}} = & -t_c \sum_{\langle ij\rangle,\sigma} (c^\dagger_{i\sigma} c_{j\sigma} + H.c.) - t_f \sum_{\langle ij\rangle,\sigma} (d^\dagger_{i\sigma} d_{j\sigma} + H.c.) \\ & - \varepsilon_f \sum_i n_{di} + V \sum_{i,\sigma} (d^\dagger_{i\sigma} c_{i\sigma} + H.c.) \\ & + U \sum_i n_{di\uparrow} n_{di\downarrow} + \sum_{i\neq j} W_{ij} n_{di} n_{dj}, \end{aligned} \tag{3.1}$$

where i, j denote Ni sites on a two-dimensional square lattice. The first term in this equation describes hopping of the conduction electrons. The second and third terms describe the hopping and on-site energy of quasi-localized electrons on neighboring Ni sites. The fourth term describes hybridization between the two types of electrons. Finally, the last two terms describe Coulomb repulsion of d-electrons occupying the same site and nearby sites, where $n_{di\sigma} = d^\dagger_{i\sigma} d_{i\sigma}$. The Hamiltonian is identical to the well-known periodic Anderson model, with the addition of the W term describing intersite Coulomb repulsion. This term is typically neglected in describing heavy fermion materials since such systems usually have exactly one local moment per site, so such a Coulomb term effectively adds an overall constant to the total energy. It is crucial for describing a system near one quarter filling, however, since such systems are susceptible to Coulomb repulsion-driven charge ordering.

In the limit of large on-site repulsion U, it is convenient to enforce the constraint of no double occupancy through the introduction of slave boson operators [72–74]. In this formulation, we substitute $d_{i\sigma} = b^\dagger_i f_{i\sigma}$, where $f_{i\sigma}$ describes a charge-neutral "spinon" that carries the spin of the electron, and the slave boson operator b_i describes a spinless particle with positive charge. Thus the operation of annihilating a d-electron in this language

corresponds to removing a neutral spin from site i and replacing it with a hole having positive charge. In terms of these new operators, the Hamiltonian (3.1) becomes

$$H \quad = H_c + H_{fc} + H_f + H_W + H_\lambda + H_J, \tag{3.2}$$

where

$$\begin{aligned}
H_c &= -t_c \sum_{\langle ij\rangle,\sigma} (c^\dagger_{i\sigma} c_{j\sigma} + H.c.) \\
H_{fc} &= V \sum_{i,\sigma} (b_i f^\dagger_{i\sigma} c_{i\sigma} + H.c.) \\
H_f &= -t_f \sum_{\langle ij\rangle,\sigma} (b_i b^\dagger_j f^\dagger_{i\sigma} f_{j\sigma} + H.c.) - \varepsilon_f \sum_i n_{fi} \\
H_W &= \sum_{i\neq j} W_{ij} n_{fi} n_{fj} \\
H_\lambda &= i \sum_i \lambda_i (n_{fi} + b^\dagger_i b_i - 1) \\
H_J &= J \sum_{\langle ij\rangle} \mathbf{S}_i \cdot \mathbf{S}_j
\end{aligned} \tag{3.3}$$

The first four terms in (3.2) are analogous to terms appearing in (3.1), but rewritten in the slave boson description. H_λ replaces the on-site repulsion term in (3.1) by enforcing the constraint $n_{fi} + b^\dagger_i b_i = 1$ via the Lagrange multiplier field λ_i (within mean-field theory, this constraint is enforced only on average). The last term in (3.2) describes an antiferromagnetic Heisenberg interaction driven by superexchange between spins on neighboring sites, which is present in the limit where U is large but not infinite, as in the usual t-J model [75]. The Hamiltonian (3.2) is identical to the "Anderson–Heisenberg" model that has been studied recently [76–78], with the addition of the Coulomb term H_W. Because the value of J will

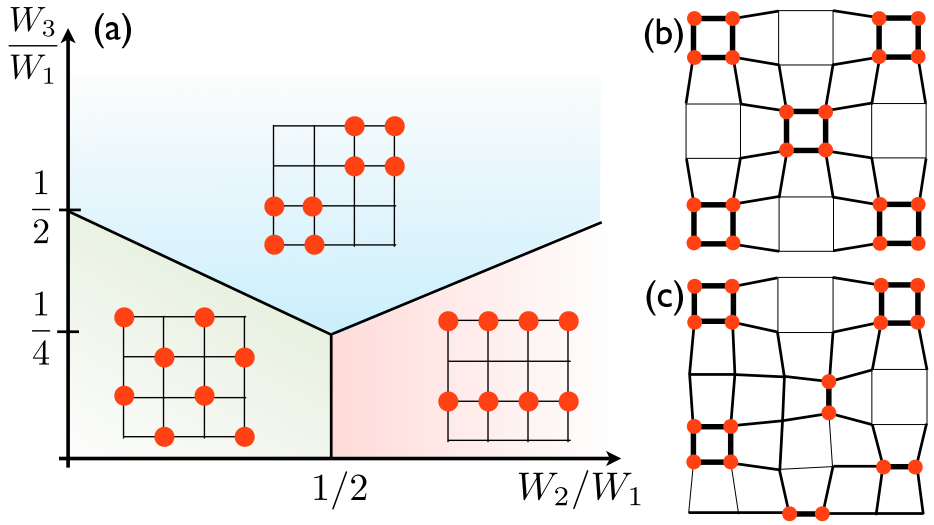

Figure 3.6: (a) $T = 0$ diagram of CDW phases minimizing the term H_W for various values of second- and third-neighbor Coulomb repulsion. (b) Schematic illustration of the "plaquette" phase showing expected lattice distortion once the coupling between electron and lattice degrees of freedom is taken into account. Links connecting sites containing localized electrons are shorter and are represented by thicker lines. (c) Schematic illustration of a possible configuration in the case where long-range CDW order is absent, but the singlet nature of the state and distribution of bond lengths remain similar to those shown in (b).

be sensitive to parameters such as the conduction band filling and other details that we are not particularly concerned with, we shall here include the Heisenberg term as an effective interaction, with the parameter J treated as independent of the other parameters in the model.

Due to the fractional filling of spinons, there is a tendency to develop CDW order when the Coulomb repulsion terms W_{ij} in (3.2) are sufficiently large. Figure 3.6(a) shows a phase diagram with possible CDW phases for various values of first-, second-, and third-nearest neighbor repulsion. We choose parameters such that the "plaquette" CDW phase in the upper part of Figure 3.6(a) is realized, since this phase naturally allows for dimer formation between neighboring spinons. In order to describe the observed absence of high-

termperature Curie magnetic response in KNi_2Se_2, the model should allow for spinons to form singlet pairs with some of their nearest neighbors. Because the spinons in the phase shown in the lower-left part of Figure 3.6 have no nearest neighbors, while the phase in the lower-right would lead to quasi-one-dimensional behavior that has not been observed experimentally, the "plaquette" charge order at large W_3 is chosen as the best candidate. In particular, it is possible for the plaquette phase to be realized for natural choices of couplings where $W_1 > W_2 > W_3$. For example, the plaquette CDW phase is realized in the idealized case of $\sim 1/r$ Coulomb repulsion, for which the ratios of the repulsion terms are $W_2/W_1 = 1/\sqrt{2}$ and $W_3/W_1 = 1/2$. When coupling between electronic and lattice degrees of freedom is taken into account, such a picture can also qualitatively explain the distinct peaks in the distribution of bond lengths observed at $T > T_{\text{coh}}$ via neutron pair distribution function analysis [17], since links containing a dimer can be expected to be shorter than other links. It can be seen from Figure 3.6(b) that each unit cell contains 2 short bonds, 2 long bonds, and 4 bonds of medium length. This is consistent with the three peaks in the distribution of bond lengths observed in experiment, with the central peak larger than the others. While there is no clear experimental evidence of long-range spatial order such as that described here, we expect that the key features of this model—spatially modulated electron density and dimer formation at high temperatures, giving way to a spatially uniform coherent state at low temperatures—will remain valid even in the absence of long-range order, as illustrated schematically in Figure 3.6(c).

3.2.2 Mean-field analysis

We proceed to study the Hamiltonian (3.2) within mean-field theory, assuming that the Coulomb repulsion terms W_i are such that the plaquette order shown in Figure 3.6(a) is favored in the CDW phase. Denoting as sublattice A (B) the sites shown as (un)occupied in the figure, the average occupation number is taken to be $\langle n_{fi} \rangle = n_f + \zeta_i \frac{\Delta}{2}$, where n_f is the average density of spinons per site, Δ is the CDW order parameter, and $\zeta_i = \pm 1$ on sublattice A (B). In the charge-ordered phase, the unit cell contains 8 sites. Letting the operators $f_1, \ldots, f_8$ correspond to the 8 types of spinon within a unit cell, the Coulomb term in (3.2) becomes

$$\begin{aligned} H_W^{\mathrm{MF}} =& W_3 \sum_{i,\delta''} \langle n_{i+\delta''} \rangle \left(n_i - \frac{1}{2} \langle n_i \rangle \right) \\ =& W_3 \sum_K \Bigg[4 \left(n_f - \frac{\Delta}{2} \right) \left(f_{1K}^\dagger f_{1K} + f_{2K}^\dagger f_{2K} + f_{3K}^\dagger f_{3K} + f_{4K}^\dagger f_{4K} \right) \\ & + 4 \left(n_f + \frac{\Delta}{2} \right) \left(f_{5K}^\dagger f_{5K} + f_{6K}^\dagger f_{6K} + f_{7K}^\dagger f_{7K} + f_{8K}^\dagger f_{8K} \right) \Bigg] \\ & + N W_3 (4\Delta^2 - 16 n_f^2), \end{aligned} \tag{3.4}$$

where δ'' denotes third-nearest neighbors, K is the momentum in the reduced Brillouin zone (the reciprocal space corresponding to unit cells rather than sites, lying within the small square around the zone center in Figure 3.7) and N is the total number of unit cells. The indices $1, \ldots, 4$ denote the sites that are occupied in Figure 3.6, while $5, \ldots, 8$ denote those that are unoccupied. At mean-field level, the nearest neighbor and second neighbor Coulomb terms $W_{1,2}$ merely shift the chemical potential for the spinons, so they will not be considered further here. The Lagrange multiplier field λ_i and the slave boson field b_i are also treated as staggered mean fields: $i\lambda_i = \lambda_0 + \zeta_i \lambda_1$ and $b_i = b_0 - \zeta_i b_1$, with $\lambda_{0,1}$ and $b_{0,1}$

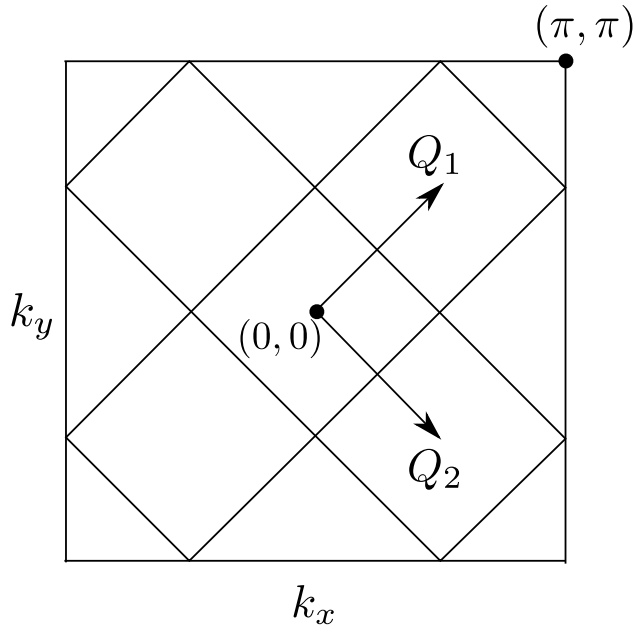

Figure 3.7: Because the unit cell in real space is composed of 8 sites, the Brillouin zone is divided into 8 different regions, which are connected by the wavevectors Q_1 and Q_2. The mean-field Hamiltonian is summed over momenta lying within the small square at the zone center.

real. With this, H_λ in (3.2) becomes

$$\begin{aligned} H_\lambda^{\mathrm{MF}} =& (\lambda_0 + \lambda_1) \sum_K \left(f_{1K}^\dagger f_{1K} + f_{2K}^\dagger f_{2K} + f_{3K}^\dagger f_{3K} + f_{4K}^\dagger f_{4K} \right) \\ &+ (\lambda_0 - \lambda_1) \sum_K \left(f_{5K}^\dagger f_{5K} + f_{6K}^\dagger f_{6K} + f_{7K}^\dagger f_{7K} + f_{8K}^\dagger f_{8K} \right) \\ &- N \left(8\lambda_0 n_f^2 + 16\lambda_1 b_0 b_1 \right). \end{aligned} \tag{3.5}$$

With the above mean-field ansatz for the slave boson field, the mean field hopping Hamil-

tonian from (3.2) is

$$\begin{aligned}
H_t^{\mathrm{MF}} = -t_f \sum_K \Big[& (b_0 - b_1)^2 \Big(e^{i(K_x+K_y)/4} f_{1K}^\dagger f_{2K} + e^{i(K_y-K_x)/4} f_{1K}^\dagger f_{4K} \\
& + e^{i(K_y-K_x)/4} f_{2K}^\dagger f_{3K} + e^{-i(K_x+K_y)/4} f_{3K}^\dagger f_{4K} + H.c. \Big) \\
& + (b_0^2 - b_1^2) \Big(e^{-i(K_x+K_y)/4} f_{1K}^\dagger f_{6K} + e^{i(K_x-K_y)/4} f_{1K}^\dagger f_{8K} + e^{i(K_x-K_y)/4} f_{2K}^\dagger f_{5K} \\
& + e^{i(K_x-K_y)/4} f_{2K}^\dagger f_{7K} + e^{i(K_y-K_x)/4} f_{3K}^\dagger f_{6K} + e^{i(K_x-K_y)/4} f_{3K}^\dagger f_{8K} \\
& + e^{i(K_y-K_x)/4} f_{4K}^\dagger f_{5K} + e^{-i(K_x+K_y)/4} f_{4K}^\dagger f_{7K} + H.c. \Big) \\
& + (b_0 + b_1)^2 \Big(e^{i(K_x-K_y)/4} f_{5K}^\dagger f_{6K} + e^{i(K_y-K_x)/4} f_{5K}^\dagger f_{8K} + e^{i(K_y-K_x)/4} f_{6K}^\dagger f_{7K} \\
& + e^{-i(K_x+K_y)/4} f_{7K}^\dagger f_{8K} + H.c. \Big) \Big]
\end{aligned} \tag{3.6}$$

The Heisenberg spins $\mathbf{S}_i$ are expressed in terms of spinons: $S_i^a = \frac{1}{2} f_{i\alpha}^\dagger \sigma_{\alpha\beta}^a f_{i\beta}$, where σ^a are the Pauli matrices [79]. With this, the Heisenberg term in (3.2) takes the form

$$H_J = -\frac{J}{2} \sum_{\langle ij \rangle} f_{i\sigma}^\dagger f_{j\sigma} f_{j\sigma'}^\dagger f_{i\sigma'} + J \sum_i n_i - \frac{J}{4} \sum_{\langle ij \rangle} n_i n_j. \tag{3.7}$$

Since the second and third terms in this equation merely have the effect of shifting the chemical potential and nearest-neighbor Coulomb repulsion, they shall be neglected here. We introduce the mean fields $\chi_{A,A',B,AB} = \left\langle f_{i\sigma}^\dagger f_{j\sigma} \right\rangle$, with χ_{AB} defined on links between sites on different sublattices, χ_B on links between two sites on sublattice B, and $\chi_{A(A')}$ on links between two sites on sublattice A in the $x(y)$-direction. While these mean fields will all be equal to one another in the uniform phase, in the CDW phase their values will in general be distinct. It is found that the free energy is always lowered in the CDW phase by having only one of $\chi_A, \chi_{A'}$ nonzero, so that the four spins on each plaquette form two

dimers. With the above mean-field ansatz for the spinons, we obtain

$$\begin{aligned}
H_J^{\mathrm{MF}} = -2\sum_K \Big[& \chi_A \Big(e^{i(K_x+K_y)/4} f_{1K}^\dagger f_{2K} + e^{i(K_y-K_x)/4} f_{1K}^\dagger f_{4K} \\
& + e^{i(K_y-K_x)/4} f_{2K}^\dagger f_{3K} + e^{-i(K_x+K_y)/4} f_{3K}^\dagger f_{4K} + H.c. \Big) \\
& + \chi_{AB} \Big(e^{-i(K_x+K_y)/4} f_{1K}^\dagger f_{6K} + e^{i(K_x-K_y)/4} f_{1K}^\dagger f_{8K} + e^{i(K_x-K_y)/4} f_{2K}^\dagger f_{5K} \\
& + e^{i(K_x-K_y)/4} f_{2K}^\dagger f_{7K} + e^{i(K_y-K_x)/4} f_{3K}^\dagger f_{6K} + e^{i(K_x-K_y)/4} f_{3K}^\dagger f_{8K} \\
& + e^{i(K_y-K_x)/4} f_{4K}^\dagger f_{5K} + e^{-i(K_x+K_y)/4} f_{4K}^\dagger f_{7K} + H.c. \Big) \\
& + \chi_B \Big(e^{i(K_x-K_y)/4} f_{5K}^\dagger f_{6K} + e^{i(K_y-K_x)/4} f_{5K}^\dagger f_{8K} + e^{i(K_y-K_x)/4} f_{6K}^\dagger f_{7K} \\
& + e^{-i(K_x+K_y)/4} f_{7K}^\dagger f_{8K} + H.c. \Big) \Big] + \frac{8N}{J} \left(\chi_A^2 + \chi_B^2 + \chi_{AB}^2 \right).
\end{aligned} \tag{3.8}$$

The conduction electrons are also indexed by the 8 sites within a unit cell. The hopping of c-electrons is thus described by

$$\begin{aligned}
H_c = -t_c \sum_K \Big[& e^{i(K_x+K_y)/4} c_{1K}^\dagger c_{2K} + e^{i(K_y-K_x)/4} c_{1K}^\dagger c_{4K} + e^{i(K_y-K_x)/4} c_{2K}^\dagger c_{3K} \\
& + e^{-i(K_x+K_y)/4} c_{3K}^\dagger c_{4K} + e^{-i(K_x+K_y)/4} c_{1K}^\dagger c_{6K} + e^{i(K_x-K_y)/4} c_{1K}^\dagger c_{8K} \\
& + e^{i(K_x-K_y)/4} c_{2K}^\dagger c_{5K} + e^{i(K_x-K_y)/4} c_{2K}^\dagger c_{7K} + e^{i(K_y-K_x)/4} c_{3K}^\dagger c_{6K} \\
& + e^{i(K_x-K_y)/4} c_{3K}^\dagger c_{8K} + e^{i(K_y-K_x)/4} c_{4K}^\dagger c_{5K} + e^{-i(K_x+K_y)/4} c_{4K}^\dagger c_{7K} \\
& + e^{i(K_x-K_y)/4} c_{5K}^\dagger c_{6K} + e^{i(K_y-K_x)/4} c_{5K}^\dagger c_{8K} + e^{i(K_y-K_x)/4} c_{6K}^\dagger c_{7K} \\
& + e^{-i(K_x+K_y)/4} c_{7K}^\dagger c_{8K} + H.c. \Big].
\end{aligned} \tag{3.9}$$

Finally, the hybridization between spinons and conduction electrons is given by

$$\begin{aligned}
H_{fc}^{\mathrm{MF}} = & V \sum_K \Big[(b_0 - b_1) \left(f_{1K}^\dagger c_{1K} + f_{2K}^\dagger c_{2K} + f_{3K}^\dagger c_{3K} + f_{4K}^\dagger c_{4K} \right) \\
& + (b_0 + b_1) \left(f_{5K}^\dagger c_{5K} + f_{6K}^\dagger c_{6K} + f_{7K}^\dagger c_{7K} + f_{8K}^\dagger c_{8K} \right) + H.c. \Big].
\end{aligned} \tag{3.10}$$

3.2.3 Solution of the mean-field equations

With the mean fields defined above, the mean-field equations are obtained by varying the Hamiltonian with respect to $\Delta, \lambda_0, \lambda_1, b_0, b_1, \chi_A, \chi_B$, and χ_{AB}, and then solving the resulting self-consistent equations numerically. In solving the mean-field equations, we require that the average density of spinons is fixed to $n_f = 0.5$ spinons per site in the limit $V = 0$, which is accomplished by appropriately setting the on-site energy of the spinons ε_f. Because we fix the particle number rather than the chemical potential, it is the Helmholtz free energy F rather than the Landau free energy (or "grand potential") Ω that must be minimized, the two quantities being related by $\Omega = F - \mu\mathcal{N}$, where $\mathcal{N}$ is the number of particles. Comparing the free energies for the CDW ($\Delta \neq 0$) and normal ($\Delta = 0$) phases allows one to compute the location of the first-order phase transition between the two phases at a given temperature. Once the hybridization V is nonzero, ε_f remains fixed to this value, and in general $n_f \neq 0.5$ once V is finite. The chemical potential is set to keep the total density of particles in the system fixed at $n_c + n_f = 1.3$ per site, which remains fixed even for $V \neq 0$. The results that follow are not particularly sensitive to the choice of n_c, so long as $n_c > n_f$, so that there are enough conduction electrons to screen all of the local moments in the coherent phase. The ratio of hopping amplitudes for spinons and c-electrons has been set to $t_f/t_c = 0.2$, which is substantially larger than that found in typical heavy-fermion systems. This is a reflection of the fact that the localized moments in KNi_2Se_2 are d-electrons, which are less tightly bound to their atomic cores than the f-electrons that constitute the local moments in most other heavy-fermion systems. This relatively large ratio of bandwidths is also the reason for the rather modest effective mass

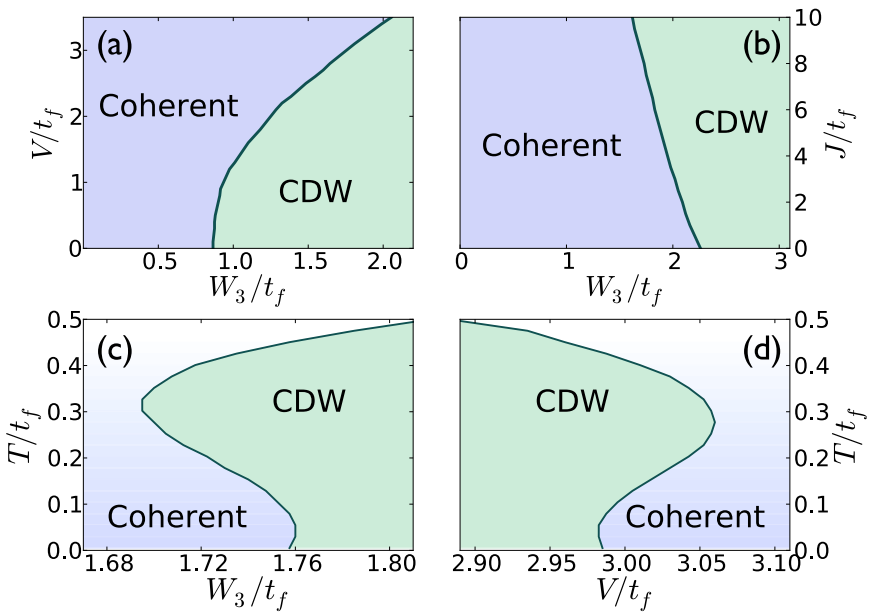

Figure 3.8: Upper plots show the $T = 0$ phase diagrams for V vs. W_3 with $J = 8t_f$ (a), and for J vs. W_3 with $V = 3t_f$ (b). Lower plots show the reentrant transition to the charge-ordered phase as a function of W_3 with $V = 3t_f$ (c), and as a function of V with $W_3 = 1.75t_f$ (d), and with $J = 8t_f$ in both plots. All transitions shown are first order.

enhancement of $m^* \sim 10m_0$ [17], which is $10 \sim 100$ times smaller than that typically found in f-electron heavy fermions.

The phase diagrams shown in Figure 3.8 illustrate the existence of a reentrant, first-order transition from a CDW to a spatially uniform phase upon cooling. The reentrant behavior is rather unusual, as in most systems the phase that breaks translational symmetry is the ground state that is realized as $T \to 0$. While the reentrance occurs along the entire critical line in Figure 3.8(a), it emerges along the critical line in Figure 3.8(b) only for $J \gtrsim 3t_f$, growing in extent as J is increased. These values of J are rather large to be generated by superexchange alone, for which one expects $J \sim t_f^2/U$. It has been suggested that additional contributions might arise in similar contexts from other superexchange processes in the CDW phase [80], or from RKKY interactions at low temperatures [78, 81].

This shows that the heavy quasiparticles are able to reduce their energy by entering a spatially uniform, correlated phase as T is lowered. The temperature at which the reentrance occurs is $T_{\rm coh} \sim 0.1 t_f$. Taking this to be equal to the experimentally observed transition temperature of ~ 20 K, we have $t_f \sim 200$ K ~ 20 meV.

Reentrant behavior reminiscent of that shown here has been seen previously in a theory of simple checkerboard CDW ordering at 1/4 filling in layered molecular crystals [82], although in that case only a second-order transition was found. The model presented here also exhibits a second-order transition, but only at higher temperatures than those shown in Figure 3.8. The mean field χ_A is nonzero throughout the CDW phase shown in Figure 3.8, indicating dimer formation between spinons.

For the parameters given above, there is a jump in the average spinon occupation per site n_f at the first-order transition. At $W_3 = 1.75 t_f$, the occupation jumps from $n_f = 0.45$ for $T < T_{\rm coh} = 0.12 t_f$ to $n_f = 0.53$ for $T > T_{\rm coh}$. The increased valency in the CDW phase is consistent with the lack of long-range CDW order observed in experiment [17], since a long-range ordered state would be impossible at incommensurate filling. It would be interesting to test whether the predicted jump in n_f at $T = T_{\rm coh}$ could be observed experimentally using techniques such as resonant inelastic X-ray scattering [83].

The densities of states in the two phases are shown in Figure 3.9. In the CDW phase, the well-defined peaks above and below the Fermi level clearly show that the spinon excitations are gapped. In contrast, the spinons contribute to the hybridization peak at the Fermi level in the low-temperature phase, as is typical in heavy-fermion materials. The relative magnitude of the peak in this case, however, is substantially smaller than that in f-

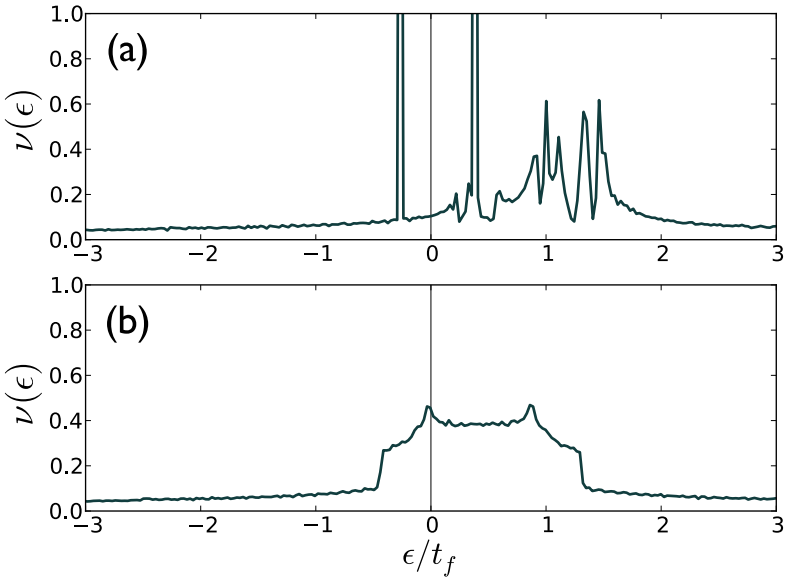

Figure 3.9: Densities of states for the CDW phase at $T = 0.15t_f$ (a) and the coherent phase at $T = 0.01t_f$ (b), with $W_3 = 1.75t_f$, $J = 8t_f$ and $V = 3t_f$. The Fermi level is at $\epsilon = 0$.

electron materials. Comparing the values of the densities of states at the Fermi level in the two different phases, one finds with these particular parameters an enhancement of ≈ 3.0 in the normal phase relative to the CDW phase. This can be compared with measurements on KNi_2Se_2, where an enhancement of ≈ 3.1 was observed in the electronic specific heat coefficient γ for $T < T_{\text{coh}}$ [17].

3.3 Magnetic susceptibility

The uniform magnetic susceptibility can be calculated as the derivative of magnetization with respect to applied magnetic field. Figure 3.10 shows the susceptibility as a function of temperature, assuming that the Lande g-factors for conduction electrons and spinons are equal. The approximately constant susceptibility in the region $T < 0.12t_f = T_{\text{coh}}$ corresponds to the Pauli susceptibility of the heavy Fermi liquid, in which the conduction

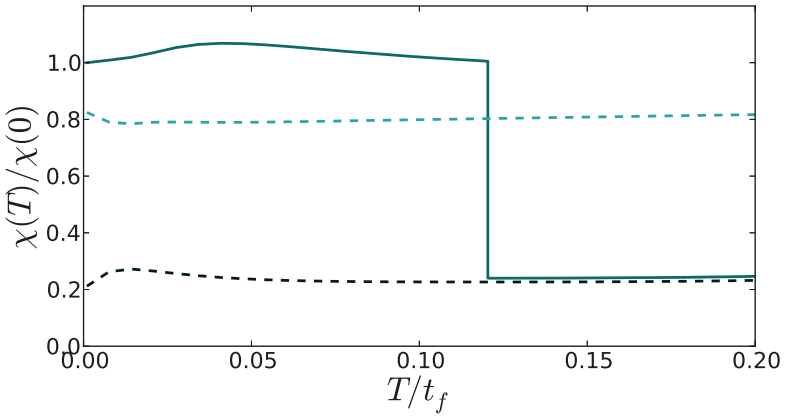

Figure 3.10: Uniform magnetic susceptibility with $W_3 = 1.75t_f$ and $J = 8t_f$. The light and dark dashed lines show $\chi(T)$ in the uniform phase ($V = 4t_f$) and in the CDW phase ($V = 2t_f$), respectively. The solid line shows $\chi(T)$ for $V = 3t_f$, for which the system exhibits a phase transition at $T = T_{\text{coh}} = 0.12t_f$. All plots are normalized to $\chi(0)$ for the solid curve.

electrons are hybridized with the localized spinons, leading to an enhanced density of states near the Fermi level. At T_{coh}, there is a jump in the susceptibility to a much smaller constant value, indicating that only the conduction electrons contribute to the susceptibility at $T > T_{\text{coh}}$, while the spinons form singlet pairs. This is in contrast to the Curie susceptibility $\chi \sim 1/T$ that is typically observed at high temperatures in heavy-fermion materials.

Rather than exhibiting a sharp step at $T \sim T_{\text{coh}}$, however, the experimentally measured $\chi(T)$ remains approximately constant through the CDW transition, as shown in Figure 3.10. One possible explanation for this discrepancy is the Van Vleck contribution to $\chi(T)$, which has not been included in our model. The possibility of a large contribution of this type in heavy-fermion materials has been considered previously [84]. Others have since investigated the Van Vleck contribution to the susceptibility and have found that, when multiple localized bands are approximately degenerate, one generally has $\chi_V \sim \chi_{\text{Pauli}}$ [85–87].

In general, the Van Vleck contribution arises from the Zeeman coupling at second-order in perturbation theory [88]:

$$\chi_V = 2\mu^2 \sum_{\gamma \neq \gamma_0} \left\langle \frac{|\langle \gamma | L^z + 2S^z | \gamma_0 \rangle|^2}{E_{\gamma_0} - E_\gamma} \right\rangle_{\mathrm{FS}}, \tag{3.11}$$

where γ denotes electron orbitals, $\langle \cdots \rangle_{\mathrm{FS}}$ denotes an average over the Fermi surface, and the magnetic field is assumed to be oriented along the z-direction. The inter-orbital energy splitting in the denominator of (3.11) allows for χ_V to become large if this splitting is small. If two or more of the d-electron bands are nearly degenerate, then only one of these bands will hybridize with the conduction electrons. If the splitting is smaller in the CDW phase than in the low-temperature coherent phase (*i.e.* if the unhybridized band has large spectral weight near one of the peaks in Figure 3.9(a)), an increased χ_V could compensate for the decrease in χ_{Pauli} at higher temperatures, with the sum of the two terms remaining roughly constant across the CDW transition. Since the Pauli susceptibility is much larger in typical heavy-fermion systems than in KNi_2Se_2, the Van Vleck term can be expected to provide a greater relative contribution in the latter case. Calculating the precise Van Vleck contribution to the susceptibility would require a more detailed knowledge of the band structure, however, and so we leave this as an open question to be addressed in future work.

In summary, it has been shown that many of the anomalous properties recently measured in the mixed-valency material KNi_2Se_2, in particular the disappearance of CDW behavior upon cooling and the unusual lack of response to applied magnetic field, can be captured within a microscopic mean-field theory describing two species of electrons, with quasi-localized electrons at one-quarter filling hybridizing with a band of light conduction

electrons. A possible direction for future work is to account theoretically for the superconductivity at temperatures $\lesssim 1$ K, which has not been included in the model presented here. A likely scenario is that the superconductivity is unconventional (e.g. *d*-wave), as often observed in heavy-fermion materials and generally in materials in which spin interactions play an important role [61, 89].

Chapter 4

Renormalization Group Study of Doped Bilayer Graphene

4.1 Introduction

Systems of itinerant fermions with repulsive interactions at finite density are often found to form unconventional superconducting states in close proximity to states with particle-hole orders such as nematic order or antiferromagnetism. To date no consensus has emerged regarding the precise mechanism underlying this behavior. In this chapter, we use the weak-coupling renormalization group formalism to shed light on this issue for the particular case of fermions on the bilayer honeycomb lattice away from half-filling, which can be realized experimentally as doped bilayer graphene. We shall find that, as electrons are added to the system, particle-hole order is suppressed, and unconventional superconductivity appears generically in its place.

The competition between different types of ordered phases—and in particular between particle-hole and superconducting phases—is a central issue in our understanding of quantum many-body physics. The idea that superconductivity can arise from repulsive interactions has a long history, dating back to the pioneering work of Kohn and Luttinger showing that the effective interaction between electrons in a metal can be attractive for angular momentum channels with $\ell > 0$, leading to the formation of Cooper pairs, even in cases where the original electron interaction is entirely repulsive [90]. Despite its remarkable success in providing a mechanism for unconventional superconductivity in weakly-coupled systems, the Kohn-Luttinger theory alone is unable to explain the empirically well-established fact that such unconventional superconductivity very often appears in close proximity to a phase with particle-hole order, such as nematic order or antiferromagnetism, and that systems that feature such competing phases tend to exhibit the highest superconducting transition temperatures. Figure 4.1 shows canonical examples of this behavior in two such systems, the cuprate and iron-pnictide superconductors. In both cases, an antiferromagnetic phase (and, in the case of pnictides, a structural transition that is thought to be closely tied to nematic order [91]) is suppressed with chemical doping of either electron or hole charge carriers, giving rise to an unconventional superconducting state. While it is widely believed that this proximity is not merely a coincidence, and that spin fluctuations or other soft modes from the nearby particle-hole phase tend to enhance superconductivity, there is so far no consensus regarding the precise mechanism by which this occurs [89].

The bilayer honeycomb lattice in many ways provides an ideal arena in which to explore these questions. The remarkably rich band structure of this system, which features

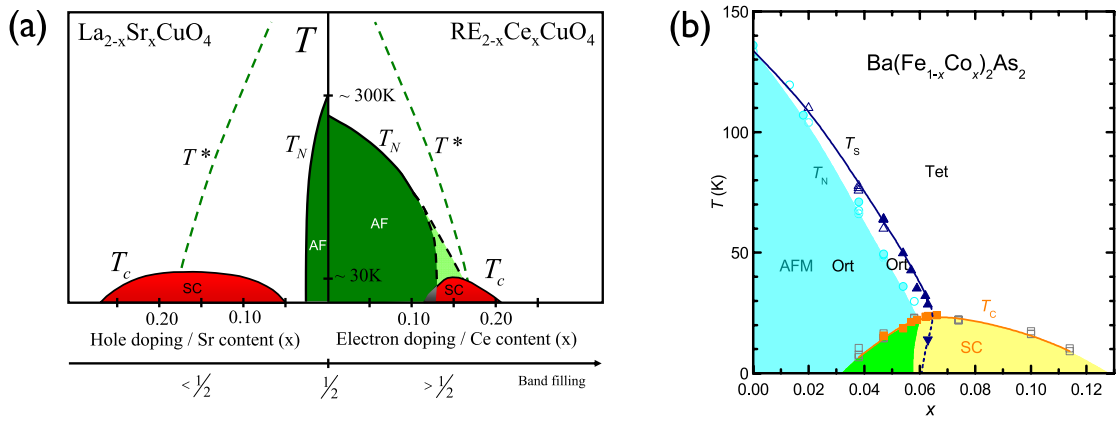

Figure 4.1: Phase diagrams of two well-studied compounds, showing the proximity of superconducting and particle-hole (in this case, antiferromagnetic) orders. (a) In the cuprate superconductors, chemically doping with either electrons or holes destroys the antiferromagnetic insulator and gives rise to a dome of d-wave superconductivity (from Ref. [92]). (b) In the iron-pnictide superconductor $Ba(Fe_{1-x}Co_x)_2As_2$, both the structural and antiferromagnetic transitions (with transition temperatures T_S and T_N, respectively) are suppressed by electron doping, which leads to a superconducting phase that is widely believed to be of the unconventional "$s_\pm$" type, in which the order parameter changes sign between Fermi surface pockets (from Ref. [93]).

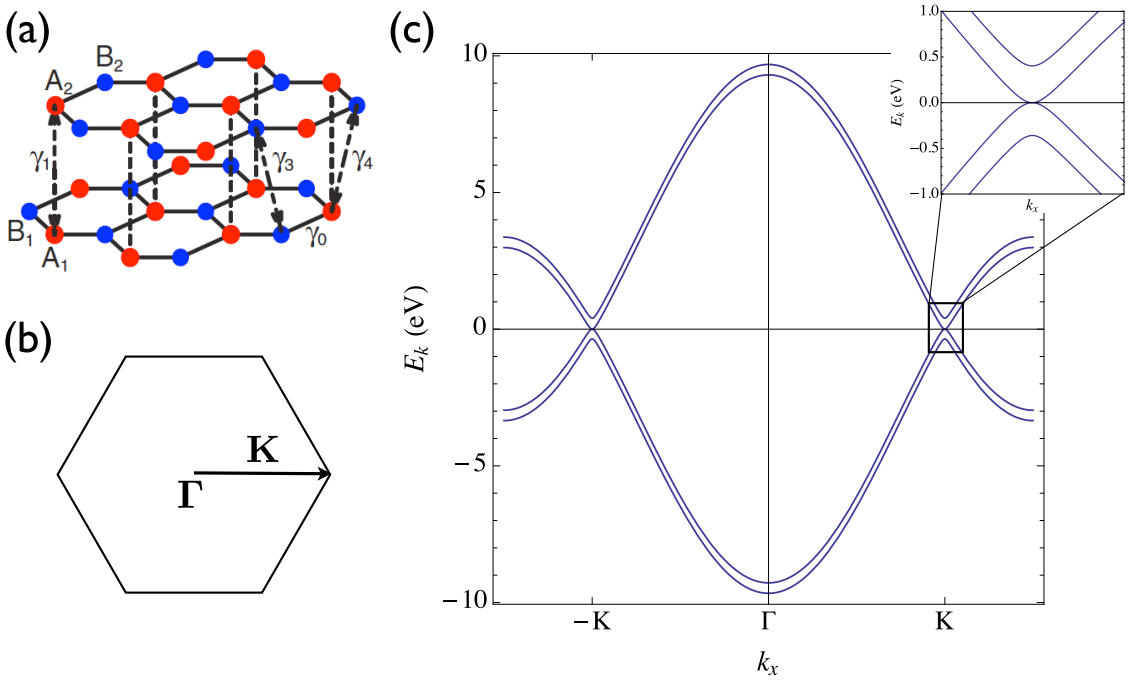

Figure 4.2: (a) The AB stacked bilayer honeycomb lattice, with γ_i corresponding to hopping between various sites. (b) Brillouin zone, showing the location where the bands meet at the zone corner at $\mathbf{K} = (\frac{4\pi}{3\sqrt{3}a}, 0)$. (c) Dispersion of bilayer graphene in the absence of trigonal warping, with parameters from Ref. [94], and $\gamma_{3,4} = 0$. (The effect of trigonal warping on the low-energy band structure is shown in Figure 4.7.)

a high degree of symmetry and nesting, leads to the possibility of instabilities to many types of ordered phases. For the simplest case, in which only nearest-neighbor hopping of electrons is considered, the low-energy spectrum consists of two pairs of upward- and downward-dispersing parabolic bands touching at the charge neutrality point, with one pair each at the $\pm\mathbf{K}$ points of the Brillouin zone, as shown in Figure 4.2.

In addition to being of purely theoretical interest, the bilayer honeycomb lattice has a physical incarnation as bilayer graphene, which can be readily studied experimentally. Experimental studies on suspended samples have shown evidence for the formation of interaction-driven symmetry breaking phases, with evidence emerging for both

gapped [95, 96] and gapless [97] behavior at low energies. The fact that electron interactions in bilayer graphene are strong enough to lead to nontrivial many-body behavior while still being small enough to allow for the use of weakly-coupled theoretical approaches—as evidenced by the small energy scales ($\sim$ meV) at which ordering behavior has been seen experimentally —provides hope that the electronic and thermodynamic properties of this material can be studied and understood both experimentally and theoretically. Theoretical studies of bilayer graphene using a variety of methods have led to many different possibilities for the ground state, with proposals including layer polarized [98, 99], nematic [100, 101], antiferromagnetic [102, 103], and quantum anomalous Hall [104].

The renormalization group (RG) is an attractive option for addressing critical behavior in systems with many competing phases, due in particular to the fact that—unlike standard mean-field theory—it is an unbiased approach that treats all types of order on an equal footing. Due to the fact that electron interactions in this system are marginally relevant, RG can be used to investigate ordering phenomena for arbitrarily weak values of the interaction strength. Recently, the problem of multicriticality was investigated for bilayer graphene at zero doping using a finite-temperature renormalization group approach [105]. In this chapter, we extend the work of Ref. [105] by introducing a finite chemical potential and investigating the types of phases that can form.

4.2 Model of interacting electrons on the honeycomb bilayer

The tight-binding Hamiltonian describing electrons hopping on the bilayer honeycomb lattice shown in Figure 4.2(a) is [102]

$$\begin{aligned} H_{tb} = &- \gamma_0 \sum_{\mathbf{R}\delta\sigma} [a^\dagger_{1\sigma}(\mathbf{R}) b_{1\sigma}(\mathbf{R}+\delta) + a^\dagger_{2\sigma}(\mathbf{R}) b_{2\sigma}(\mathbf{R}-\delta) + H.c.] \\ &- \gamma_1 \sum_{\mathbf{R}\sigma} [a^\dagger_{1\sigma}(\mathbf{R}) a_{2\sigma}(\mathbf{R}) + H.c.] - \gamma_3 \sum_{\mathbf{R}\delta\sigma} [b^\dagger_{1\sigma}(\mathbf{R}-a\hat{\mathbf{y}}) b_{2\sigma}(\mathbf{R}-a\hat{\mathbf{y}}+\delta) + H.c.], \end{aligned} \tag{4.1}$$

where $\delta = -a\hat{\mathbf{y}}, \frac{\sqrt{3}}{2}a\hat{\mathbf{x}} + \frac{1}{2}a\hat{\mathbf{y}}, -\frac{\sqrt{3}}{2}a\hat{\mathbf{x}} + \frac{1}{2}a\hat{\mathbf{y}}$ is a vector connecting nearest neighbor lattice sites, and $a \approx 1.4$Å is the lattice spacing. The hopping parameters connect lattice sites as shown in Figure 4.2(a), with γ_4 and further neighbor hoppings taken to be zero. The experimental values for these parameters are [106] $\gamma_0 \approx 3$eV, $\gamma_1 \approx 0.4$eV, and $\gamma_3 \approx 0.3$eV. The last of these leads to so-called "trigonal warping," which deforms the bands near the $\pm K$ points so that the parabolic low-energy dispersion is replaced by four Dirac cones. The effects of this term will be discussed in detail in Section 4.6.

A low-energy Hamiltonian may be obtained from (4.1) by projecting out [107] (or, equivalently, integrating out [108, 109]) the high-energy modes coming from the dimerized sites, i.e. A_1 and A_2 in Figure 4.2(a). The result of this procedure is

$$H_0 = \sum_{|\mathbf{k}|<\Lambda} \psi^\dagger_{\mathbf{k}} \mathcal{H}_{\mathbf{k}} \psi_{\mathbf{k}}, \tag{4.2}$$

where

$$\mathcal{H}_{\mathbf{k}} = \frac{k_x^2 - k_y^2}{2m^*} 1\sigma_1 1 + \frac{k_x k_y}{m^*} \tau_3 \sigma_2 1 + v_3 k_x \tau_3 \sigma_1 1 - v_3 k_y 1\sigma_2 1. \tag{4.3}$$

The effective mass in this equation is related to the tight-binding parameters as

$$m^* = \frac{2\gamma_1}{9a^2\gamma_0^2}, \tag{4.4}$$

and the velocity leading to the trigonal warping described above is given by $v_3 = 3a\gamma_3$. The experimentally determined values [97] of these parameters are $m^* \approx 0.029m_e$ and $v_3 \approx 1.41$m/s. The Pauli matrices τ_i, σ_i, and s_i operate in the valley, layer, and spin spaces, respectively. We have also introduced the composite spinors

$$\psi_{\mathbf{k}} = \begin{pmatrix} \psi_{\mathbf{K}1}(\mathbf{k}) \\ \psi_{\mathbf{K}2}(\mathbf{k}) \\ \psi_{-\mathbf{K}1}(\mathbf{k}) \\ \psi_{-\mathbf{K}2}(\mathbf{k}) \end{pmatrix}, \tag{4.5}$$

with two-component spinors given by $\psi_{\pm\mathbf{K}a} = (\psi_{\pm\mathbf{K}a\uparrow}, \psi_{\pm\mathbf{K}a\downarrow})^T$, where $\pm\mathbf{K}$ denotes valley, $a = 1, 2$ denotes layer, and $\sigma = \uparrow\downarrow$ denotes spin.

The noninteracting action corresponding to the Hamiltonian (4.2) is given by

$$S_0 = T \sum_{n=-\infty}^{\infty} \sum_{|\mathbf{k}|<\Lambda} \psi^\dagger_{n\mathbf{k}} G_0^{-1}(i\omega_n, \mathbf{k}) \psi_{n\mathbf{k}}, \tag{4.6}$$

where $\omega_n = (2n+1)T$ are fermionic Matsubara frequencies, and the the Green function is

$$\begin{aligned} G_0(i\omega_n, \mathbf{k}) &= \left[(-i\omega_n - \mu) 1_8 + \frac{1}{2m^*}(k_x^2 - k_y^2) 1\sigma_1 1 + \frac{k_x k_y}{m^*} \tau_3\sigma_2 1 + v_3 k_x \tau_3 \sigma_1 1 - v_3 k_y 1\sigma_2 1 \right]^{-1} \\ &= \frac{1}{2} \sum_{s=\pm} (1 + s\tau_3) \frac{(i\omega_n + \mu)1 + (\varepsilon_{\mathbf{k}} \cos 2\theta_{\mathbf{k}} + s v_3 k \cos\theta_{\mathbf{k}})\sigma_1 + (s\varepsilon_{\mathbf{k}} \sin 2\theta_{\mathbf{k}} - v_3 k \sin\theta_{\mathbf{k}})\sigma_2}{-(i\omega_n + \mu)^2 + \varepsilon_{\mathbf{k}}^2 + v_3^2 k^2 + 2s\varepsilon_{\mathbf{k}} v_3 k \cos 3\theta_{\mathbf{k}}} 1. \end{aligned} \tag{4.7}$$

Here we have defined $\varepsilon_{\mathbf{k}} = \mathbf{k}^2/2m^*$. The interacting part of the action, which includes all possible contact interactions, is given by [105]

$$S_{\text{int}} = \sum_{i=1}^{9} \frac{g_i}{2} \sum_{m=1}^{m_i} \int d^2x \int d\tau \left(\psi^\dagger(x,\tau) \Gamma_i^m \psi(x,\tau) \right)^2, \tag{4.8}$$

where i is summed over the nine representations, with a unique coupling g_i corresponding to each representation, and m_i denotes the multiplicity within a representation. The 16 interaction matrices are given in Table 4.1.

Group rep.	Matrix
A_{1g}	$\Gamma_1^{(1)} = 1_8,$
A_{2g}	$\Gamma_2^{(1)} = \tau_3\sigma_3 1$
E_g	$\Gamma_3^{(1,2)} = 1\sigma_1 1, \tau_3\sigma_2 1$
A_{1u}	$\Gamma_4^{(1)} = \tau_3 1_4$
A_{2u}	$\Gamma_5^{(1)} = 1\sigma_3 1$
E_u	$\Gamma_6^{(1,2)} = \tau_3\sigma_1 1, -1\sigma_2 1$
$A_{1\mathbf{K}}$	$\Gamma_7^{(1,2)} = \tau_1\sigma_1 1, \tau_2\sigma_1 1$
$A_{2\mathbf{K}}$	$\Gamma_8^{(1,2)} = \tau_1\sigma_2 1, \tau_2\sigma_2 1$
$E_{\mathbf{K}}$	$\Gamma_9^{(1,2,3,4)} = \tau_1 1_4, -\tau_2\sigma_3 1, -\tau_2 1_4, -\tau_1\sigma_3 1$

Table 4.1: Matices corresponding to the 9 space-group representations of the bilayer honeycomb lattice.

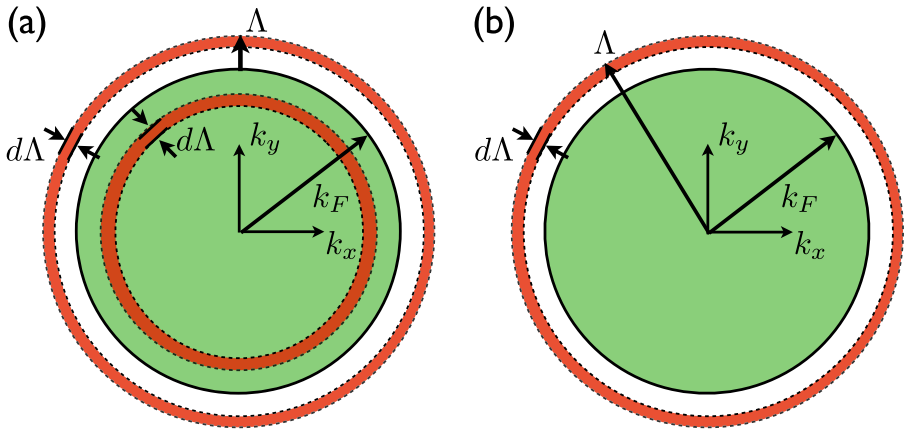

Figure 4.3: (a) In the conventional RG approach for fermions at finite density, modes at both high and low energies (shown in red) are integrated out, yielding an effective theory of fermions near the Fermi surface (occupied states are shown in green). (b) The approach presented here differs in that *all* modes are integrated out, beginning at large momenta, integrating through the Fermi surface, and continuing to $k = 0$.

4.3 Derivation of the flow equations

In the usual approach to performing RG on systems of itinerant fermions at finite density [110, 111], the modes with momenta far away from the Fermi surface are first integrated out, leading to an effective theory describing electrons occupying a thin shell around the Fermi surface, as shown in Figure 4.3(a). This approach of integrating *toward* the Fermi surface has been remarkably successful, providing a firm foundation for Landau's Fermi liquid theory, as well as leading to a deeper understanding of superconductivity and other instabilities of fermionic many-body systems.

The approach employed in this chapter differs in that we begin integrating out modes near the large momentum cutoff Λ and continue integrating *through* the Fermi surface, decreasing the cutoff until all modes have been integrated out, as shown in Figure 4.3(b). The question of which of the two approaches is preferable depends on what sort

of question one is using RG to try to answer. Very often in describing itinerant electron systems one is interested in situations in which the chemical potential is much larger than the energy scales associated with temperature and interaction strength, and in this case the usual approach of integrating toward the Fermi surface is quite reasonable. In situations where these energy scales are comparable, however, as might be the case in bilayer graphene near the neutrality point, keeping the Fermi surface as a rigid kinematic constraint may not be the most useful approach. The first approach is useful if one wishes to end up with a low-energy effective theory similar to the initial one, but with couplings modified by the RG procedure. If one is interested in calculating susceptibilities in order to determine phase diagrams, however, then it makes sense to integrate over *all* momentum values, as we do in the present work. At temperature $T = 0$, of course, one will generally encounter divergences in the couplings and susceptibilities when all modes are integrated out. This can make the RG calculation difficult to control, and in practice one typically cuts off the RG at some finite value of the flow parameter. In contrast, we carry out all calculations at $T > 0$, where the couplings and susceptibilities remain finite above some critical temperature. Exactly at the critical temperature, they diverge only asymptotically as the RG parameter runs to infinity.

In implementing the RG procedure, we begin by integrating out fermionic states within a shell of momenta $e^{-l}\Lambda < k < \Lambda$, where $l > 0$ is the RG flow parameter, while summing over all Matsubara frequencies for those states. We then rescale the frequencies, momenta, fields, and chemical potential in such a way that the noninteracting part of the action (4.6) remains invariant. According to this tree-level rescaling, one obtains for the

temperature $dT/dl = 2T$, which has the solution

$$T_l = T_0 e^{2l}. \tag{4.9}$$

Similarly, for the chemical potential we have $d\mu/dl = 2\mu$, which gives $\mu_l = \mu_0 e^{2l}$. While the RG flow of the temperature given in (4.9) is not affected by corrections arising from interactions, we will see in Section 4.3.2 that the chemical potential flow is modified by such corrections.

4.3.1 Flow of the fermion couplings

In this section the flow equations for the fermion couplings g_i are derived for the special case of vanishing trigonal warping ($v_3 = 0$). In addition to making the calculations significantly simpler, this limit is useful in that it allows us to draw conclusions about the pure Hubbard model (i.e. fermions with on-site interaction and hopping only between nearest neighbors in each direction). The effects of trigonal warping will be addressed in Section 4.6 below. In the limit of no trigonal warping, the noninteracting fermion Green function (4.7) reduces to

$$G_0(i\omega_n, \mathbf{k}) = \frac{1}{\varepsilon_{\mathbf{k}}^2 - (i\omega_n + \mu)^2} \left[(i\omega_n + \mu) 1_8 + \varepsilon_{\mathbf{k}} (\cos 2\theta_{\mathbf{k}} 1\sigma_1 1 + \sin 2\theta_{\mathbf{k}} \tau_3 \sigma_2 1) \right]. \tag{4.10}$$

Working to one loop in perturbative RG, the change to the quartic part of the action due to integrating out a shell of momenta $e^{-l}\Lambda < k < \Lambda$ is given from the cumulant expansion:

$$\begin{aligned} \delta S_{\text{int}} &= -\frac{1}{2} \langle S_{\text{int}}^2 \rangle_{f,1} \\ &= -\frac{1}{2} \left\langle \left(\sum_{i=1}^{9} \frac{g_i}{2} \sum_{m=1}^{m_i} \int_{1234} \psi^\dagger(1) \Gamma_i^m \psi(2) \psi^\dagger(3) \Gamma_i^m \psi(4) \right)^2 \right\rangle_{f,1}, \end{aligned} \tag{4.11}$$

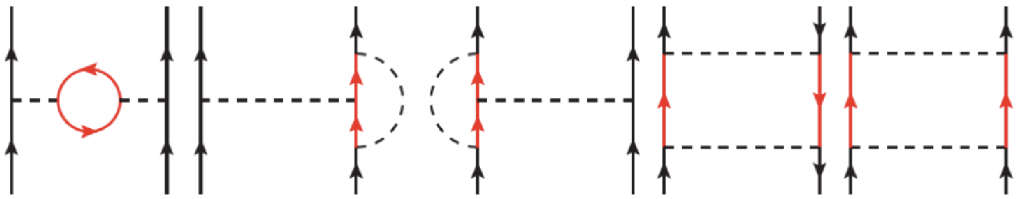

Figure 4.4: Diagrams contributing to the flow equations for the coupling constants. Solid lines correspond to electron propagators, while dashed lines denote interactions. The internal red lines are integrated over "fast" momenta $e^{-l}\Lambda < k < \Lambda$, while the external legs have "slow" momenta $k < e^{-l}\Lambda$.

where $\langle \cdots \rangle_{f,1}$ denotes integration over fast modes for connected diagrams with one loop and four external legs, as shown in Figure 4.4. The integral $\int_{1234}$ denotes integration over momenta and summation over all Matsubara frequencies, along with momentum- and frequency-conserving δ-functions.

The flow equations for the coupling constants can be evaluated as in Ref. [105], with the only major difference being the evaluation of integrals over the fast modes. In evaluating the first four (particle-hole) diagrams shown in Figure 4.4, we need to compute the quantity

$$\begin{aligned} & T\sum_n \int_{\mathbf{k}_>} G_0(i\omega_n,\mathbf{k}) \otimes G_0(i\omega_n,\mathbf{k}) \\ & = T\sum_n \int_{e^{-l}\Lambda}^{\Lambda} \frac{d^2k}{(2\pi)^2} \frac{1}{[\varepsilon_{\mathbf{k}}^2 - (i\omega_n+\mu)^2]^2} \\ & \qquad \times \left[(i\omega_n+\mu)^2 1_8 \otimes 1_8 + \frac{1}{2}\varepsilon_{\mathbf{k}}^2 (1\sigma_1 1 \otimes 1\sigma_1 1 + \tau_3\sigma_2 1 \otimes \tau_3\sigma_2 1) \right]. \end{aligned} \tag{4.12}$$

Starting with the first term, we obtain

$$\begin{aligned}
&T\sum_n \int_{\mathbf{k}_>} \frac{(i\omega_n+\mu)^2}{[\varepsilon_{\mathbf{k}}^2-(i\omega_n+\mu)^2]^2} \\
&= \frac{1}{4}\int_{\mathbf{k}_>}\left[\frac{n_F(\varepsilon_{\mathbf{k}}-\mu)-n_F(-\varepsilon_{\mathbf{k}}-\mu)}{\varepsilon_{\mathbf{k}}} - \frac{1}{4T}\left(\frac{1}{\cosh^2\left(\frac{\varepsilon_{\mathbf{k}}-\mu}{2T}\right)}+\frac{1}{\cosh^2\left(\frac{\varepsilon_{\mathbf{k}}+\mu}{2T}\right)}\right)\right] \\
&= -\frac{m^*}{4\pi}\left[\frac{1}{2}\tanh\left(\frac{1+\tilde{\mu}}{2t}\right)+\frac{1}{2}\tanh\left(\frac{1-\tilde{\mu}}{2t}\right)\right. \\
&\qquad\left. +\frac{1}{4t}\left(\frac{1}{\cosh^2\left(\frac{1-\tilde{\mu}}{2t}\right)}+\frac{1}{\cosh^2\left(\frac{1+\tilde{\mu}}{2t}\right)}\right)\right]dl,
\end{aligned} \tag{4.13}$$

where $n_F(\varepsilon)$ is the Fermi distribution function. In obtaining the last line we used

$$\int_> f(\varepsilon_{\mathbf{k}}) = \frac{m^*}{\pi}\frac{\Lambda^2}{2m^*} f\left(\frac{\Lambda^2}{2m^*}\right)dl, \tag{4.14}$$

and made use of the dimensionless variables

$$\begin{aligned}
\tilde{\mu} &= \frac{\mu}{\Lambda^2/2m^*}, \\
t &= \frac{T}{\Lambda^2/2m^*}.
\end{aligned} \tag{4.15}$$

Similarly, for the second term in (4.12),

$$\begin{aligned}
&T\sum_n \int_{\mathbf{k}_>} \frac{\varepsilon_{\mathbf{k}}^2}{2[\varepsilon_{\mathbf{k}}^2-(i\omega_n+\mu)^2]^2} \\
&= \frac{1}{8}\int_{\mathbf{k}_>}\left[\frac{n_F(-\varepsilon_{\mathbf{k}}-\mu)-n_F(\varepsilon_{\mathbf{k}}-\mu)}{\varepsilon_{\mathbf{k}}} - \frac{1}{4T}\left(\frac{1}{\cosh^2\left(\frac{\varepsilon_{\mathbf{k}}-\mu}{2T}\right)}+\frac{1}{\cosh^2\left(\frac{\varepsilon_{\mathbf{k}}+\mu}{2T}\right)}\right)\right] \\
&= \frac{m^*}{8\pi}\left[\frac{1}{2}\tanh\left(\frac{1+\tilde{\mu}}{2t}\right)+\frac{1}{2}\tanh\left(\frac{1-\tilde{\mu}}{2t}\right)\right. \\
&\qquad\left. -\frac{1}{4t}\left(\frac{1}{\cosh^2\left(\frac{1-\tilde{\mu}}{2t}\right)}+\frac{1}{\cosh^2\left(\frac{1+\tilde{\mu}}{2t}\right)}\right)\right]dl.
\end{aligned} \tag{4.16}$$

For the particle-particle case, corresponding to the fifth diagram in Figure 4.4, we

wish to evaluate the integral

$$
\begin{aligned}
&T\sum_n \int_{\mathbf{k}_>} G_0(i\omega_n,\mathbf{k})\otimes G(-i\omega_n,-\mathbf{k}) \\
&\qquad = T\sum_n \int_{e^{-l}\Lambda}^{\Lambda} \frac{d^2k}{(2\pi)^2}\frac{1}{[\varepsilon_{\mathbf{k}}^2-(i\omega_n+\mu)^2][\varepsilon_{\mathbf{k}}^2-(-i\omega_n+\mu)^2]} \\
&\qquad\quad \times\left[(i\omega_n+\mu)(-i\omega_n+\mu)1_8\otimes 1_8+\frac{1}{2}\varepsilon_{\mathbf{k}}^2(1\sigma_1 1\otimes 1\sigma_1 1+\tau_3\sigma_2 1\otimes\tau_3\sigma_2 1)\right].
\end{aligned}
\tag{4.17}
$$

The first contribution is

$$
\begin{aligned}
&T\sum_n \int_{\mathbf{k}_>} \frac{(i\omega_n+\mu)(-i\omega_n+\mu)}{[\varepsilon_{\mathbf{k}}^2-(i\omega_n+\mu)^2][\varepsilon_{\mathbf{k}}^2-(-i\omega_n+\mu)^2]} \\
&= \frac{1}{8\mu}\int_{\mathbf{k}_>}\left[\frac{\varepsilon_{\mathbf{k}}+2\mu}{\varepsilon_{\mathbf{k}}+\mu}\left(n_F(-\varepsilon_{\mathbf{k}}-\mu)-n_F(\varepsilon_{\mathbf{k}}+\mu)\right)\right. \\
&\qquad\qquad \left. -\frac{\varepsilon_{\mathbf{k}}-2\mu}{\varepsilon_{\mathbf{k}}-\mu}\left(n_F(-\varepsilon_{\mathbf{k}}+\mu)-n_F(\varepsilon_{\mathbf{k}}-\mu)\right)\right] \\
&= \frac{m^*}{8\pi\tilde{\mu}}\left[\frac{1+2\tilde{\mu}}{1+\tilde{\mu}}\tanh\left(\frac{1+\tilde{\mu}}{2t}\right)-\frac{1-2\tilde{\mu}}{1-\tilde{\mu}}\tanh\left(\frac{1-\tilde{\mu}}{2t}\right)\right]dl,
\end{aligned}
\tag{4.18}
$$

while the second gives

$$
\begin{aligned}
&\frac{T}{2}\sum_n \int_{\mathbf{k}_>} \frac{\varepsilon_{\mathbf{k}}^2}{[\varepsilon_{\mathbf{k}}^2-(i\omega_n+\mu)^2][\varepsilon_{\mathbf{k}}^2-(-i\omega_n+\mu)^2]} \\
&= \frac{1}{16\mu}\int_{\mathbf{k}_>}\varepsilon_{\mathbf{k}}\left[\frac{n_F(\varepsilon_{\mathbf{k}}+\mu)-n_F(-\varepsilon_{\mathbf{k}}-\mu)}{\varepsilon_{\mathbf{k}}+\mu}+\frac{n_F(-\varepsilon_{\mathbf{k}}+\mu)-n_F(+\varepsilon_{\mathbf{k}}-\mu)}{\varepsilon_{\mathbf{k}}-\mu}\right] \\
&= \frac{m^*}{16\pi\tilde{\mu}}\left[-\frac{1}{1+\tilde{\mu}}\tanh\left(\frac{1+\tilde{\mu}}{2t}\right)+\frac{1}{1-\tilde{\mu}}\tanh\left(\frac{1-\tilde{\mu}}{2t}\right)\right]dl.
\end{aligned}
\tag{4.19}
$$

Putting these contributions together, one obtains

$$
\begin{aligned}
&T\sum_n \int_{\mathbf{k}_>} G_0(i\omega_n,\mathbf{k})\otimes G(\pm i\omega_n,\pm\mathbf{k}) \\
&\qquad = \frac{m^*}{4\pi}dl\left[\mp f^{(1)}_{ph,pp}(t,\tilde{\mu})1_8\otimes 1_8+\frac{1}{2}f^{(2)}_{ph,pp}(t,\tilde{\mu})(1\sigma_1 1\otimes 1\sigma_1 1+\tau_3\sigma_2 1\otimes\tau_3\sigma_2 1)\right],
\end{aligned}
\tag{4.20}
$$

where

$$
\begin{aligned}
f_{ph}^{(1,2)}(t,\tilde{\mu}) &= \frac{1}{2}\left[\tanh\left(\frac{1+\tilde{\mu}}{2t}\right)+\tanh\left(\frac{1-\tilde{\mu}}{2t}\right)\right] \pm \frac{1}{4t}\left[\frac{1}{\cosh^2\left(\frac{1-\tilde{\mu}}{2t}\right)}+\frac{1}{\cosh^2\left(\frac{1+\tilde{\mu}}{2t}\right)}\right], \\
f_{pp}^{(1)}(t,\tilde{\mu}) &= \frac{1}{2\tilde{\mu}}\left[\frac{1+2\tilde{\mu}}{1+\tilde{\mu}}\tanh\left(\frac{1+\tilde{\mu}}{2t}\right)-\frac{1-2\tilde{\mu}}{1-\tilde{\mu}}\tanh\left(\frac{1-\tilde{\mu}}{2t}\right)\right], \\
f_{pp}^{(2)}(t,\tilde{\mu}) &= -\frac{1}{2\tilde{\mu}}\left[\frac{1}{1+\tilde{\mu}}\tanh\left(\frac{1+\tilde{\mu}}{2t}\right)-\frac{1}{1-\tilde{\mu}}\tanh\left(\frac{1-\tilde{\mu}}{2t}\right)\right].
\end{aligned}
\tag{4.21}
$$

It can be easily verified that for $\tilde{\mu}\to 0$ one recovers the expressions from Ref. [105] (without trigonal warping):

$$
\begin{aligned}
f_{ph,pp}^{(1)}(t,\tilde{\mu}=0) &= \Phi_{1,2}(t) = \tanh\left(\frac{1}{2t}\right)+\frac{1}{2t\cosh^2\left(\frac{1}{2t}\right)}, \\
f_{ph,pp}^{(2)}(t,\tilde{\mu}=0) &= \Phi_{3,4}(t) = \tanh\left(\frac{1}{2t}\right)-\frac{1}{2t\cosh^2\left(\frac{1}{2t}\right)}.
\end{aligned}
\tag{4.22}
$$

With these results in place, we can write the explicit form of the flow equations for the nine coupling constants $g_i(l)$:

$$
\frac{dg_i}{dl} = \sum_{j,k=1}^{9}\sum_{a=1}^{2} g_j g_k\left[\alpha_{ijk}^{(a)} f_{ph}^{(a)}(t,\tilde{\mu}) + \beta_{ijk}^{(a)} f_{pp}^{(a)}(t,\tilde{\mu})\right], \tag{4.23}
$$

where the coefficients are given by

$$
\begin{aligned}
\alpha_{ijk}^{(1)} &= \sum_{m=1}^{4}\left[A_{ijk}^{(1)}(m)+A_{ijk}^{(2)}(m)\right] \\
\alpha_{ijk}^{(2)} &= \sum_{m=1}^{4}\left[A_{ijk}^{(3)}(m)+A_{ijk}^{(4)}(m)\right] \\
\beta_{ijk}^{(1)} &= A_{ijk}^{(1)}(5)+A_{ijk}^{(2)}(5) \\
\beta_{ijk}^{(2)} &= A_{ijk}^{(3)}(5)+A_{ijk}^{(4)}(5).
\end{aligned}
\tag{4.24}
$$

The explicit expressions for the coefficients $A_{ijk}^{(a)}(m)$, which are independent of the RG scale l, are given in Appendix A. (The index m refers to the five diagram contributions in Figure 4.4.)

4.3.2 Flow of the chemical potential

At tree level, as seen in Section 4.3.1, the chemical potential also flows according to its engineering dimension, i.e. $d\mu/dl = 2\mu$. However, the interaction term leads to a one-loop correction to the chemical potential, which modifies the RG flow equation.[1] The one-loop flow equation for $\tilde{\mu}_l$ is

$$\frac{d\tilde{\mu}_l}{dl} = 2\tilde{\mu}_l - 2K(\tilde{\mu}_l, t_l)\sum_i c_i g_i(l), \tag{4.25}$$

where, for the particular case of bilayer graphene with $\nu_3 = 0$, evaluation of the one-loop contribution gives

$$K(\tilde{\mu}_l, t_l) = 1 + \frac{1}{2}\tanh\left(\frac{1+\tilde{\mu}_l}{2t_l}\right) - \frac{1}{2}\tanh\left(\frac{1-\tilde{\mu}_l}{2t_l}\right) \tag{4.26}$$

and

$$\sum_{i=1}^{9} c_i g_i = \frac{m^*}{4\pi}\left(8g_{A_{1g}} - \sum_{j=1}^{9}\sum_{m=1}^{m_j} g_j\right). \tag{4.27}$$

Now let

$$\tilde{\mu}_l = \tilde{\mu}_l^{(0)} + \delta\tilde{\mu}_l, \tag{4.28}$$

where $\delta\tilde{\mu}_l$ is the shift in the chemical potential due to interactions at half filling.[2] At exactly half-filling, we have $\tilde{\mu}_l^{(0)} = 0$, in which case (4.25) becomes

$$\frac{d\delta\tilde{\mu}_l}{dl} \approx 2\delta\tilde{\mu}_l - 2K(0, t_l)\sum_i c_i g_i(l). \tag{4.29}$$

[1] The fact that the chemical potential depends on interactions is intuitively clear from the observation that, assuming the interaction is repulsive, a given particle will have more total energy than in a noninteracting system. Hence the chemical potential must be increased in order to accommodate an equal number of particles as one dials up the interaction.

[2] Forgetting about RG for a moment, the chemical potential in an interacting electron system at fixed particle density generally depends on the interaction g and can be expressed as $\mu(g) = \mu^{(0)} + \delta\mu(g)$, where $\mu^{(0)}$ is g-independent, and $\delta\mu(g)$ can be computed to any desired order in perturbation theory. In the special case of a particle-hole symmetric system at half filling, $\delta\mu(g)$ can also be derived exactly by requiring that the system remain invariant upon performing a particle-hole transformation on the electron operators.

In this equation we have replaced $\delta\tilde{\mu}_l \to 0$ in the argument of $K(\tilde{\mu}_l, t_l)$, since we are only working to leading order in g_i, and $\delta\tilde{\mu}_l \sim g$. Noting from (4.26) that $K(0, t_l) = 1$, the flow equation (4.25) gives (to leading order in g_i)

$$\frac{d\tilde{\mu}_l^{(0)}}{dl} = 2\tilde{\mu}_l^{(0)} - 2[K(\tilde{\mu}_l^{(0)}, t_l) - 1] \sum_i c_i g_i(l). \tag{4.30}$$

From this equation it can be seen that $\tilde{\mu}_l^{(0)}$ does not get generated if it is zero initially, which just means that a system at half-filling must remain at half-filling under RG transformation, as required in this case by particle-hole symmetry [105]. From (4.30) we see that the chemical potential no longer flows according to its engineering dimension in the presence of interactions.[3] Crucially, depending on the sign of the last term in (4.30), the flow of the chemical potential can be either faster or slower than $\sim e^{2l}$. As we shall see in Section 4.4, the phase of the system ultimately depends on which of these two scenarios is realized.

In addition, at the order to which we are working, we can take $\tilde{\mu} \to \tilde{\mu}_l^{(0)}$ in (4.23), so that the flow equation for the coupling constants is

$$\frac{dg_i}{dl} = \sum_{j,k=1}^{9} \sum_{a=1}^{2} g_j g_k \left[\alpha_{ijk}^{(a)} f_{ph}^{(a)}(t_l, \tilde{\mu}_l^{(0)}) + \beta_{ijk}^{(a)} f_{pp}^{(a)}(t_l, \tilde{\mu}_l^{(0)}) \right]. \tag{4.31}$$

Together, the coupled flow equations (4.30) and (4.31) can be solved to determine the properties of the system at low energies. By solving these equations numerically, it is found that, while the chemical potential always grows under RG flow, as one would expect for a relevant perturbation, the behavior of the couplings depends on temperature. At high temperature, the couplings saturate to fixed values as $l \to \infty$. Upon lowering the

[3] It should be noted that in general the chemical potential is also a function of temperature if the particle density is held fixed. This turns out not to be the case for the model considered here, however, due to the fact that the density of states for the noninteracting Hamiltonian is constant at all energies (both positive and negative). In the presence of trigonal warping v_3, however, we indeed find that $\mu = \mu(T)$. This point is discussed in detail in Section 4.6.1.

temperature to just above the critical temperature, the couplings increase exponentially in magnitude over some range of l and saturate at larger and larger values. Precisely at the critical temperature, the couplings continue to diverge exponentially to $\pm\infty$ as $l \to \infty$, while below the critical temperature, the couplings diverge for finite values of l. As we shall see in the following section, the critical properties are determined by the way in which the couplings and chemical potential diverge at $T = T_c$.

4.4 Asymptotic analysis of flow equations

In this section we analyze the $l \to \infty$ behavior of the flow equations for the chemical potential and couplings. As we shall see in Section 4.6, this analysis also applies to the case of nonzero trigonal warping v_3, due to the fact that this quantity is less relevant than either temperature or chemical potential under RG flow.

4.4.1 Couplings and chemical potential

The critical behavior is determined by the asymptotic limit of the flow equations as $l \to \infty$. From (4.30), the flow equation for the chemical potential becomes

$$\frac{d\tilde{\mu}_l^{(0)}}{dl} \overset{(l\to\infty)}{=} 2\tilde{\mu}_l^{(0)} - 2\tanh\left(\frac{e^{-2l}\tilde{\mu}_l^{(0)}}{2t_0}\right)\sum_i c_i g_i(l). \tag{4.32}$$

As $l \to \infty$, the flow equations (4.31) and (4.32) admit solutions of the form

$$\tilde{\mu}_l^{(0)} \sim e^{\alpha l}, \quad \begin{cases} \alpha < 2, & \sum_i c_i g_i(l \to \infty) > 0, \\ \alpha > 2, & \sum_i c_i g_i(l \to \infty) < 0. \end{cases} \tag{4.33}$$

Below we consider the cases $\alpha < 2$ and $\alpha > 2$ separately.

For $\alpha < 2$, assuming $\tilde{\mu}_l^{(0)} \sim e^{\alpha l}$, the flow equation coefficients in (4.21) reduce to

$$\begin{aligned} f_{ph}^{(1)}(l \to \infty) &= f_{pp}^{(1)}(l \to \infty) = \frac{1}{t_l} \sim e^{-2l}, \\ f_{ph}^{(2)}(l \to \infty) &\approx 0 \approx f_{pp}^{(2)}(l \to \infty), \end{aligned} \tag{4.34}$$

where the functions in the second line vanish faster than e^{-2l} and so can be neglected in the limit $l \to \infty$. The flow equation for the coupling constants (4.23) then becomes

$$\begin{aligned} \frac{dg_i}{dl} &\overset{(l\to\infty)}{=} \frac{e^{-2l}}{t_0} \sum_{j,k=1}^{9} \sum_{m=1}^{5} \left[A_{ijk}^{(1)}(m) + A_{ijk}^{(2)}(m) \right] g_j g_k \\ &\equiv e^{-2l} \sum_{j,k=1}^{9} \tilde{A}_{ijk}^{(1)} g_j g_k \end{aligned} \tag{4.35}$$

From this we see that the asymptotic behavior of the runaway couplings is $g_i(l \to \infty) \sim e^{2l}$. In order to be more concrete, we define the "coupling magnitude" as

$$G(l) = \sqrt{\sum_{i=1}^{9} g_i^2(l)}. \tag{4.36}$$

The flow equation for this quantity is then (still for $l \to \infty$)

$$\frac{dG}{dl} = e^{-2l} G^2 \sum_{ijk} \tilde{A}_{ijk}^{(1)} \rho_i \rho_j \rho_k, \tag{4.37}$$

where

$$\rho_i \equiv \lim_{l\to\infty} \frac{g_i(l)}{G(l)} = const. \tag{4.38}$$

We refer to ρ_i as a "fixed ratio," and, as we shall see below when calculating susceptibilities, the relative values of these 9 quantities ultimately determine the nature of the phase instability. The solution to the flow equation for $G(l)$ is

$$G(l) = \frac{2e^{2l}}{\sum_{ijk} \tilde{A}_{ijk}^{(1)} \rho_i \rho_j \rho_k} \tag{4.39}$$

The flow equation (4.32) for $\tilde{\mu}_l^{(0)}$ meanwhile becomes

$$\begin{aligned}\frac{d\tilde{\mu}_l^{(0)}}{dl} &\overset{(l\to\infty)}{=} \left[2 - \frac{1}{t_0}\sum_i c_i g_i(l) e^{-2l}\right]\tilde{\mu}_l^{(0)} \\ &= 2\left[1 - \frac{\sum_i c_i \rho_i}{t_0 \sum_{ijk}\tilde{A}^{(1)}_{ijk}\rho_i\rho_j\rho_k}\right]\tilde{\mu}_l^{(0)}, \qquad (\alpha < 2),\end{aligned} \tag{4.40}$$

where we have utilized (4.39) in the second line. Since the quantity in brackets approaches a constant as $l \to \infty$, this equation indeed has the solution $\tilde{\mu}_l^{(0)} \sim e^{\alpha l}$.

For $\alpha > 2$, assuming from (4.33) that $\tilde{\mu}_l^{(0)} \sim e^{\alpha l}$, the limiting behavior of the functions in (4.21) is

$$\begin{aligned} f_{pp}^{(1)}(l\to\infty) &= \frac{2}{\tilde{\mu}_l^{(0)}} \sim e^{-\alpha l}, \\ f_{ph}^{(1,2)}(l\to\infty) &\approx 0 \approx f_{pp}^{(2)}(l\to\infty). \end{aligned} \tag{4.41}$$

The functions in the second line of (4.41) vanish exponentially faster than $\sim e^{-\alpha l}$ as $l \to \infty$. In this case the asymptotic behavior of the flow equation for the coupling constants is

$$\begin{aligned}\frac{dg_i}{dl} &\overset{(l\to\infty)}{=} \frac{2}{\tilde{\mu}_l^{(0)}}\sum_{j,k=1}^{9}\left[A^{(1)}_{ijk}(5) + A^{(2)}_{ijk}(5)\right] g_j g_k \\ &\equiv e^{-\alpha l}\sum_{j,k=1}^{9}\tilde{A}^{(2)}_{ijk} g_j g_k\end{aligned} \tag{4.42}$$

The flow equation for $G(l)$ then becomes

$$\frac{dG}{dl} = e^{-\alpha l} G^2 \sum_{ijk}\tilde{A}^{(2)}_{ijk}\rho_i\rho_j\rho_k, \tag{4.43}$$

which has the solution

$$G(l) = \frac{\alpha e^{\alpha l}}{\sum_{ijk}\tilde{A}^{(2)}_{ijk}\rho_i\rho_j\rho_k} \tag{4.44}$$

The flow equation (4.32) in this case reduces to

$$\begin{aligned}\frac{d\tilde{\mu}_l^{(0)}}{dl} &\overset{(l\to\infty)}{=} 2\tilde{\mu}_l^{(0)} - 2\sum_i c_i g_i(l) \\ &= 2\tilde{\mu}_l^{(0)} - \frac{2\alpha e^{\alpha l}\sum_i c_i\rho_i}{\sum_{ijk}\tilde{A}^{(2)}_{ijk}\rho_i\rho_j\rho_k}, \qquad (\alpha > 2),\end{aligned} \tag{4.45}$$

Putting together (4.40) and (4.45), we have in both cases $\tilde{\mu}_l^{(0)} \sim e^{\alpha l}$, with

$$\alpha = \begin{cases} 2 - \frac{2\sum c_i\rho_i}{t_0\sum_{ijk}\tilde{A}^{(1)}_{ijk}\rho_i\rho_j\rho_k} & , \sum_i c_i\rho_i > 0 \\ \left[\frac{1}{2} + \frac{\sum_i c_i\rho_i}{\sum_{ijk}\tilde{A}^{(2)}_{ijk}\rho_i\rho_j\rho_k}\right]^{-1} & , \sum_i c_i\rho_i < 0. \end{cases} \tag{4.46}$$

We see from (4.46) that, indeed, $\alpha < 2$ ($\alpha > 2$) when flowing toward a stable ray that satisfies $\sum_i c_i\rho_i > 0$ ($\sum_i c_i\rho_i > 0$), consistent with our initial assumption. Note that, for $\alpha < 2$, the chemical potential does not enter into the asymptotic flow equation for the coupling constants (4.35), so that the asymptotic analysis presented here matches exactly that from Ref. [105]. This means that, although the flow behavior at small l may determine which stable ray is approached, the particular ratios that define that ray, as well as the universal properties such as critical exponents associated with it, are independent of the chemical potential. On the other hand, for $\alpha > 2$, the temperature doesn't appear at all in the asymptotic analysis, and the $l \to \infty$ behavior depends only on the chemical potential. We shall find in the following section that all instabilities for which $\alpha > 2$ are to superconducting phases. The fate of the system at low energies thus depends in a crucial way on the competition between temperature and chemical potential to be the most relevant variable, and the winner of this competition ultimately determines which phase will be realized. This competition is missed entirely by the more common RG approaches with $T = 0$, which tend to favor superconducting instabilities away from special situations with

Fermi surface nesting. Our analysis thus suggests that the inclusion of nonzero temperature in the RG framework in this sense levels the playing field between particle-hole and particle-particle instabilities.

4.4.2 Susceptibilities and symmetry breaking

As in Ref. [105], we investigate possible types of symmetry breaking by introducing source terms to the action:

$$\begin{aligned}\Delta S = &\sum_{i=1}^{18} \Delta_i^{ph} T \sum_n \sum_{\mathbf{k}} \psi^\dagger(i\omega_n, \mathbf{k}) O_{ph}^{(i)} \psi(i\omega_n, \mathbf{k}) \\ &+ \frac{1}{2} \sum_{i=1}^{9} \Delta_i^{pp} T \sum_n \sum_{\mathbf{k}} \left[\psi^\dagger(i\omega_n, \mathbf{k}) O_{pp}^{(i)} \psi^*(-i\omega_n, -\mathbf{k}) + c.c. \right].\end{aligned} \tag{4.47}$$

The matrices $O_{pp}^{(i)}$ for the particle-particle vertices are given in Table 4.2. (The corresponding table for particle-hole terms is given in Ref. [105].) The flow equations for the particle-hole source terms are then given by

$$\begin{aligned}\frac{d \ln \Delta_i^{ph}}{dl} = 2 + \sum_{j=1}^{9} g_j(l) \sum_{m=1}^{2} \Big[&\left(B_{ij}^{(1)}(m) + B_{ij}^{(2)}(m) \right) f_{ph}^{(1)}(t_l, \tilde{\mu}_l^{(0)}) \\ &+ \left(B_{ij}^{(1)}(m) + B_{ij}^{(2)}(m) \right) f_{ph}^{(2)}(t_l, \tilde{\mu}_l^{(0)}) \Big],\end{aligned} \tag{4.48}$$

where the coefficients $B_{ij}^{(1,2)}(m)$ were originally derived in Ref. [105] and are reproduced in Appendix A. (The index m refers to the first two diagrams in Figure 4.5.) The flows for the particle-particle source terms, corresponding to the third diagram in Figure 4.5, are given by

$$\frac{d \ln \Delta_i^{pp}}{dl} = 2 + \sum_{j=1}^{9} g_j(l) \left[\left(C_{ij}^{(1)} + C_{ij}^{(2)} \right) f_{pp}^{(1)}(t_l, \tilde{\mu}_l^{(0)}) + \left(C_{ij}^{(1)} + C_{ij}^{(2)} \right) f_{pp}^{(2)}(t_l, \tilde{\mu}_l^{(0)}) \right], \tag{4.49}$$

where the coefficients $C_{ij}^{(1,2)}$ are identical to $\tilde{B}_{ij}^{(1,2)}$ in Ref. [105] and are also reproduced in Appendix A. As with the other flow equations, the asymptotic behavior of (4.48) and

Group rep.	Spin	Matrices	Name
A_{1g}	singlet	$\tau_1 1 s_2$	s_{++}
A_{2g}	triplet	$-\tau_2\sigma_3 1$	$f_{\pm}$
E_g	singlet	$\tau_1\sigma_1 s_2, \tau_2\sigma_2 s_2$	$d_{x^2-y^2}, d_{xy}$
A_{1u}	triplet	$-\tau_2 11$	f_{++}
A_{2u}	singlet	$-\tau_1\sigma_3 s_2$	$s_{\pm}$
E_u	triplet	$\tau_2\sigma_1 1, \tau_1\sigma_2 1$	p_x, p_y
$A_{1\mathbf{K}}$	singlet	$1\sigma_1 s_2, \tau_3\sigma_1 s_2$	s-PDW
$A_{2\mathbf{K}}$	triplet	$-1\sigma_2 1, \tau_3\sigma_2 1$	p-PDW
$E_{\mathbf{K}}$	singlet	$11 s_2, \tau_3\sigma_3 s_2, \tau_3 1 s_2, 1\sigma_3 s_2$	d-PDW

Table 4.2: Particle-particle phases, together with associated matrices appearing in (4.47), listed according to the representation of the D_{3d} point group under which they transform (those with subscript $\mathbf{K}$ transform instead according to D_3).

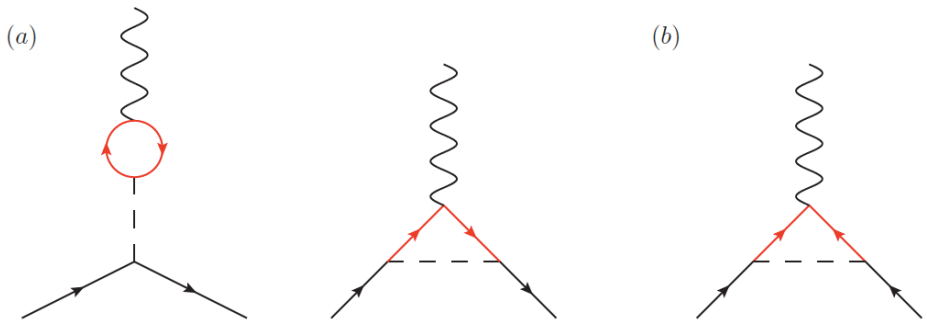

Figure 4.5: Diagrams contributing to the flow equations for the particle-hole (a) and particle-particle (b) source terms.

(4.49) must be analyzed separately for the cases $\alpha < 2$ and $\alpha > 2$.

For $\alpha < 2$, using (4.34) the vertex flow equations become

$$\begin{aligned} \frac{d\ln\Delta_i^{ph}}{dl} &\overset{(l\to\infty)}{=} 2 + \frac{1}{t_l}\sum_{j=1}^{9}\tilde{B}_{ij}g_j(l), \\ \frac{d\ln\Delta_i^{pp}}{dl} &\overset{(l\to\infty)}{=} 2 + \frac{1}{t_l}\sum_{j=1}^{9}\tilde{C}_{ij}g_j(l), \end{aligned} \tag{4.50}$$

where

$$\begin{aligned} \tilde{B}_{ij} &= \sum_{m=1}^{2}\left[B_{ij}^{(1)}(m) + B_{ij}^{(2)}(m)\right], \\ \tilde{C}_{ij} &= C_{ij}^{(1)} + C_{ij}^{(2)}. \end{aligned} \tag{4.51}$$

Note that these results are again independent of the chemical potential, so that the universal features of the critical behavior are for $\alpha < 2$ identical to those established by Ref. [105]. For $\alpha > 2$, on the other hand, using (4.41) the vertex flow equations (4.48) and (4.49) become

$$\begin{aligned} \frac{d\ln\Delta_i^{ph}}{dl} &\overset{(l\to\infty)}{=} 2, \\ \frac{d\ln\Delta_i^{pp}}{dl} &\overset{(l\to\infty)}{=} 2 + \frac{2}{\tilde{\mu}_l^{(0)}}\sum_{j=1}^{9}\tilde{C}_{ij}g_j(l). \end{aligned} \tag{4.52}$$

Putting these results together, and using (4.39) and (4.44), the vertex flow equations can be expressed as

$$\frac{d\ln\Delta_i^{ph,pp}}{dl} \overset{(l\to\infty)}{=} \begin{cases} 2 + \eta_i^{ph,pp}, & \alpha < 2, \\ 2 + \alpha\eta_i^{ph,pp}/2, & \alpha > 2, \end{cases} \tag{4.53}$$

with the anomalous critical exponents given by

$$\eta_i^{ph} = \begin{cases} \frac{2\sum_j \tilde{B}_{ij}\rho_j}{\sum_{ijk}\tilde{A}_{ijk}^{(1)}\rho_i\rho_j\rho_k}, & \alpha < 2, \\ 0, & \alpha > 2, \end{cases} \tag{4.54}$$

$$\eta_i^{pp} = \begin{cases} \frac{2\sum_j \tilde{C}_{ij}\rho_j}{\sum_{ijk}\tilde{A}^{(1)}_{ijk}\rho_i\rho_j\rho_k}, & \alpha < 2 \\ \frac{2\sum_j \tilde{C}_{ij}\rho_j}{\sum_{ijk}\tilde{A}^{(2)}_{ijk}\rho_i\rho_j\rho_k}, & \alpha > 2. \end{cases} \tag{4.55}$$

It can be shown following the method of Ref. [105] that, as the critical temperature is approached, the corresponding susceptibilities behave as

$$\chi_i^{ph,pp} \sim (t_0 - t_c)^{-\gamma_i^{ph,pp}}, \tag{4.56}$$

with

$$\gamma_i^{ph,pp} = \eta_i^{ph,pp} - 1. \tag{4.57}$$

Thus the condition for a diverging susceptibility is that $\eta_i^{ph,pp} > 1$, with mean-field behavior realized for $\eta_i^{ph,pp} = 2$.

Due to the fact that $\eta_i^{ph} = 0$ when $\alpha > 2$, there can be no instability in any particle-hole channel in this case. Thus *only* particle-particle instabilities may occur when $\alpha > 2$, i.e. when the flow of the chemical potential under RG is more relevant than the flow of temperature. This could in fact be inferred already from (4.42), which shows that only the particle-particle ladder diagrams contribute to the asymptotic flows for $\alpha > 2$.

4.4.3 Discussion

Let us summarize and discuss the results obtained in the previous two subsections. In analyzing the asymptotic flow equations, one finds two distinct regimes with very different behaviors. In the first, which occurs for sufficiently small values of the bare chemical potential, we find that $\mu_{l\to\infty} \sim e^{\alpha l}$, with $\alpha < 2$, and the diverging couplings blowing up as $g_i(l \to \infty) \sim e^{2l}$. Due to the fact that μ_l and v_{3l} are both less relevant than temperature,

the coefficients in the flow equations depend only on temperature as $l \to \infty$. Thus, while the presence of a chemical potential may affect nonuniversal properties such as the critical temperature and may even nudge the RG flow toward a different phase, the universal properties such as the critical exponents and the possible phases that can be realized do not depend on μ in this regime. We thus recover the fixed ratios and associated phases, almost all of which correspond to particle-hole instabilities, from the half-filled case described in Ref. [105].

In the second regime, which occurs for sufficiently large bare values of the chemical potential, we again find that $\mu_{l\to\infty} \sim e^{\alpha l}$, but now with $\alpha > 2$, while for the diverging couplings, $g_i(l \to \infty) \sim e^{\alpha l}$. In this case the chemical potential is *more* relevant than temperature, and the flow equation coefficients turn out to depend only on μ_l. In this limit, only the particle-particle ladder diagrams from Figure 4.4 contribute to the flow equations for the couplings, and the critical exponents assume their mean-field values ($\eta_i^{ph} = 0$, and $\eta_i^{pp} = 2$ in the divergent channel). The couplings then approach an entirely different set of fixed ratios, all of which correspond to superconducting instabilities. There are 9 of these fixed ratios, which are listed explicitly in Table 4.3, with one corresponding to each irreducible representation. The coupling ratios for all of these phases satisfy $\sum_i c_i \rho_i < 0$. Further insight into these particle-particle instabilities may be obtained by noting that the original interaction term (4.8) can be rewritten as a sum of interactions in particle-particle interaction terms. By rearranging the fermion operators and employing the Fierz transformation,

$$\tilde{g}_i = F_{ij} g_j, \tag{4.58}$$

Group rep.	ρ_1	ρ_2	ρ_3	ρ_4	ρ_5	ρ_6	ρ_7	ρ_8	ρ_9
A_{1g}	-	+	-	+	-	+	-	+	-
A_{2g}	-	+	+	+	-	-	-	+	+
E_g	-	-	0	+	+	0	-	-	0
A_{1u}	-	+	-	+	-	+	+	-	+
A_{2u}	-	+	+	+	-	-	+	-	-
E_u	-	-	0	+	+	0	+	+	0
$A_{1\mathbf{K}}$	-	+	-	-	+	-	0	0	0
$A_{2\mathbf{K}}$	-	+	+	-	+	+	0	0	0
$E_{\mathbf{K}}$	-	-	0	-	-	0	0	0	0

Table 4.3: Fixed coupling ratios for particle-particle phases with $\alpha > 2$. Because all of the magnitudes of the nonzero couplings are equal as $l \to \infty$, only the signs of the couplings are given.

the interaction term can be rewritten as

$$S_{\text{int}} = \sum_{i=1}^{9} \frac{\tilde{g}_i}{2} \sum_{m=1}^{m_i} \int d^2x \int d\tau \left(\psi^\dagger(x,\tau) \Gamma_i^m \psi^*(x,\tau) \right) \left(\psi^T(x,\tau) \Gamma_i^m \psi(x,\tau) \right). \tag{4.59}$$

The transformation matrix in (4.58) is given by

$$F = \frac{1}{8} \begin{pmatrix} 1 & -1 & 2 & -1 & 1 & -2 & 2 & -2 & 4 \\ 1 & -1 & -2 & -1 & 1 & 2 & 2 & -2 & -4 \\ 1 & 1 & 0 & -1 & -1 & 0 & 2 & 2 & 0 \\ 1 & -1 & 2 & -1 & 1 & -2 & -2 & 2 & -4 \\ 1 & -1 & -2 & -1 & 1 & 2 & -2 & 2 & 4 \\ 1 & 1 & 0 & -1 & -1 & 0 & -2 & -2 & 0 \\ 1 & -1 & 2 & 1 & -1 & 2 & 0 & 0 & 0 \\ 1 & -1 & -2 & 1 & -1 & -2 & 0 & 0 & 0 \\ 1 & 1 & 0 & 1 & 1 & 0 & 0 & 0 & 0 \end{pmatrix}, \tag{4.60}$$

where the matrix operates on the 9 couplings arranged in the order that they appear in Table 4.3. In this new basis, each combination of stable fixed coupling ratios from Table 4.3 corresponds to a *single* diverging coupling $\tilde{g}_i$. In addition, it is straightforward to verify that—apart from the A_{1g} particle-hole charge instability—all of the fixed ratios from Ref. [105], including the entire "target plane," satisfy $\sum_i c_i \rho_i > 0$.

4.5 Phase diagrams without trigonal warping

In general, the form of the interaction between fermions is determined by the bare ($l = 0$) values of the nine coupling constants. For repulsive density-density interactions, the largest bare couplings will be those corresponding to the A_{1g}, A_{2u}, and $E_{\mathbf{K}}$ representations,

with the first of these being the largest. Letting $V_\parallel(\mathbf{q})$ and $V_\perp(\mathbf{q})$ denote the momentum-dependent intralayer and interlayer density-density interaction, respectively, it can be shown that [109]

$$\begin{aligned} g_{A_{1g}} &= \frac{1}{2}[V_\parallel(\mathbf{q}\approx 0) + V_\perp(\mathbf{q}\approx 0)] \\ g_{A_{2u}} &= \frac{1}{2}[V_\parallel(\mathbf{q}\approx 0) - V_\perp(\mathbf{q}\approx 0)] \\ g_{E_\mathbf{K}} &= \frac{1}{4}V_\parallel(\mathbf{q}\approx 2\mathbf{K}). \end{aligned} \tag{4.61}$$

In the presence of metallic gates above and/or below the sample, the bare Coulomb interaction will be screened, resulting in an interaction that decays with some characteristic length ξ. Previous RG analyses of the undoped system have shown that the nematic phase is favored in the forward scattering limit, where $\xi \gg a$ (a is the lattice constant), while the antiferromagnetic phase is favored for $\xi \sim a$, corresponding to the Hubbard interaction limit [105, 109].

Let us first consider the forward scattering limit, in which the bare coupling $g_{A_{1g}}$ is much greater than all other couplings. Detailed analysis of the flow equations indicates that, if all other bare couplings are strictly zero, then the only other couplings that are generated under RG are $g_{A_{2g}}$ and g_{E_g}, with the other six couplings remaining equal to zero. This presents a problem, however, in that all of the stable coupling ratios for the superconducting phases shown in Table 4.3 require more than just these three couplings to be nonzero. We conclude that any superconducting phase found starting from the pure forward scattering limit is unstable, in the sense that small perturbations to the bare coupling values will in general cause the system to flow to another phase. Thus, rather than focusing on such fine-tuned and physically irrelevant cases, we begin by investigating the "near-forward

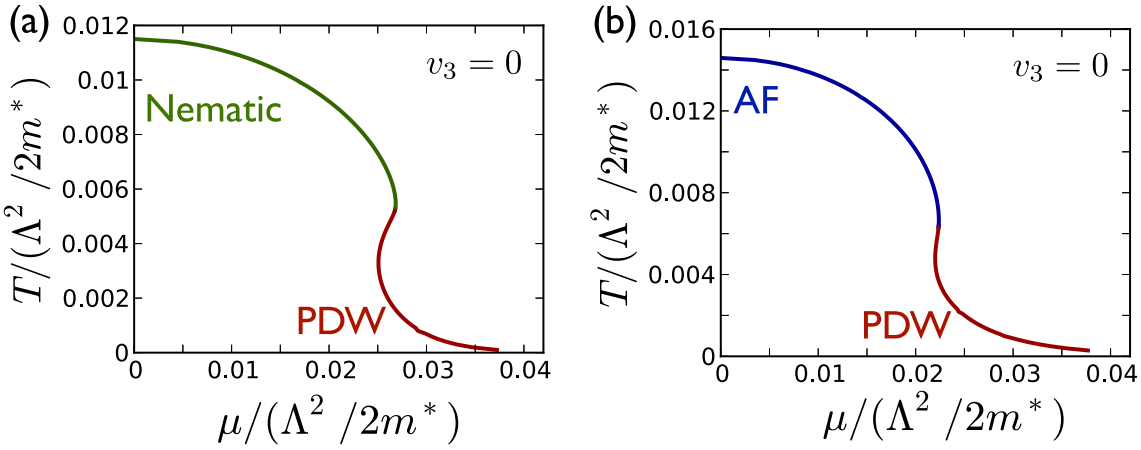

Figure 4.6: (a) Phase diagram showing nematic (E_g) and superconducting pair density wave ($A_{1\mathbf{K}}$) instabilities in the absence of trigonal warping. The bare interaction corresponds to the near-forward scattering limit, with $\frac{m^*}{4\pi} g_{A_{1g}}(l=0) = 0.15$ and $\frac{m^*}{4\pi} g_{A_{2u}}(l=0) = \frac{m^*}{4\pi} g_{E_{\mathbf{K}}}(l=0) = 0.003$. (b) Phase diagram showing antiferromagnetic (A_{2u}) and pair density wave ($A_{1\mathbf{K}}$) superconducting instabilities in the absence of trigonal warping. The bare A_{1g} coupling is $\frac{m^*}{4\pi} g_{A_{1g}}(l=0) = 0.06$, with $g_{A_{2u}}(0) = g_{A_{1g}}(0)$ and $g_{E_{\mathbf{K}}}(0) = \frac{1}{2} g_{A_{1g}}(0)$, corresponding to Hubbard interaction.

scattering" limit, where it is assumed that all three of the bare density-density couplings in (4.61) are nonzero, with $g_{A_{1g}}$ being much larger than the others. In this case, the remaining six couplings are all generated under the RG flow. The phase diagram corresponding to this scenario is shown in Figure 4.6(a). For small chemical potential μ, the dominant instability is toward the nematic phase, which transforms under the E_g representation in the particle-hole channel. This phase has previously been predicted theoretically [100, 101], and there have been recent claims that it has been realized experimentally [97]. As μ is increased, the nematic instability is suppressed, giving way to a superconducting instability.

This superconducting phase, which transforms according to the $A_{1\mathbf{K}}$ representation, is a pair density wave (PDW) state, in which the Cooper pairs are formed by electrons with momenta $\mathbf{K}+\mathbf{k}$ and $\mathbf{K}-\mathbf{k}$. The pairs thus carry a nonzero net momentum, which

leads to spatial modulation of the order parameter. The two components of this representation behave as $\Delta^{(1)}_{A_{1\mathbf{K}}}(\mathbf{x}) \sim \cos(2\mathbf{K}\cdot\mathbf{x})$ and $\Delta^{(2)}_{A_{1\mathbf{K}}}(\mathbf{x}) \sim \sin(2\mathbf{K}\cdot\mathbf{x})$. In the case that these two components coexist, the amplitude of the condensate remains constant, while the phase modulates as $\sim e^{\pm 2i\mathbf{K}\cdot\mathbf{x}}$. The idea of such spatially modulated superconducting phases was first proposed by Fulde, Ferrel, Larkin, and Ovchinnikov [112, 113], and the realization of such a state has been a longstanding experimental challenge. This exotic superconducting phase is unlikely to be observed experimentally in bilayer graphene, however. As we shall see in the following section, the PDW is suppressed by trigonal warping, which spoils the intrapocket symmetry between electron states at $\mathbf{K} \pm \mathbf{k}$.

The phase diagram remains qualitatively similar, with instabilities to the antiferromagnetic and PDW phases, as $g_{A_{2u}}$ and $g_{E_{\mathbf{K}}}$ are increased further, all the way up to the limit of completely local Hubbard interaction, for which the nonzero bare couplings are $g_{A_{1g}} = g_{A_{2u}} = 2g_{E_{\mathbf{K}}}$. These couplings are related to the usual Hubbard interaction via the relation $U = 2g_{A_{1g}}$. The phase diagram corresponding to Hubbard interaction is shown in Figure 4.6(b), and includes antiferromagnetic and PDW phases.

4.6 Effects of trigonal warping

The phase diagrams calculated in Section 4.5 apply to a bilayer honeycomb lattice with parabolic bands touching at the $\pm\mathbf{K}$ points in the Brillouin zone. In bilayer graphene, however, it is known that the spectrum contains a term linear in momentum that distorts the parabolic bands. This so-called "trigonal warping," which arises due to interlayer hopping between non-dimerized sites (γ_3 in Figure 4.2), distorts the electron spectrum at low

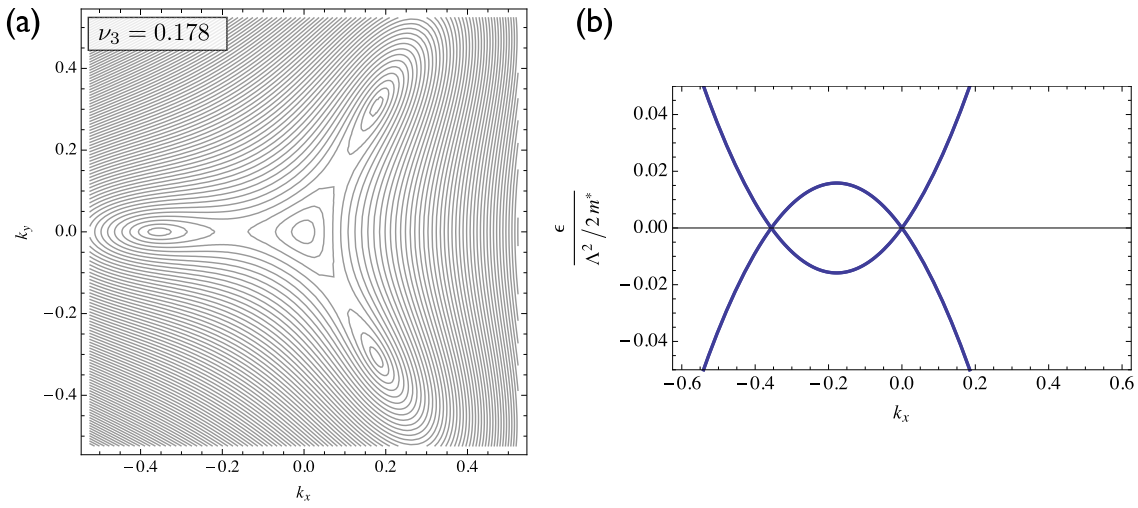

Figure 4.7: (a) Low-energy electronic dispersion near the **K** point at the corner of the Brillouin zone with nonzero trigonal warping, leading to four nodal points. The contours of constant energy are spaced by $0.005\Lambda^2/2m^*$. The corresponding dispersion at $-\mathbf{K}$ is obtained by reflecting $k_x \to -k_x$. (b) Dispersion along the line $k_y = 0$, with the same parameters as in (a).

energies, so that the Fermi surfaces are no longer circular and perfectly nested, but rather exhibit dispersion as shown in Figure 4.7, with the parabolic spectrum replaced by four Dirac minicones near each point $\pm\mathbf{K}$. Taking into account the effects of trigonal warping is crucial to determining the extent to which the phases that have been found thus far depend on having a fine-tuned band structure, or whether they are robust against distortions leading to imperfect nesting, thus having a much greater chance of being realized in actual materials. Taking the trigonal warping into account, we proceed to calculate the flow equations as in Section 4.3, but now using the full fermionic Green function (4.7), with $v_3 \neq 0$. It shall be convenient to define the dimensionless quantity $\nu_3 \equiv v_3/(\Lambda/2m^*)$. Tree-level RG scaling of the noninteracting action (4.6) dictates that the trigonal warping flows according

to $d\nu_3(l)/dl = \nu_3(l)$, so that

$$\nu_3(l) = \nu_3(0)e^l. \tag{4.62}$$

In much of what follows, we shall focus our attention on the experimentally determined [97] value $\nu_3(0) = 0.178$.

4.6.1 Temperature dependence of the chemical potential

Let us make a brief aside in order to note that, due to the fact that we are interested in slight deviations away from half-filling, it is necessary to keep in mind the relation between particle density n and chemical potential μ, which is nontrivial at finite temperature. Typically the dependence of chemical potential on temperature is small if $\mu \gg T$, but it is necessary to consider it in the case where $\mu \sim T$, which is the regime of interest here. As pointed out in Section 4.3.2, μ turns out to be independent of T for the case of parabolic dispersion, but this is no longer the case when $\nu_3 \neq 0$.

A straightforward calculation leads to the following expression for the particle density:

$$n = 4\int^{\Lambda} \frac{d^2k}{(2\pi)^2}\left[n_F(\xi_{\mathbf{k}} - \mu) + n_F(-\xi_{\mathbf{k}} - \mu)\right], \tag{4.63}$$

where the factor of 4 is due to spin and valley degeneracy, and

$$\xi_{\mathbf{k}} = \sqrt{\varepsilon_{\mathbf{k}}^2 + v_3^2k^2 + 2v_3k\varepsilon_{\mathbf{k}}\cos 3\theta_{\mathbf{k}}}. \tag{4.64}$$

If the particle density is held constant as temperature is varied, then (4.63) implies that μ must adjust accordingly in order to keep the right hand side of the equation constant as well. Thus we have $\mu = \mu(T)$. Figure 4.8 shows the contours of constant fermion

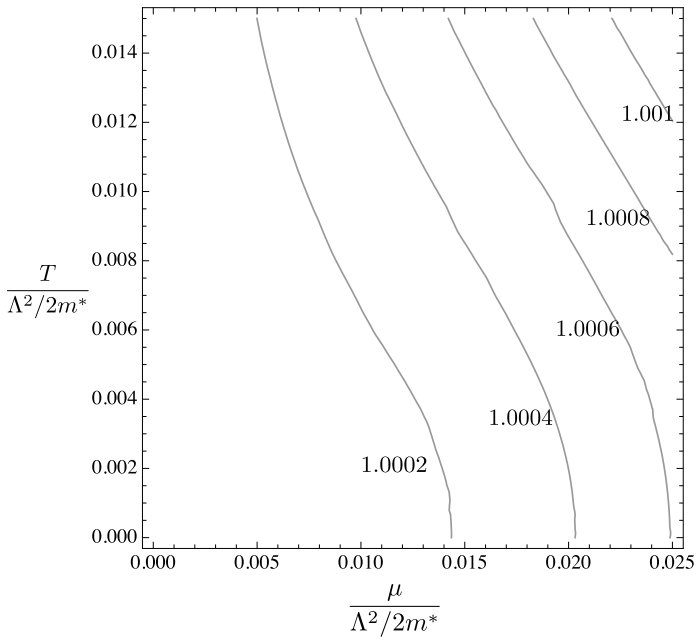

Figure 4.8: Contours of constant fermion density with trigonal warping velocity $v_3 = 0.178\Lambda/2m^*$. The line $\mu = 0$ corresponds to half-filling, with $n = 1$.

density n as chemical potential and temperature are varied. We see that, for the energy scales ($\sim$meV) that we are interested in, the characteristic amount of doping required to suppress particle-hole order and induce superconductivity is $\Delta n \sim 10^{-4}$ carriers per site. This translates to $\Delta n \sim 10^{12}$ cm^{-2}, which is well within the resolution that can be obtained experimentally [97].

4.6.2 Flow equations with $\nu_3 \neq 0$

We proceed to derive the flow equations as in Section 4.3, but now in the presence of nonzero trigonal warping. Using (4.7), the loop integral over modes at large momenta

gives

$$
\begin{aligned}
& T\sum_n \int_{\Lambda(1-dl)}^{\Lambda} \frac{dkk}{2\pi}\int_0^{2\pi}\frac{d\theta_{\mathbf{k}}}{2\pi} G_0(i\omega_n,\mathbf{k})\otimes G_0(\pm i\omega_n,\pm\mathbf{k}) \\
&= \frac{m^*}{8\pi}dl\Big\{ \mp 1_8\otimes 1_8\left[F^{(1)}_{ph,pp}+F^{(2)}_{ph,pp}\right] \\
&\qquad\qquad + \frac{1}{2}(1\sigma_1 1\otimes 1\sigma_1 1+\tau_3\sigma_2 1\otimes\tau_3\sigma_2 1)\left[F^{(3)}_{ph,pp}+F^{(4)}_{ph,pp}\right]\Big\} \\
&\quad + \frac{m^*}{8\pi}dl\Big\{ -\tau_3 1_4\otimes\tau_3 1_4\left[F^{(1)}_{ph,pp}-F^{(2)}_{ph,pp}\right] \\
&\qquad\qquad \pm \frac{1}{2}(\tau_3\sigma_1 1\otimes\tau_3\sigma_1 1+1\sigma_2 1\otimes 1\sigma_2 1)\left[F^{(4)}_{ph,pp}-F^{(3)}_{ph,pp}\right]\Big\},
\end{aligned}
\tag{4.65}
$$

where the upper and lower signs correspond to the particle-hole and particle-particle cases, respectively. The F functions in (4.65) are defined as

$$
\begin{aligned}
F^{(1)}_{ph,pp}(t,\tilde{\mu},\nu_3) &= \frac{1}{2\pi t}\int_{-1}^{1}\frac{dx}{\sqrt{1-x^2}}\Upsilon^{(1)}_{ph,pp}(t,\tilde{\mu},\nu_3,x) \\
F^{(2)}_{ph,pp}(t,\tilde{\mu},\nu_3) &= \frac{1}{2\pi\nu_3}\int_{-1}^{1}\frac{dx}{\sqrt{1-x^2}}\frac{1}{x}\Upsilon^{(2)}_{ph,pp}(t,\tilde{\mu},\nu_3,x) \\
F^{(3)}_{ph,pp}(t,\tilde{\mu},\nu_3) &= \frac{1-\nu_3^2}{2\pi\nu_3}\int_{-1}^{1}\frac{dx}{\sqrt{1-x^2}}\frac{1}{x}\Upsilon^{(3)}_{ph,pp}(t,\tilde{\mu},\nu_3,x) \\
F^{(4)}_{ph,pp}(t,\tilde{\mu},\nu_3) &= \frac{1}{2\pi t}\int_{-1}^{1}\frac{dx}{\sqrt{1-x^2}}\Upsilon^{(4)}_{ph,pp}(t,\tilde{\mu},\nu_3,x),
\end{aligned}
\tag{4.66}
$$

where

$$\begin{aligned}
\Upsilon^{(1)}_{ph}(t,\tilde{\mu},\nu_3,x) &= \frac{1}{2}\left[\frac{1}{\cosh^2\left(\frac{Q_+-\tilde{\mu}}{2t}\right)}+\frac{1}{\cosh^2\left(\frac{Q_++\tilde{\mu}}{2t}\right)}\right] \\
&\quad + \frac{t}{Q_+}\left[\tanh\left(\frac{Q_+-\tilde{\mu}}{2t}\right)+\tanh\left(\frac{Q_++\tilde{\mu}}{2t}\right)\right] \\
\Upsilon^{(2)}_{ph}(t,\tilde{\mu},\nu_3,x) &= \frac{1}{2}\sum_{\lambda=\pm}\lambda Q_\lambda\left[\tanh\left(\frac{Q_\lambda-\tilde{\mu}}{2t}\right)+\tanh\left(\frac{Q_\lambda+\tilde{\mu}}{2t}\right)\right] \\
\Upsilon^{(3)}_{ph}(t,\tilde{\mu},\nu_3,x) &= -\frac{1}{2}\sum_{\lambda=\pm}\frac{\lambda}{Q_\lambda}\left[\tanh\left(\frac{Q_\lambda-\tilde{\mu}}{2t}\right)+\tanh\left(\frac{Q_\lambda+\tilde{\mu}}{2t}\right)\right] \\
\Upsilon^{(4)}_{ph}(t,\tilde{\mu},\nu_3,x) &= -\frac{1}{2}\left[\frac{1}{\cosh^2\left(\frac{Q_+-\tilde{\mu}}{2t}\right)}+\frac{1}{\cosh^2\left(\frac{Q_++\tilde{\mu}}{2t}\right)}\right] \\
&\quad + \frac{t}{Q_+}\left[\tanh\left(\frac{Q_+-\tilde{\mu}}{2t}\right)+\tanh\left(\frac{Q_++\tilde{\mu}}{2t}\right)\right]
\end{aligned} \tag{4.67}$$

and

$$\begin{aligned}
\Upsilon^{(1)}_{pp}(t,\tilde{\mu},\nu_3,x) &= \frac{t}{\tilde{\mu}}\left[\frac{Q_++2\tilde{\mu}}{Q_++\tilde{\mu}}\tanh\left(\frac{Q_++\tilde{\mu}}{2t}\right)-\frac{Q_+-2\tilde{\mu}}{Q_+-\tilde{\mu}}\tanh\left(\frac{Q_+-\tilde{\mu}}{2t}\right)\right] \\
\Upsilon^{(2)}_{pp}(t,\tilde{\mu},\nu_3,x) &= 2\nu_3 x\sum_{\lambda=\pm}\left[\frac{Q_\lambda-2\tilde{\mu}}{(Q_\lambda-2\tilde{\mu})^2-Q^2_{-\lambda}}\tanh\left(\frac{Q_\lambda-\tilde{\mu}}{2t}\right)\right. \\
&\qquad \left. + \frac{Q_\lambda+2\tilde{\mu}}{(Q_\lambda+2\tilde{\mu})^2-Q^2_{-\lambda}}\tanh\left(\frac{Q_\lambda+\tilde{\mu}}{2t}\right)\right] \\
\Upsilon^{(3)}_{pp}(t,\tilde{\mu},\nu_3,x) &= -2\nu_3 x\sum_{\lambda=\pm}\frac{1}{Q_\lambda}\left[\frac{1}{(Q_\lambda-2\tilde{\mu})^2-Q^2_{-\lambda}}\tanh\left(\frac{Q_\lambda-\tilde{\mu}}{2t}\right)\right. \\
&\qquad \left. + \frac{1}{(Q_\lambda+2\tilde{\mu})^2-Q^2_{-\lambda}}\tanh\left(\frac{Q_\lambda+\tilde{\mu}}{2t}\right)\right] \\
\Upsilon^{(4)}_{pp}(t,\tilde{\mu},\nu_3,x) &= \frac{tQ_+}{\tilde{\mu}}\left[\frac{1}{Q_+-\tilde{\mu}}\tanh\left(\frac{Q_+-\tilde{\mu}}{2t}\right)-\frac{1}{Q_++\tilde{\mu}}\tanh\left(\frac{Q_++\tilde{\mu}}{2t}\right)\right]
\end{aligned} \tag{4.68}$$

with

$$Q_\pm = \sqrt{1+\nu_3^2\pm 2\nu_3 x}. \tag{4.69}$$

In the limit of vanishing chemical potential, one recovers the previous results of Ref. [105]:

$$F^{(i)}_{ph,pp}(t,\tilde{\mu}=0,\nu_3) = \Phi_i(t,\nu_3). \tag{4.70}$$

Similarly, these functions reduce to the $f^{(i)}_{ph,pp}(t,\tilde{\mu})$ defined in Equation 4.21 in the limit $\nu_3 \to 0$.

With these expressions in hand, we can proceed by solving the flow equations as before, replacing $f^{(i)}_{ph,pp}(t,\tilde{\mu}) \to F^{(i)}_{ph,pp}(t,\tilde{\mu},\nu_3)$. As before, we can again replace $\tilde{\mu}_l \to \tilde{\mu}^{(0)}_l$ in the flow equations, neglecting the interaction-induced part of the chemical potential at the order to which we are working. The flow of the chemical potential for $\nu_3 \neq 0$ is still given by (4.30), with the only difference being that one must perform the following angular average:

$$K(\tilde{\mu}^{(0)}_l, t_l) = 1 + \frac{1}{2\pi}\int_{-1}^{1} \frac{dx}{\sqrt{1-x^2}} \left[\tanh\left(\frac{Q_+ + \tilde{\mu}^{(0)}_l}{2t_l}\right) - \tanh\left(\frac{Q_+ - \tilde{\mu}^{(0)}_l}{2t_l}\right)\right]. \quad (4.71)$$

Due to the fact that the trigonal warping coefficient flows under RG as $\nu_3(l) \sim e^l$, which is always less relevant than temperature, the functions $F^{(i)}_{ph,pp}$ do not depend on ν_3 as $l \to \infty$. This means that the asymptotic analysis from Section 4.4 applies to the case with nonzero trigonal warping as well. Thus, while nonuniversal properties such as the critical temperature may change due to nonzero ν_3, the universal critical properties such as the coupling ratios and exponents corresponding to the various phases remain unaffected.

4.7 Phase diagrams with trigonal warping

The phase diagram shown in Figure 4.9(a) illustrates the effects of trigonal warping on the nematic and superconducting phases for the near-forward scattering case. The particle-hole phase, as in the $\nu_3 = 0$ case from Section 4.5, is a nematic. Rather than the PDW as before, however, this phase gives way upon doping to an f-wave superconducting state, transforming under the A_{1u} representation (cf. Table 4.2).

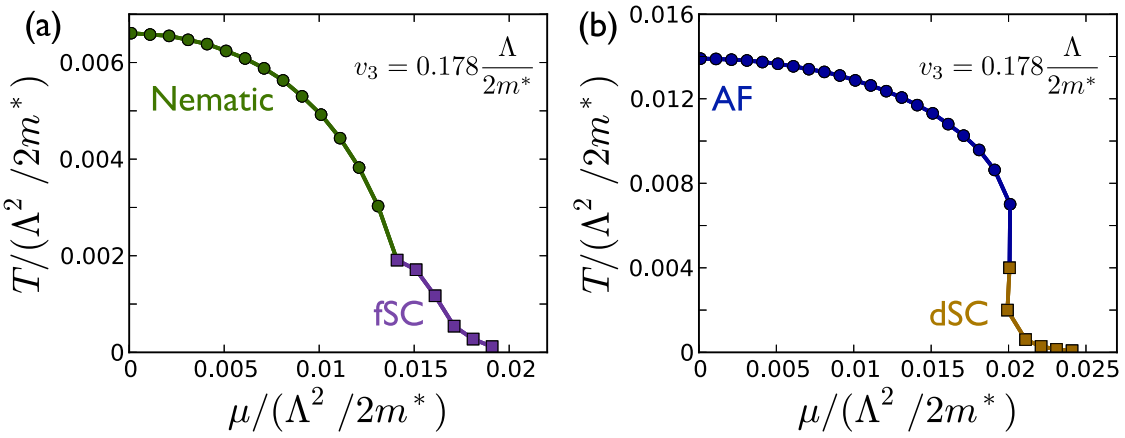

Figure 4.9: (a) Phase diagram showing nematic (E_g) and f-wave superconducting (A_{1u}) instabilities with trigonal warping $v_3 = 0.178\Lambda/2m^*$. The bare couplings are $\frac{m^*}{4\pi}g_{A_{1g}}(l = 0) = 0.15$, $\frac{m^*}{4\pi}g_{A_{2u}}(l = 0) = \frac{m^*}{4\pi}g_{A_{E_{\mathbf{K}}}}(l = 0) = 0.003$. (b) Phase diagram showing antiferromagnetic (A_{2u}) and d-wave (E_g) superconducting instabilities with trigonal warping $v_3 = 0.178\Lambda/2m^*$. The bare A_{1g} coupling is $\frac{m^*}{4\pi}g_{A_{1g}}(l = 0) = 0.06$, with $g_{A_{2u}}(0) = g_{A_{1g}}(0)$ and $g_{E_{\mathbf{K}}}(0) = \frac{1}{2}g_{A_{1g}}(0)$, corresponding to Hubbard interaction.

The phase diagram shown in Figure 4.9(b) illustrates the effects of trigonal warping on the competing antiferromagnetic and superconducting phases that arise from a bare Hubbard interaction. The appearance of antiferromagnetic order adjacent to a d-wave superconducting phase is reminiscent of the phase diagram of the high-temperature cuprate superconductors shown in Figure 4.1. In Section 4.8.1 it will be shown that this d-wave superconducting phase is chiral, with the two order parameter components coexisting in a manner that breaks time-reversal symmetry.

4.8 Nature of the superconducting phase

The RG calculations presented in the previous section led to two superconducting phases belonging to two-dimensional representations. For small trigonal warping v_3, both long- and short-ranged interactions were found to lead to a pair density wave (PDW)

phase, belonging to the $A_{1\mathbf{K}}$ space group representation. For larger v_3 and short-ranged interactions, we instead found a d-wave superconducting instability, belonging to the E_g representation. However, the RG approach used thus far is unable to determine which linear combination of the two order parameter components belonging to each representation will be realized. In order to determine this, we derive an effective Ginzburg-Landau (GL) free energy and minimize it in each case.

4.8.1 d-wave superconducting phase

For the case of d-wave superconductivity, an intriguing possibility is that the order parameter components might coexist, with a relative phase between them (denoted as $d_{x^2-y^2} + id_{xy}$, or simply "$d + id$"), thereby breaking time-reversal symmetry. Such chiral phases have been proposed in a variety of condensed matter systems, with the hope of providing a solid-state analogue to the well-established $p + ip$ superfluidity in the A phase of ^{3}He [114]. Such a phase has likely already been observed in Sr_2RuO_4 [115]. A chiral d-wave phase was first proposed in the context of high-temperature cuprate superconductors [116], and more recently there have been theoretical proposals of chiral s-wave phases in iron-based superconductors [117, 118]. Based on perturbative RG calculations, it was recently proposed that a time-reversal symmetry breaking combination of the two components ought to be realized in single-layer graphene doped to the van Hove point [119]. The possibility of $d + id$ superconductivity on the honeycomb bilayer has also been suggested recently [120], although the strong-coupling mean-field theory used in that study did not account for the origin of the effective attractive interaction, nor did it address the competition of d-wave superconductivity with other ordered phases. In this section we address the question of

whether chiral superconductivity can arise from repulsive interactions on the honeycomb bilayer via our weak-coupling RG analysis.

Due to the fact that only a single coupling corresponding to a single particle-particle channel diverges at the critical temperature when the system flows to a superconducting phase, as shown above by performing a Fierz transformation (4.58) on the couplings, it should be possible to describe the system accurately by performing a Hubbard-Stratonovich (HS) transformation, with the fermion interaction decoupled in the appropriate particle-particle channel. (This would not be possible if the system were flowing to one of the particle-hole fixed ratios, since fluctuations in multiple channels are important in this case, and by decoupling into any particular channel one would not be accounting for these other fluctuations.) After performing the HS decoupling, the action describing the system is

$$\begin{aligned} S_{\Delta,\psi} = T\sum_n \int \frac{d^2k}{(2\pi)^2} \Big\{ & \frac{1}{4\tilde{g}_{A_{1g}}}|\Delta_0|^2 + \frac{1}{4\tilde{g}_{E_g}}\left(|\Delta_1|^2+|\Delta_2|^2\right) \\ & + 2\big[\Delta_0^*(\psi_{\mathbf{K}1}s_2\psi_{-\mathbf{K}1}+\psi_{\mathbf{K}2}s_2\psi_{-\mathbf{K}2})+c.c.\big] \\ & + 2\big[(\Delta_1^*-i\Delta_2^*)\psi_{\mathbf{K}2}s_2\psi_{-\mathbf{K}1}+(\Delta_1^*+i\Delta_2^*)\psi_{\mathbf{K}1}s_2\psi_{-\mathbf{K}2}+c.c.\big]\Big\}, \end{aligned} \tag{4.72}$$

where $\Delta_{1,2}$ correspond to the $d_{x^2-y^2}$ and d_{xy} superconducting order parameter components, respectively; $\psi_{\pm\mathbf{K}a}$ are two-component spinors; and s_2 is the Pauli matrix that gives spin singlet pairing.[4] For reasons that will become apparent below, the order parameter for s-wave (A_{1g}) superconductivity, denoted as Δ_0, has also been included. Using Nambu spinor

[4]The two factors of i in (4.72) are included so that, if both order parameter components have the same phase, then the action is time-reversal invariant. This can be seen by noting that, since time-reversal changes $\mathbf{K}\to-\mathbf{K}$, the factor of i, which changes sign under time-reversal, is needed to compensate for the relative minus sign between the two places in the action where Δ_2 appears.

notation, the action can be written as

$$S_{\Delta,\psi} = T\sum_n \int \frac{d^2k}{(2\pi)^2} \Psi^\dagger_{n,k} \hat{\mathcal{G}}^{-1}_\Delta(i\omega_n, k)\Psi_{n,k} + \int d\tau \int d^2x \left[\frac{1}{4\tilde{g}_{A_{1g}}}|\Delta_0|^2 + \frac{1}{4\tilde{g}_{E_g}}\left(|\Delta_1|^2 + |\Delta_2|^2\right)\right] \quad (4.73)$$

The 8×8 Green function matrix is given by

$$\hat{\mathcal{G}}^{-1}_\Delta(i\omega_n, k) = \hat{\mathcal{G}}^{-1}_0(i\omega_n, k) + \hat{\Delta}(i\omega_n, k), \quad (4.74)$$

where

$$\begin{aligned}\hat{\mathcal{G}}^{-1}_0(i\omega_n, k) = &- i\omega_n 1_8 - \mu\rho_3 1 1 + \frac{k_x^2 - k_y^2}{2m^*}\rho_3 1\sigma_1 + \frac{k_x k_y}{m^*} 1\tau_3\sigma_2 \\ &+ v_3 k_x 1\tau_3\sigma_1 - v_3 k_y \rho_3 1\sigma_2\end{aligned} \quad (4.75)$$

is the bare Green function for fermions, and

$$\begin{aligned}\hat{\Delta} = &\mathrm{Re}\Delta_1\rho_1\tau_1\sigma_1 - \mathrm{Im}\Delta_1\rho_2\tau_1\sigma_1 + \mathrm{Im}\Delta_2\rho_1\tau_2\sigma_2 + \mathrm{Re}\Delta_2\rho_2\tau_2\sigma_2 \\ &+ \mathrm{Re}\Delta_0\rho_1\tau_1 1 + \mathrm{Im}\Delta_0\rho_2\tau_1 1.\end{aligned} \quad (4.76)$$

The 2×2 matrices ρ_i, τ_i, and σ_i, appearing in these equations are Pauli matrices operating in Nambu, valley, and layer spaces, respectively.

Integrating out the fermions from the action (4.73) yields the following effective action for the superconducting fields:

$$S_\Delta = \frac{1}{4\tilde{g}_{E_g}} \int d\tau \int d^2x \left(|\Delta_1|^2 + |\Delta_2|^2\right) + \frac{1}{2}\mathrm{Tr}\left(\hat{\mathcal{G}}_0\hat{\Delta}\right)^2 + \frac{1}{4}\mathrm{Tr}\left(\hat{\mathcal{G}}_0\hat{\Delta}\right)^4, \quad (4.77)$$

where higher-order terms have been ignored. The traces in (4.77) are over matrix indices, as well as frequency and momentum. The traces are most conveniently performed by letting

$$\hat{\mathcal{G}}^{-1}_0(i\omega_n, k) = \begin{pmatrix} \hat{G}^{-1}_+(i\omega_n, k) & 0 \\ 0 & \hat{G}^{-1}_-(i\omega_n, k) \end{pmatrix} \quad (4.78)$$

and

$$\hat{\Delta} = \begin{pmatrix} 0 & \hat{\Delta}_0 + \hat{\Delta}_1 - i\hat{\Delta}_2 \\ \hat{\Delta}_0^\dagger + \hat{\Delta}_1^\dagger + i\hat{\Delta}_2^\dagger & 0 \end{pmatrix} \tag{4.79}$$

The 4×4 matrices $\hat{G}_\pm$ can then be expressed as

$$\hat{G}_\pm^{-1} = \begin{pmatrix} \hat{g}_{\pm,+}^{-1}(i\omega_n, k) & 0 \\ 0 & \hat{g}_{\pm,-}^{-1}(i\omega_n, k) \end{pmatrix}, \tag{4.80}$$

and the 2×2 Green function matrices can be inverted to give

$$\hat{g}_{rt}(i\omega_n, \mathbf{k}) = \frac{(i\omega_n + r\mu)1 + (r\varepsilon_{\mathbf{k}} \cos 2\theta_{\mathbf{k}} + tv_3 k \cos\theta_{\mathbf{k}})\sigma_1 + (t\varepsilon_{\mathbf{k}} \sin 2\theta_{\mathbf{k}} - rv_3 k \sin\theta_{\mathbf{k}})\sigma_2}{-(i\omega_n + r\mu)^2 + \varepsilon_{\mathbf{k}}^2 + (v_3 k)^2 + 2rtv_3 k\varepsilon_{\mathbf{k}} \cos 3\theta_{\mathbf{k}}} \tag{4.81}$$

Similarly, the 4×4 matrices $\hat{\Delta}_i$ in (4.79) can be expressed as

$$\hat{\Delta}_0 = \begin{pmatrix} 0 & \hat{\delta}_0 \\ \hat{\delta}_0 & 0 \end{pmatrix}, \quad \hat{\Delta}_1 = \begin{pmatrix} 0 & \hat{\delta}_1 \\ \hat{\delta}_1 & 0 \end{pmatrix}, \quad \hat{\Delta}_2 = \begin{pmatrix} 0 & -i\hat{\delta}_2 \\ i\hat{\delta}_2 & 0 \end{pmatrix}, \tag{4.82}$$

where $\hat{\delta}_0 = \Delta_0 1$, $\hat{\delta}_1 = \Delta_1 \sigma_1$, and $\hat{\delta}_2 = \Delta_2 \sigma_2$. In terms of these new matrices, the quadratic part of the action (4.77) becomes

$$\begin{aligned} S_\Delta^{(2)} = \int d\tau \int d^2x \left[\frac{1}{4\tilde{g}_{A_{1g}}} |\Delta_0|^2 + \frac{1}{4\tilde{g}_{E_g}} \left(|\Delta_1|^2 + |\Delta_2|^2 \right) \right] \\ + \mathrm{Tr} \left[\hat{G}_+ (\hat{\Delta}_1 + \hat{\Delta}_1 - i\hat{\Delta}_2) \hat{G}_- (\hat{\Delta}_1 + \hat{\Delta}_1 - i\hat{\Delta}_2)^\dagger \right]. \end{aligned} \tag{4.83}$$

The trace in this expression can be evaluated using standard methods. Assuming that the E_g coupling is the most negative, as found in our RG solutions, one finds a sign-changing term $\sim (T - T_c)(|\Delta_1|^2 + |\Delta_2|^2)$, so that there is a mean-field transition into the d-wave superconducting phase below temperature T_c, which is determined by the following condition:

$$\frac{1}{4\tilde{g}_{E_g}} = -\int \frac{d^2k}{(2\pi)^2} \left[\frac{1}{\xi_{\mathbf{k}} + \mu} \tanh\left(\frac{\xi_{\mathbf{k}} + \mu}{2T_c} \right) + \frac{1}{\xi_{\mathbf{k}} - \mu} \tanh\left(\frac{\xi_{\mathbf{k}} - \mu}{2T_c} \right) \right]. \tag{4.84}$$

The nature of the superconducting phase is determined by the fourth-order term in (4.77). Considering first just the d-wave terms, we have

$$\begin{aligned} S_{\Delta_{1,2}}^{(4)} =& \mathrm{Tr}\left[\hat{G}_+(\hat{\Delta}_1 + i\hat{\Delta}_2)\hat{G}_-(\hat{\Delta}_1 + i\hat{\Delta}_2)^\dagger\right]^2 \\ =& \int d^2x \int d\tau \left[\frac{\beta}{2}\left(|\Delta_1(\tau,x)|^2 + |\Delta_2(\tau,x)|^2\right)^2 + \gamma|\Delta_1^2(\tau,x) + \Delta_2^2(\tau,x)|^2\right]. \end{aligned} \tag{4.85}$$

Equation (4.85) is in fact the most general possible form of a quartic contribution to the free energy that is invariant under the symmetry of the honeycomb lattice [121]. The first coefficient β is positive, as required for the phase to be thermodynamically stable, and its precise value shall not be of concern here. The second coefficient in (4.85) is given by

$$\begin{aligned} \gamma =& \sum_n \int \frac{d^2k}{(2\pi)^2} \frac{1}{[(i\omega_n+\mu)^2 - \xi_{\mathbf{k}}^2]^2[(i\omega_n-\mu)^2 - \xi_{\mathbf{k}}^2]^2} \\ &\times \left\{\xi_{\mathbf{k}}^4 + 2\xi_{\mathbf{k}}^2(\mu^2 - \omega_n^2) - (\mu^2+\omega_n^2)^2 - 2\left[\varepsilon_{\mathbf{k}}^2\cos 4\theta_{\mathbf{k}} + (v_3 k)^2\cos 2\theta_{\mathbf{k}} - 2v_3 k\varepsilon_{\mathbf{k}}\cos 3\theta_{\mathbf{k}}\right]^2\right\}, \end{aligned} \tag{4.86}$$

where the external momenta have been set to zero when performing traces over the Green's functions. For $T < T_c$, the nature of the superconducting phase depends on the sign of γ. Below we consider the two possible cases in turn.

For $\gamma < 0$, the free energy is minimized by maximizing the amplitude of the last term in (4.85). This clearly occurs when there is no relative phase difference between Δ_1 and Δ_2. In this case, assuming $\Delta_i(\tau,x) = const.$, the free energy density f is given by

$$\frac{f}{T} = \alpha\left(|\Delta_1|^2 + |\Delta_2|^2\right) + \left(\frac{\beta}{2} + \gamma\right)\left(|\Delta_1|^2 + |\Delta_2|^2\right)^2. \tag{4.87}$$

Clearly the phase is only stable when $\beta/2 + \gamma > 0$. Assuming this is the case, the free energy is minimized for $\Delta_1 = \Delta_0\cos\theta$ and $\Delta_2 = \Delta_0\sin\theta$, where $\Delta_0 = \sqrt{-\alpha/(\beta+2\gamma)}$, and θ can take any value. Because there is no phase difference between the two order parameter components, this phase is non-chiral and preserves time-reversal symmetry.

For $\gamma > 0$, on the other hand, the last term in (4.85) is positive definite, so it is clearly minimized when $\Delta_2 = e^{\pm i\pi/2}\Delta_1$. In this case, again assuming $\Delta_i(\tau, x) = const.$, the Ginzburg–Landau free energy density f is given by

$$\frac{f}{T} = \alpha\left(|\Delta_1|^2 + |\Delta_2|^2\right) + \frac{\beta}{2}\left(|\Delta_1|^2 + |\Delta_2|^2\right)^2, \tag{4.88}$$

which is minimized by $|\Delta_{1,2}| = \sqrt{-\alpha/\beta}$. Because the two order parameter components coexist with a nontrivial relative phase between them, time-reversal symmetry is broken in this case. This is the chiral, time-reversal symmetry breaking $d + id$ phase.

Having identified these two possibilities, the next step is to determine the sign of γ from Equation (4.86). The equation takes on a slightly more tractable form in the limit $v_3 \to 0$:

$$\gamma \overset{(v_3=0)}{=} \sum_n \int \frac{d^2k}{(2\pi)^2} \frac{2\varepsilon_{\mathbf{k}}^2(\mu^2 - \omega_n^2) - (\mu^2 + \omega_n^2)^2}{[(i\omega_n + \mu)^2 - \varepsilon_{\mathbf{k}}^2]^2[(i\omega_n - \mu)^2 - \varepsilon_{\mathbf{k}}^2]^2}. \tag{4.89}$$

In the weak-coupling limit, this integral should be dominated by the infrared singularity at $\varepsilon_{\mathbf{k}} \sim \mu$, $i\omega_n \sim T_c \ll \mu$ (recall that the Ginzburg-Landau expansion we are performing is valid only for $T \sim T_c$). Performing the summation over Matsubara frequencies and the integral over momentum (the latter of which must be done numerically), we find that this is indeed the case, with $\gamma > 0$ for $\mu \gg T_c$, so that the chiral superconducting phase is favored in the weakly-coupled regime. On the other hand, for $\mu \lesssim T_c$, we find $\gamma < 0$, so that the non-chiral phase is preferred. In general, there is a critical line $\mu \approx 2.8T_c$ separating the two cases when $v_3 = 0$. As v_3 is increased, even smaller values of μ are needed in order for the chiral phase to be preferred over the non-chiral phase.

Let us now consider the effects of including the s-wave order parameter in the effective action (4.77). In addition to the obvious terms containing even powers of Δ_0,

there is also an allowed term that is *linear* in Δ_0, and this turns out to have important consequences for the nature of the superconducting phase. The part of the quartic term in (4.77) that is linear in Δ_0 is given by

$$\begin{aligned}\frac{1}{4}\mathrm{Tr}\left(\hat{\mathcal{G}}_0\hat{\Delta}\right) \ni &\mathrm{Tr}\Big[\hat{g}_{++}(\hat{\delta}_1-\hat{\delta}_2)\hat{g}_{--}(\hat{\delta}_1^\dagger-\hat{\delta}_2^\dagger)\hat{g}_{++}(\hat{\delta}_1-\hat{\delta}_2)\hat{g}_{--}\hat{\delta}_0^\dagger \\ &+\hat{g}_{+-}(\hat{\delta}_1+\hat{\delta}_2)\hat{g}_{-+}(\hat{\delta}_1^\dagger+\hat{\delta}_2^\dagger)\hat{g}_{+-}(\hat{\delta}_1+\hat{\delta}_2)\hat{g}_{-+}\hat{\delta}_0^\dagger\Big]+c.c. \\ =&16\mu\Delta_0^*\mathrm{Tr}\left\{\frac{\Sigma_1(\Sigma_1^2-\Sigma_2^2)|\Delta_1|^2\Delta_1+\Sigma_1(3\Sigma_2^2-\Sigma_1^2)|\Delta_2|^2\Delta_1+2\Sigma_1\Sigma_2^2\Delta_1^*\Delta_2^2}{((i\omega_n+\mu)^2-\xi_{\mathbf{k}}^2)^2((i\omega_n-\mu)^2-\xi_{\mathbf{k}}^2)^2}\right\} \\ &+c.c.,\end{aligned} \tag{4.90}$$

where we have defined

$$\begin{aligned}\Sigma_1(\mathbf{k}) &= \varepsilon_{\mathbf{k}}\cos 2\theta_{\mathbf{k}}+v_3k\cos\theta_{\mathbf{k}} \\ \Sigma_2(\mathbf{k}) &= \varepsilon_{\mathbf{k}}\sin 2\theta_{\mathbf{k}}-v_3k\sin\theta_{\mathbf{k}}\end{aligned} \tag{4.91}$$

From (4.90) we obtain the following term in the free energy:

$$F_\delta = \delta\left[\Delta_0^*(|\Delta_1|^2\Delta_1-2|\Delta_2|^2\Delta_1-\Delta_1^*\Delta_2^2)+c.c.\right], \tag{4.92}$$

where

$$\delta = 8\mu T\sum_n\int\frac{d^2k}{(2\pi)^2}\frac{\varepsilon_{\mathbf{k}}^2\cos 6\theta_{\mathbf{k}}+v_3k(3\varepsilon_{\mathbf{k}}^2+v_3^2k^2)\cos 3\theta_{\mathbf{k}}+3\varepsilon_{\mathbf{k}}v_3^2k^2}{((i\omega_n+\mu)^2-\xi_{\mathbf{k}}^2)^2((i\omega_n-\mu)^2-\xi_{\mathbf{k}}^2)^2}. \tag{4.93}$$

From the term (4.92) in the free energy it would appear that s-wave superconducting order is immediately induced once $\Delta_{1,2}\neq 0$. However, due to the phase difference of $\pm\pi/2$ between Δ_1 and Δ_2, $F_\delta = 0$ in the chiral phase, so that s-wave order is not immediately induced as long as this phase difference persists. By minimizing the free energy with respect to Δ_0, one finds that $\Delta_2 = e^{\pm i\pi/2}\Delta_1$ and hence $\Delta_0 = 0$ as long as $\gamma > \delta^2|\Delta_1|^2/\alpha_s$, which is always the case sufficiently close to T_c. (Here it is assumed that $\gamma > 0$, and $\alpha_s > 0$ is the coefficient of

the term $\sim |\Delta_0|^2$ in the free energy.) Of course, it is possible that s-wave superconductivity is induced at temperatures well below T_c, but showing this would require that one include higher-order terms in the free energy expansion.

The quasiparticle spectrum in the superconducting phase can be obtained by diagonalizing the full fermionic Green function (4.74). Considering first the limit $\nu_3 = 0$, the eigenvalues when only one order parameter is present are given by

$$E_{\Delta_1}(k) = \pm \left[\varepsilon_k^2 + \mu^2 + \Delta_1^2 \pm 2\sqrt{\varepsilon_k^2 \mu^2 + \left(\frac{k_x k_y}{m^*}\right)^2 \Delta_1^2} \right]^{1/2}, \tag{4.94}$$

and

$$E_{\Delta_2}(k) = \pm \left[\varepsilon_k^2 + \mu^2 + \Delta_2^2 \pm 2\sqrt{\varepsilon_k^2 \mu^2 + \left(\frac{k_x^2 - k_y^2}{2m^*}\right)^2 \Delta_2^2} \right]^{1/2}, \tag{4.95}$$

where each eigenvalue is twofold degenerate (the $\pm$ signs can be chosen independently in these equations). It's easy to see from these equations that E_{Δ_1} generically has point nodes along the lines $k_x = \pm k_y$, while E_{Δ_2} has nodes along the $k_x = 0$ and $k_y = 0$ directions. These cases are shown in panels (a) and (b) of Figure 4.10, respectively. These nodes remain intact if the two orders have the same phase and coexist in any linear combination, with the position of the nodes rotating in the k_x–k_y plane as the relative magnitude of the two components is varied (Figure 4.10(c)). Recall from the above analysis of the free energy that any of these non-chiral phases are allowed for the case where $\gamma < 0$. For the case $\gamma > 0$, on the other hand, we have $\Delta_2 = e^{\pm i\pi/2}\Delta_1$. In this case, the dispersion is isotropic and fully gapped, as shown in Figure 4.10(d). (In the special case $\mu = 0$, the chiral phase has a single nodal point at $k_x = k_y = 0$. However, we know from our RG analysis that d-wave superconductivity can arise only for finite μ.)

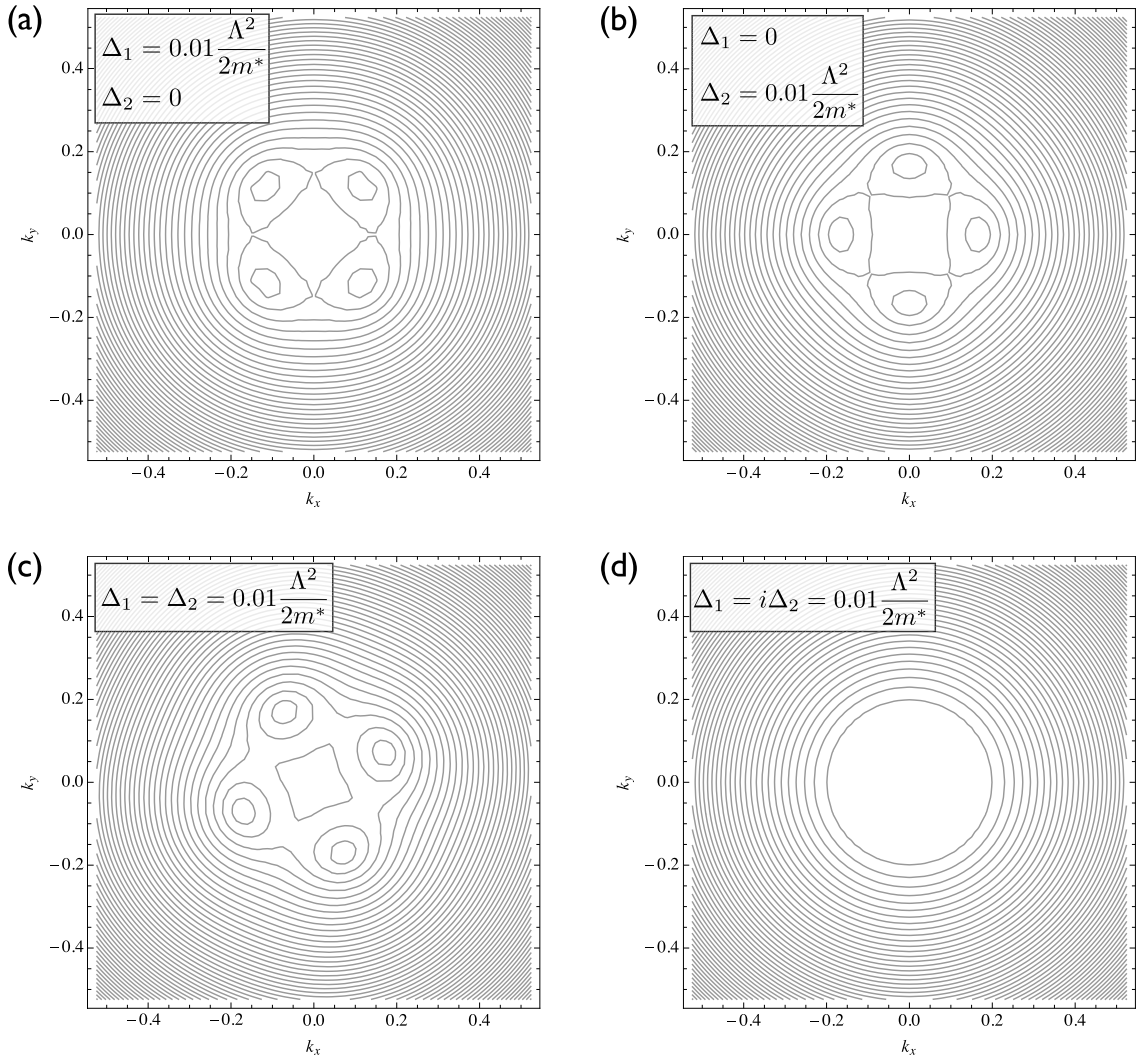

Figure 4.10: Quasiparticle excitation energy in the presence of superconducting order in the absence of trigonal warping, with $\mu = 0.01\Lambda^2/2m^*$. The non-chiral phases shown in (a)–(c) are all degenerate, have no relative phase between the two order parameter components, and have four nodal points in the excitation spectrum. The chiral phase shown in (d) has a nontrivial phase difference between the order parameter components, and is isotropic and fully gapped. (In all subplots, the contours are spaced by energy $0.005\Lambda^2/2m^*$.)

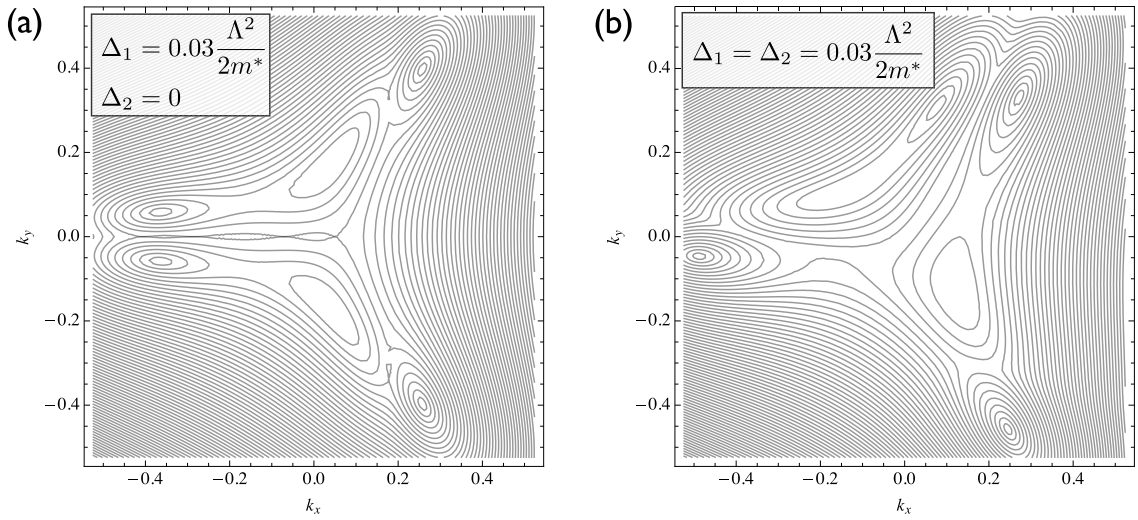

Figure 4.11: Quasiparticle excitation energy near **K** in the presence of non-chiral superconducting order, trigonal warping $v_3 = 0.178\Lambda/2m^*$, and chemical potential $\mu = 0.01\Lambda^2/2m^*$. The excitations are gapless at 4 nodal points (the contours are spaced by energy $0.005\Lambda^2/2m^*$).

We now turn to the case with nonzero trigonal warping. Considering first the non-chiral phase, shown in Figure 4.11, we find that the nodes in the excitation spectrum are not gapped due to the superconducting order, but merely shifted to different positions in momentum space. This is true for both Δ_1 and Δ_2 superconducting orders, as well as linear combinations of the two. For the chiral phase, on the other hand, we see that the nodes become completely gapped due to the superconducting order, as shown in Figure 4.12.

4.8.2 Pair density wave superconducting phase

For small values of v_3, it was found in Section 4.5 that the pair density wave (PDW) superconducting phase, which belongs to the $A_{1\mathbf{K}}$ representation, is the preferred solution. As in the d-wave case, the representation is two-dimensional, and the RG procedure does

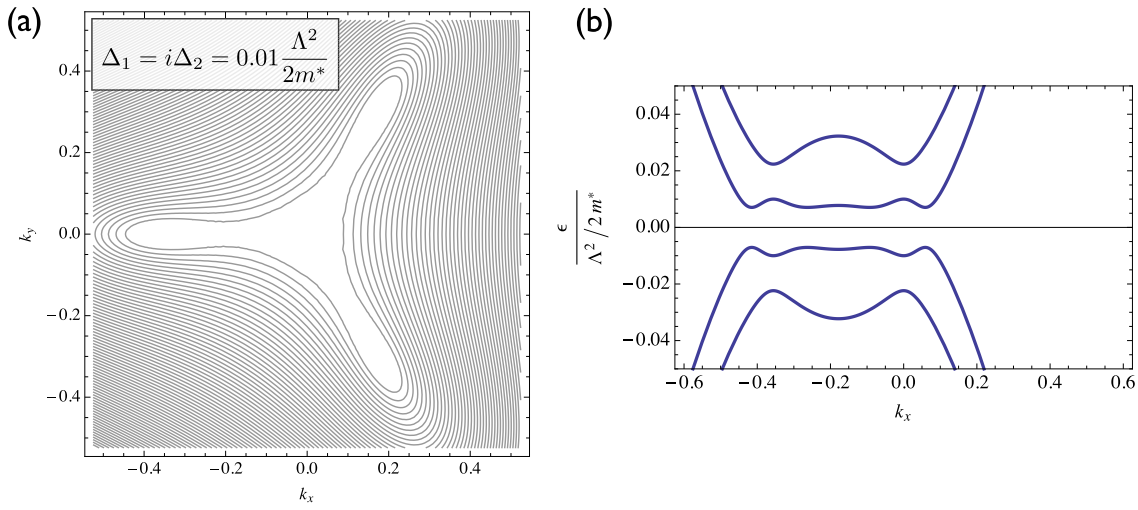

Figure 4.12: (a) Contour plot of the quasiparticle excitation energy near $\mathbf{K}$ in the presence of chiral superconducting order, trigonal warping $v_3 = 0.178\Lambda/2m^*$, and chemical potential $\mu = 0.01\Lambda^2/2m^*$. The excitations are gapped at all momenta (the contours are spaced by energy $0.005\Lambda^2/2m^*$). (b) The corresponding quasiparticle energy bands are shown along the line $k_y = 0$. (The corresponding dispersion near $-\mathbf{K}$ is obtained by reflecting $k_x \to -k_x$.)

not determine which linear combination of the two order parameter components is selected. In order to determine this, we again derive an effective Ginzburg-Landau theory as in the previous section, but now with the order parameter

$$\hat{\Delta} = \mathrm{Re}\Delta_{\mathbf{K}1}\rho_1 1\sigma_1 - \mathrm{Im}\Delta_{\mathbf{K}1}\rho_2 1\sigma_1 + \mathrm{Im}\Delta_{\mathbf{K}2}\rho_1\tau_3\sigma_1 + \mathrm{Re}\Delta_{\mathbf{K}2}\rho_2\tau_3\sigma_1. \tag{4.96}$$

The Pauli matrices ρ, τ, σ correspond to Nambu, valley, and layer spaces, and the order parameters are shorthand for $(\Delta_{\mathbf{K}1}, \Delta_{\mathbf{K}2}) \equiv (\Delta^{(1)}_{A1\mathbf{K}}, \Delta^{(1)}_{A1\mathbf{K}})$, with each component being complex.[5]

As in the previous section, the nature of the PDW phase is determined by the

[5] As in the d-wave case, a factor of i has been included in the definition of $\Delta_{\mathbf{K}2}$, such that the combination preserving time-reversal symmetry corresponds to $\Delta_{\mathbf{K}1}$ and $\Delta_{\mathbf{K}2}$ having the same phase.

fourth-order term in the Ginzburg-Landau expansion for the effective action:

$$\begin{aligned} S^{(4)} &= \frac{1}{4}\mathrm{Tr}\left(\hat{\mathcal{G}}_0\hat{\Delta}\right)^4 \\ &= \frac{1}{2}[|\Delta_{\mathbf{K}1}|^2 + |\Delta_{\mathbf{K}2}|^2 + i(\Delta_{\mathbf{K}1}\Delta^*_{\mathbf{K}2} - \Delta_{\mathbf{K}2}\Delta^*_{\mathbf{K}1})]\mathrm{Tr}\left[(\hat{\mathrm{g}}_{++}\sigma_1\hat{\mathrm{g}}_{-+}\sigma_1)^2\right] \\ &\quad + \frac{1}{2}[|\Delta_{\mathbf{K}1}|^2 + |\Delta_{\mathbf{K}2}|^2 - i(\Delta_{\mathbf{K}1}\Delta^*_{\mathbf{K}2} - \Delta_{\mathbf{K}2}\Delta^*_{\mathbf{K}1})]\mathrm{Tr}\left[(\hat{\mathrm{g}}_{+-}\sigma_1\hat{\mathrm{g}}_{--}\sigma_1)^2\right] \\ &= \left[2(|\Delta_{\mathbf{K}1}|^2 + |\Delta_{\mathbf{K}2}|^2)^2 - |\Delta^2_{\mathbf{K}1} + \Delta^2_{\mathbf{K}2}|^2\right]\mathrm{Tr}\left[(\hat{\mathrm{g}}_{++}\sigma_1\hat{\mathrm{g}}_{-+}\sigma_1)^2\right], \end{aligned} \tag{4.97}$$

where in the last line I used the fact that $\hat{g}_{r,t} \to \hat{g}_{r,-t}$ under $\theta_{\mathbf{k}} \to \theta_{\mathbf{k}} + \pi$. As usual, I also assumed that $\Delta_{1,2}$ have no frequency or momentum dependence. Evaluating the trace and simplifying gives the following 4th order term for the free energy:

$$F^{(4)} = \frac{\beta}{2}(|\Delta_{\mathbf{K}1}|^2 + |\Delta_{\mathbf{K}2}|^2)^2 + \gamma|\Delta^2_{\mathbf{K}1} + \Delta^2_{\mathbf{K}2}|^2, \tag{4.98}$$

with

$$\begin{aligned} \beta = 8T\sum_n \int \frac{d^2k}{(2\pi)^2} &\frac{1}{[(i\omega_n+\mu)^2 + (\xi^+_{\mathbf{k}})^2]^2[(i\omega_n-\mu)^2 + (\xi^-_{\mathbf{k}})^2]^2} \\ \times \left\{[(i\omega_n)^2 - \mu^2]^2 - 16(\varepsilon_{\mathbf{k}}v_3k\sin 3\theta_{\mathbf{k}})^2 + 2\mu^2[3\varepsilon^2_{\mathbf{k}} - (v_3k)^2] + 2(i\omega_n)^2[3(v_3k)^2 - \varepsilon^2_{\mathbf{k}}]\right\}, \end{aligned} \tag{4.99}$$

and $\gamma = -\beta/4$. Here I have used

$$\xi^{\pm}_{\mathbf{k}} = \sqrt{\varepsilon^2_{\mathbf{k}} + v_3^2k^2 \pm 2v_3k\varepsilon_{\mathbf{k}}\cos 3\theta_{\mathbf{k}}}. \tag{4.100}$$

Using the same arguments as in the d-wave case, the fact that $\gamma < 0$ means that the non-chiral PDW phase is stable. In this phase, the order parameter amplitude varies spatially as either $\Delta_{\mathbf{K}1} \sim \cos(2\mathbf{K}\cdot\mathbf{x})$ or $\Delta_{\mathbf{K}2} \sim \sin(2\mathbf{K}\cdot\mathbf{x})$, or some linear combination of the two, with only the overall amplitude $|\Delta_{\mathbf{K}1}|^2 + |\Delta_{\mathbf{K}2}|^2$ fixed.

The quasiparticle excitation spectrum in the non-chiral PDW phase is shown in Figure 4.13. The spectrum does not depend on the individual amplitudes of $\Delta_{\mathbf{K}1}$ and

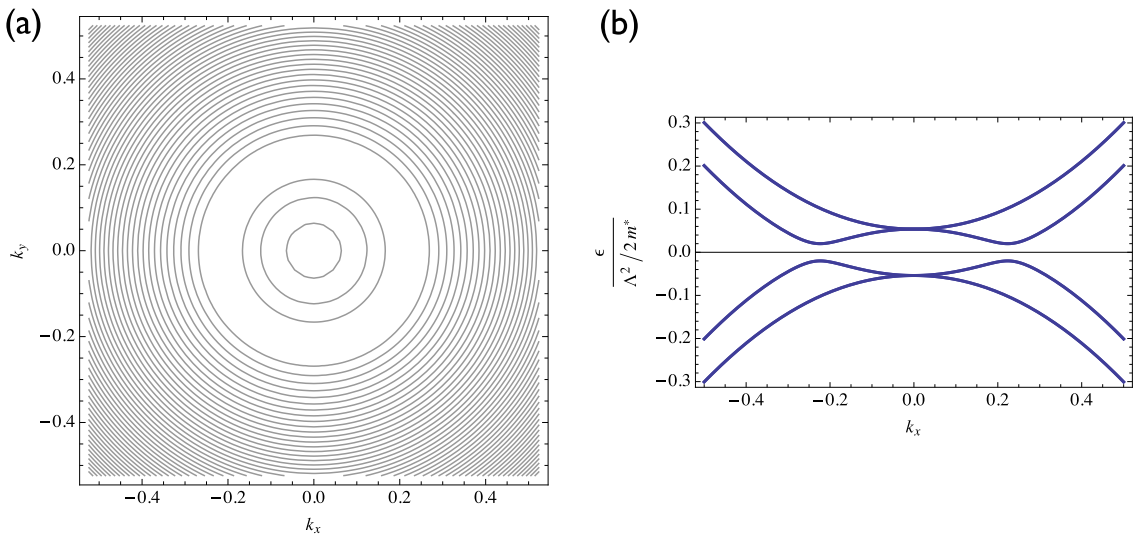

Figure 4.13: (a) Contour plot of the lowest-energy quasiparticle excitation band near $\pm\mathbf{K}$ in the presence of PDW superconducting order $\sqrt{|\Delta_{\mathbf{K}1}|^2 + |\Delta_{\mathbf{K}2}|^2} = 0.01\Lambda^2/2m^*$, chemical potential $\mu = 0.05\Lambda^2/2m^*$, and without trigonal warping ($v_3 = 0$). The excitations are gapped at all momenta. (b) The corresponding quasiparticle energy bands are shown along the line $k_y = 0$.

$\Delta_{\mathbf{K}2}$, but only on the overall magnitude $\sqrt{|\Delta_{\mathbf{K}1}|^2 + |\Delta_{\mathbf{K}2}|^2}$. Despite the fact that the order parameter vanishes and changes sign periodically in real space, excitations are fully gapped in this phase. In the absence of trigonal warping, the spectrum is completely isotropic around each point $\pm\mathbf{K}$.

4.9 Discussion

The most important aspect of the work presented in this chapter is the unbiased way in which the RG approach is able to address particle-hole and superconducting orders on equal footing. We have found that generically, i.e. for any initial choice of repulsive interactions, there is a crossover between the two regimes described above, with particle-hole order giving way to an unconventional superconducting phase as the chemical potential is

increased. From this analysis we see that such crossover behavior, which is ubiquitous in quantum many-body systems, can be usefully described as a competition between temperature and chemical potential to be the most relevant parameter (in the RG sense), with the winner of this competition ultimately determining which type of phase is realized. While this perturbative RG scheme can only be formally justified in the weak-coupling limit, the similarity of the phase diagram shown in Figure 4.9 to those of the more strongly coupled systems shown in Figure 4.1 is suggestive that similar mechanisms may be at play in these systems.

In Section 4.4.2 it was shown that, for sufficiently large μ/T, the coupling corresponding to only a single superconducting channel grows under RG flow, with no competing instabilities in other superconducting or particle-hole channels. These observations lend justification to RG approaches that consider only particle-particle contributions to the flow equations, arguing that—at least for $\mu \gg T$ and away from special fine-tuned nesting conditions—superconductivity is the only generic instability of fermionic systems at finite density [122]. However, as shown in the phase diagrams calculated in Sections 4.5 and 4.7, the highest values of superconducting T_c occur near the region of the phase diagram exhibiting particle-hole instability. Here fluctuations in particle-hole channels clearly play a role in enhancing T_c, and the approach of considering only contributions from particle-particle diagrams, which ignores these fluctuations, breaks down.

Experimental observation of the unconventional superconducting phase in doped bilayer graphene may be possible, but would be challenging due to the low predicted value of the transition temperature. If recent reports [96, 97] of a gap at the neutrality point

below $T \sim 5$K indeed correspond to an interaction-induced symmetry-breaking phase such as the particle-hole phases described here, then our model would predict that the doped sample should become superconducting below $T_c \lesssim 1$K. This value could be further reduced, however, due to the fact that disorder tends to suppress the T_c of unconventional superconducting states, in which the order parameter changes sign upon going around the Fermi surface. This includes states such as the d- and f-wave phases found in our theory.

Appendix A

Renormalization group flow equation coefficients

Below we list the flow equation coefficients used in the renormalization group analysis of the bilayer honeycomb lattice from Chapter 4, which were originally derived in Ref. [105].

The coefficients from (4.24) that come from evaluating the first diagram shown in Figure 4.4 are

$$\begin{aligned} A_{iii}^{(1/2)}(1) &= -\tfrac{1}{2}\{8 \pm \mathrm{Tr}[(\Gamma_i^{(1)}\tau_3 1_4)^2]\}\frac{m^*}{4\pi}, \\ A_{iii}^{(3/4)}(1) &= \tfrac{1}{4}\{\mathrm{Tr}[(\Gamma_i^{(1)}1\sigma_1 1)^2] \mp \mathrm{Tr}[(\Gamma_i^{(1)}\tau_3\sigma_1 1)^2] \\ &\qquad \mp \mathrm{Tr}[(\Gamma_i^{(1)}1\sigma_2 1)^2] + \mathrm{Tr}[(\Gamma_i^{(1)}\tau_3\sigma_2 1)^2]\}\frac{m^*}{4\pi}, \end{aligned} \tag{A.1}$$

where $\Gamma_i^{(m)}$ are the 8×8 matrices given in Table 4.1. In deriving these coefficients, the completeness relation $\mathrm{Tr}(\Gamma_i^{(m)}\Gamma_j^{(n)}) = 8\delta_{ij}\delta_{mn}$ has been used. The superscripts on the left hand sides of the above equations correspond to the upper and lower signs on the right

hand sides. As one would expect for the "RPA"-type diagram shown in Figure 4.4, only terms diagonal in the couplings are nonzero, with $A^{(a)}_{ijk}(1) \sim \delta_{ij}\delta_{jk}$. From the second and third diagrams in Figure 4.4, the nonzero contributions to the $A^{(a)}_{ijk}$ coefficients are

$$\begin{aligned}
A^{(1/2)}_{iij}(2+3) &= \tfrac{1}{8}\sum_{m=1}^{m_j}\{\mathrm{Tr}[(\Gamma^{(1)}_i\Gamma^{(m)}_j)^2] \pm \mathrm{Tr}(\Gamma^{(1)}_i\Gamma^{(m)}_j\tau_3 1_4\Gamma^{(1)}_i\tau_3 1_4\Gamma^{(m)}_j)\}\frac{m^*}{4\pi}, \\
A^{(3/4)}_{iij}(2+3) &= \tfrac{-1}{16}\sum_{m=1}^{m_j}[\mathrm{Tr}(\Gamma^{(1)}_i\Gamma^{(m)}_j 1\sigma_1 1\Gamma^{(1)}_i 1\sigma_1 1\Gamma^{(m)}_j) \mp \mathrm{Tr}(\Gamma^{(1)}_i\Gamma^{(m)}_j\tau_3\sigma_1 1\Gamma^{(1)}_i\tau_3\sigma_1 1\Gamma^{(m)}_j) \\
&\quad \mp \mathrm{Tr}(\Gamma^{(1)}_i\Gamma^{(m)}_j 1\sigma_2 1\Gamma^{(1)}_i 1\sigma_2 1\Gamma^{(m)}_j) + \mathrm{Tr}(\Gamma^{(1)}_i\Gamma^{(m)}_j\tau_3\sigma_2 1\Gamma^{(1)}_i\tau_3\sigma_2 1\Gamma^{(m)}_j)]\frac{m^*}{4\pi}.
\end{aligned} \tag{A.2}$$

From the fourth diagram in Figure 4.4,

$$\begin{aligned}
A^{(1/2)}_{kij}(4) &= \tfrac{1}{128}\sum_{m=1}^{m_i}\sum_{n=1}^{m_j}[\mathrm{Tr}(\Gamma^{(1)}_k\Gamma^{(m)}_i\Gamma^{(n)}_j)\mathrm{Tr}(\Gamma^{(1)}_k\Gamma^{(n)}_j\Gamma^{(m)}_i) \\
&\qquad \pm \mathrm{Tr}(\Gamma^{(1)}_k\Gamma^{(m)}_i\tau_3 1_4\Gamma^{(n)}_j)\mathrm{Tr}(\Gamma^{(1)}_k\Gamma^{(n)}_j\tau_3 1_4\Gamma^{(m)}_i)]\frac{m^*}{4\pi}, \\
A^{(3/4)}_{kij}(4) &= \tfrac{-1}{256}\sum_{m=1}^{m_i}\sum_{n=1}^{m_j}[\mathrm{Tr}(\Gamma^{(1)}_k\Gamma^{(m)}_i 1\sigma_1 1\Gamma^{(n)}_j)\mathrm{Tr}(\Gamma^{(1)}_k\Gamma^{(n)}_j 1\sigma_1 1\Gamma^{(m)}_i) \\
&\qquad \mp \mathrm{Tr}(\Gamma^{(1)}_k\Gamma^{(m)}_i\tau_3\sigma_1 1\Gamma^{(n)}_j)\mathrm{Tr}(\Gamma^{(1)}_k\Gamma^{(n)}_j\tau_3\sigma_1 1\Gamma^{(m)}_i) \\
&\qquad \mp \mathrm{Tr}(\Gamma^{(1)}_k\Gamma^{(m)}_i 1\sigma_2 1\Gamma^{(n)}_j)\mathrm{Tr}(\Gamma^{(1)}_k\Gamma^{(n)}_j 1\sigma_2 1\Gamma^{(m)}_i) \\
&\qquad + \mathrm{Tr}(\Gamma^{(1)}_k\Gamma^{(m)}_i\tau_3\sigma_2 1\Gamma^{(n)}_j)\mathrm{Tr}(\Gamma^{(1)}_k\Gamma^{(n)}_j\tau_3\sigma_2 1\Gamma^{(m)}_i)]\frac{m^*}{4\pi}.
\end{aligned} \tag{A.3}$$

Finally, from the fifth (particle-particle) diagram,

$$\begin{aligned}
A^{(1/2)}_{kij}(5) &= -\tfrac{1}{128}\sum_{m=1}^{m_i}\sum_{n=1}^{m_j}\{[\mathrm{Tr}(\Gamma^{(1)}_k\Gamma^{(m)}_i\Gamma^{(n)}_j)]^2 \mp [\mathrm{Tr}(\Gamma^{(1)}_k\Gamma^{(m)}_i\tau_3 1_4\Gamma^{(n)}_j)]^2\}\frac{m^*}{4\pi}, \\
A^{(3/4)}_{kij}(5) &= -\tfrac{1}{256}\sum_{m=1}^{m_i}\sum_{n=1}^{m_j}\{[\mathrm{Tr}(\Gamma^{(1)}_k\Gamma^{(m)}_i 1\sigma_1 1\Gamma^{(n)}_j)]^2 \pm [\mathrm{Tr}(\Gamma^{(1)}_k\Gamma^{(m)}_i\tau_3\sigma_1 1\Gamma^{(n)}_j)]^2 \\
&\qquad \pm [\mathrm{Tr}(\Gamma^{(1)}_k\Gamma^{(m)}_i 1\sigma_2 1\Gamma^{(n)}_j)]^2 + [\mathrm{Tr}(\Gamma^{(1)}_k\Gamma^{(m)}_i\tau_3\sigma_2 1\Gamma^{(n)}_j)]^2\}\frac{m^*}{4\pi}
\end{aligned} \tag{A.4}$$

We now turn to the symmetry-breaking source terms, which appear in the vertex flow equations (4.48) and (4.49), and come from evaluating the diagrams in Figure 4.5. The

coefficients for the particle-hole vertices are, for the first diagram,

$$B_{ij}^{(1/2)}(1) = -\tfrac{1}{2}\sum_{n=1}^{m_j}[\mathrm{Tr}(O^{(i)}\Gamma_j^{(n)}) \pm \mathrm{Tr}(\tau_3 1_4 O^{(i)}\tau_3 1_4 \Gamma_j^{(n)})]\frac{m^*}{4\pi},, \tag{A.5}$$

and for the second diagram,

$$B_{ij}^{(1/2)}(2) = \tfrac{1}{16}\sum_{n=1}^{m_j}\{\mathrm{Tr}[(O^{(i)}\Gamma_j^{(n)})^2] \pm \mathrm{Tr}(O^{(i)}\Gamma_j^{(n)}\tau_3 1_4 O^{(i)}\tau_3 1_4 \Gamma_j^{(n)})\}\frac{m^*}{4\pi}. \tag{A.6}$$

Finally, the coefficients corresponding to the last (particle-particle) vertex diagram in Figure 4.5 are given by

$$C_{ij}^{(1/2)} = \tfrac{-1}{16}\sum_{n=1}^{m_j}\{\mathrm{Tr}[\tilde{O}^{(i)}\Gamma_j^{(n)}\tilde{O}^{(i)}(\Gamma_j^{(n)})^T] \mp \mathrm{Tr}[\tilde{O}^{(i)}\Gamma_j^{(n)}\tau_3 1_4 \tilde{O}^{(i)}\tau_3 1_4 (\Gamma_j^{(n)})^T]\}\frac{m^*}{4\pi}. \tag{A.7}$$

Bibliography

[1] R. B. Laughlin and D. Pines, *Proc. Nat. Acad. Sci.*, vol. 97, p. 28, 2000.

[2] P. W. Anderson, *Science*, vol. 177, p. 393, 1972.

[3] V. L. Ginzburg and L. D. Landau, *Zh. Eksp. Teor. Fiz.*, vol. 20, p. 1064, 1950.

[4] T. H. Hansson, V. Oganesyan, and S. L. Sondhi, *Ann. Phys.*, vol. 313, p. 497, 2004.

[5] T. Kennedy and C. King, *Phys. Rev. Lett.*, vol. 55, p. 776, 1985.

[6] L. P. Gor'kov, *JETP*, vol. 9, p. 1364, 1959.

[7] A. A. Abrikosov, *J. Phys. Chem. Solids*, vol. 2, p. 199, 1957.

[8] B. Rosenstein and D. Li, *Rev. Mod. Phys.*, vol. 82, p. 109, 2010.

[9] J. Bardeen, L. N. Cooper, and J. R. Schrieffer, *Phys. Rev.*, vol. 106, p. 162, 1957.

[10] ——, *Phys. Rev.*, vol. 108, p. 1175, 1957.

[11] E. C. G. Stueckelberg and A. Petermann, *Helv. Phys. Acta*, vol. 26, p. 499, 1953.

[12] M. Gell-Mann and F. E. Low, *Phys. Rev.*, vol. 95, p. 1300, 1954.

[13] K. G. Wilson and J. Kogut, *Phys. Rep.*, vol. 12, p. 75, 1974.

[14] K. G. Wilson, *Rev. Mod. Phys.*, vol. 47, p. 773, 1975.

[15] J. M. Murray and Z. Tešanović, *Phys. Rev. Lett.*, vol. 105, p. 037006, 2010.

[16] J. M. Murray, A. Del Maestro, and Z. Tešanović, *Phys. Rev. B*, vol. 85, p. 115117, 2012.

[17] J. R. Neilson, A. Llobet, A. V. Stier, L. Wu, J. Wen, J. Tao, Y. Zhu, Z. Tešanović, N. P. Armitage, and T. M. McQueen, *Phys. Rev. B*, vol. 86, p. 054512, 2012.

[18] J. M. Murray and Z. Tešanović, *Phys. Rev. B*, vol. 87, p. 081103(R), 2013.

[19] O. Vafek, J. M. Murray, and V. Cvetkovic, *arXiv:1309.3123*, 2013.

[20] J. M. Murray, V. Cvetkovic, and O. Vafek, *in preparation*, 2013.

[21] J. M. Murray and Z. Tešanović, *Phys. Rev. D*, vol. 83, p. 126011, 2011.

[22] Y. Kamihara, T. Watanabe, M. Hirano, and H. Hosono, *J. Am. Chem. Soc.*, vol. 130, p. 3296, 2008.

[23] P. C. W. Chu, A. Koshelev, W. Kwok, I. Mazin, U. Welp, and H.-H. Wen, *Physica C*, vol. 469, p. 313, 2009.

[24] G. Blatter, M. V. Feigel'man, V. B. Geshkenbein, A. I. Larkin, and V. M. Vinokur, *Rev. Mod. Phys.*, vol. 66, p. 1125, 1994.

[25] S. Raghu, X.-L. Qi, C.-X. Liu, D. J. Scalapino, and S.-C. Zhang, *Phys. Rev. B*, vol. 77, p. 220503, 2008.

[26] K. Kuroki, S. Onari, R. Arita, H. Usui, Y. Tanaka, H. Kontani, and H. Aoki, *Phys. Rev. Lett.*, vol. 101, p. 087004, 2008.

[27] V. Cvetkovic and Z. Tešanović, *Euro. Phys. Lett.*, vol. 85, p. 37002, 2009.

[28] A. V. Chubukov, D. V. Efremov, and I. Eremin, *Phys. Rev. B*, vol. 78, p. 134512, 2008.

[29] M. M. Parish, J. Hu, and B. A. Bernevig, *Phys. Rev. B*, vol. 78, p. 144512, 2008.

[30] S. Salem-Sugui, L. Ghivelder, A. D. Alvarenga, J. L. Pimentel, H. Luo, Z. Wang, and H.-H. Wen, *Phys. Rev. B*, vol. 80, p. 014518, 2009.

[31] C. Choi, S. H. Kim, K.-Y. Choi, M.-H. Jung, S.-I. Lee, X. F. Wang, X. H. Chen, and X. L. Wang, *Supercond. Sci. Tech.*, vol. 22, p. 105016, 2009.

[32] M. Rotter, M. Tegel, and D. Jorendt, *Phys. Rev. Lett.*, vol. 101, p. 107006, 2008.

[33] A. Georges, G. Kotliar, W. Krauth, and M. J. Rozenberg, *Rev. Mod. Phys.*, vol. 68, p. 13, 1996.

[34] Z. Tešanović, L. Xing, L. Bulaevskii, Q. Li, and M. Suenaga, *Phys. Rev. Lett.*, vol. 69, p. 3563, 1992.

[35] Z. Tešanović and A. Andreev, *Phys. Rev. B*, vol. 49, p. 4064, 1994.

[36] S. Ullah and A. Dorsey, *Phys. Rev. B*, vol. 44, p. 262, 1991.

[37] R. Ikeda, T. Ohmi, and T. Tsuneto, *J. Phys. Soc. Japan*, vol. 60, p. 1051, 1990.

[38] W. E. Lawrence and S. Doniach, in *Proc. 12th Int. Conf. Low Temp. Phys.*, 1970, p. 361.

[39] M. Kollar, M. Eckstein, K. Byczuk, N. Blmer, P. van Dongen, M. Radke de Cuba, W. Metzner, D. Tanasković, V. Dobrosavljević, G. Kotliar, and D. Vollhardt, *Ann. Phys. (Leipzig)*, vol. 14, p. 642, 2005.

[40] M. Tinkham, *Introduction to Superconductivity.* Dover, 1996.

[41] Y. Kato and N. Nagaosa, *Phys. Rev. B*, vol. 48, p. 7383, 1993.

[42] Z. Tešanović and L. Xing, *Phys. Rev. Lett.*, vol. 67, p. 2729, 1991.

[43] J. Hu and A. H. MacDonald, *Phys. Rev. Lett.*, vol. 71, p. 432, 1993.

[44] A. Yamamoto, J. Jaroszynski, C. Taratini, L. Balicas, J. Jiang, A. Gurevich, D. C. Larbalestier, R. Jin, A. S. Sefat, M. A. McGuire, B. C. Sales, D. K. Christen, and D. Mandrus, *App. Phys. Lett.*, vol. 94, p. 062511, 2009.

[45] Y. Wang, L. Li, and N. P. Ong, *Phys. Rev. B*, vol. 73, p. 024510, 2006.

[46] Z. Tešanović, *Physica (Amsterdam)*, vol. 220C, p. 303, 1994.

[47] H. K. Mak, P. Burger, L. Cevey, T. Wolf, C. Meingast, and R. Lortz, *Phys. Rev. B*, vol. 87, p. 214523, 2013.

[48] L. N. Bulaevskii, M. Ledvij, and V. G. Kogan, *Phys. Rev. Lett.*, vol. 68, p. 3773, 1992.

[49] A. E. Koshelev, *Phys. Rev. B*, vol. 50, p. 506, 1994.

[50] T. J. Williams, A. A. Aczel, E. Baggio-Saitovitch, S. L. Bud'ko, P. C. Canfield, J. P. Carlo, T. Goko, J. Munevar, N. Ni, Y. J. Uemura, W. Yu, and G. M. Luke, *Phys. Rev. B*, vol. 80, p. 094501, 2009.

[51] A. L. Fetter and P. C. Hohenberg, *Phys. Rev.*, vol. 159, p. 330, 1967.

[52] I. Pallecchi, C. Fanciulli, M. Tropeano, A. Palenzona, M. Ferretti, A. Malagoli, A. Martinelli, I. Sheikin, M. Putti, and C. Ferdeghini, *Phys. Rev. B*, vol. 79, p. 104515, 2009.

[53] A. Larkin and A. Varlamov, *Theory of Fluctuations in Superconductors.* Oxford University Press, 2005.

[54] S. Weyeneth, R. Puzniak, U. Mosele, N. Zhigadlo, S. Katrych, Z. Bukowski, J. Karpinski, S. Kohout, J. Roos, and H. Keller, *J. Supercond. Novel Magnetism*, vol. 22, p. 325, 2009.

[55] S. Margadonna, Y. Takabayashi, M. T. McDonald, M. Brunelli, G. Wu, R. H. Liu, X. H. Chen, and K. Prassides, *Phys. Rev. B*, vol. 79, p. 014503, 2009.

[56] D. Jérome and H. J. Schulz, *Adv. Phys.*, vol. 31, p. 299, 1982.

[57] C. R. Laumann, S. A. Parameswaran, and S. L. Sondhi, *Phys. Rev. B*, vol. 80, p. 144415, 2009.

[58] A. V. Chubukov, S. Sachdev, and J. Ye, *Phys. Rev. B*, vol. 49, p. 11919, 1994.

[59] S. Sachdev, *Quantum Phase Transitions.* Cambridge University Press, 2011.

[60] J. Zinn-Justin, *Quantum Field Theory and Critical Phenomena*. Claredon Press, Oxford, 2002.

[61] P. Coleman, in *Handbook of Magnetism and Advanced Magnetic Materials*, 2007, pp. 95–148.

[62] A. C. Hewson, *The Kondo Problem to Heavy Fermions*. Cambridge University Press, 1993.

[63] S. Doniach, *Physica B*, vol. 91, p. 231, 1977.

[64] C. Varma, *Rev. Mod. Phys.*, vol. 48, p. 219, 1976.

[65] K. Kummer, Y. Kucherenko, S. Danzenbächer, C. Krellner, C. Geibel, M. G. Holder, L. V. Bekenov, T. Muro, and Y. Kato, *Phys. Rev. B*, vol. 84, p. 245114, 2011.

[66] A. Fernandez-Pañella, V. Balédent, D. Braithwaite, L. Paolasini, R. Verbeni, G. Lapertot, and J.-P. Rueff, *Phys. Rev. B*, vol. 86, p. 125104, 2012.

[67] S. Watanabe and K. Miyake, *J. Phys. Cond. Mat.*, vol. 23, p. 094217, 2011.

[68] A. Taraphder and P. Coleman, *Phys. Rev. Lett.*, vol. 66, p. 2814, 1991.

[69] H. Matsuura and K. Miyake, *arXiv:1209.5519*, 2012.

[70] J. R. Neilson, T. M. McQueen, A. Llobet, J. Wen, and M. R. Suchomel, *Phys. Rev. B*, vol. 87, p. 045124, 2013.

[71] H. Lei, K. Wang, H. Ryu, D. Graf, J. B. Warren, and C. Petrovic, *arXiv:1211.1371*, 2012.

[72] N. Read and D. M. Newns, *J. Phys. C*, vol. 16, p. 3237, 1983.

[73] P. Coleman, *Phys. Rev. B*, vol. 29, p. 3035, 1984.

[74] D. M. Newns and N. Read, *Adv. Phys.*, vol. 36, p. 799, 1987.

[75] A. Auerbach, *Interacting Electrons and Quantum Magnetism*. Springer, 1998.

[76] C. Pepin, *Phys. Rev. Lett.*, vol. 98, p. 206401, 2007.

[77] J.-X. Zhu, I. Martin, and A. R. Bishop, *Phys. Rev. Lett.*, vol. 100, p. 236403, 2008.

[78] M.-T. Tran, A. Benlagra, C. Pepin, and K.-S. Kim, *Phys. Rev. B*, vol. 85, p. 165118, 2012.

[79] X.-G. Wen, *Quantum Field Theory of Many-Body Systems*. Oxford University Press, 2007.

[80] R. H. McKenzie, J. Merino, J. B. Marston, and O. P. Sushkov, *Phys. Rev. B*, vol. 64, p. 085109, 2001.

[81] P. Coleman and N. Andrei, *J. Phys. Cond. Mat.*, vol. 1, p. 4057, 1989.

[82] J. Merino and R. H. McKenzie, *Phys. Rev. Lett.*, vol. 87, p. 237002, 2001.

[83] C. Dallera, M. Grioni, A. Shukla, G. Vankó, J. L. Sarrao, J. P. Rueff, and D. L. Cox, *Phys. Rev. Lett.*, vol. 88, p. 196403, 2002.

[84] Z. Zou and P. W. Anderson, *Phys. Rev. Lett.*, vol. 57, p. 2073, 1986.

[85] S. M. M. Evans, *J. Phys. Cond. Mat.*, vol. 2, p. 9097, 1990.

[86] H. Kontani and K. Yamada, *J. Phys. Soc. Japan*, vol. 65, p. 172, 1996.

[87] T. Mutou and D. S. Hirashima, *J. Phys. Soc. Japan*, vol. 65, p. 369, 1996.

[88] R. M. White, *Quantum Theory of Magnetism.* Springer, 2006.

[89] D. J. Scalapino, *Rev. Mod. Phys.*, vol. 84, p. 1383, 2012.

[90] W. Kohn and J. M. Luttinger, *Phys. Rev. Lett.*, vol. 15, p. 524, 1965.

[91] J.-H. Chu, J. G. Analytis, K. De Greve, P. L. McMahon, Z. Islam, Y. Yamamoto, and I. R. Fisher, *Science*, vol. 329, p. 824, 2010.

[92] N. P. Armitage, P. Fournier, and R. L. Greene, *Rev. Mod. Phys.*, vol. 82, p. 2421, 2010.

[93] R. M. Fernandes, D. K. Pratt, W. Tian, J. Zarestky, A. Kreyssig, S. Nandi, M. G. Kim, A. Thaler, N. Ni, P. C. Canfield, R. J. McQueeney, J. Schmalian, and A. I. Goldman, *Phys. Rev. B*, vol. 81, p. 140501, 2010.

[94] E. McCann and M. Koshino, *Rep. Prog. Phys.*, vol. 76, p. 056503, 2013.

[95] J. Velasco Jr., L. Jing, W. Bao, Y. Lee, P. Kratz, V. Aji, M. Bockrath, C. N. Lau, C. Varma, R. Stillwell, D. Smirnov, F. Zhang, J. Jung, and A. H. MacDonald, *Nature Nanotechnology*, vol. 7, p. 156, 2012.

[96] W. Bao, J. Velasco, F. Zhang, L. Jing, B. Standley, D. Smirnov, M. Bockrath, A. H. MacDonald, and C. N. Lau, *Proc. Nat. Acad. Sci.*, vol. 109, p. 10802, 2012.

[97] A. S. Mayorov, D. C. Elias, M. Mucha-Kruczynski, R. V. Gorbachev, T. Tudorovskiy, A. Zhukov, S. V. Morozov, M. I. Katsnelson, V. I. Falko, A. K. Geim, and K. S. Novoselov, *Science*, vol. 333, p. 860, 2011.

[98] F. Zhang, H. Min, M. Polini, and A. H. MacDonald, *Phys. Rev. B*, vol. 81, p. 041402, 2010.

[99] R. Nandkishore and L. Levitov, *Phys. Rev. Lett.*, vol. 104, p. 156803, 2010.

[100] Y. Lemonik, I. L. Aleiner, C. Toke, and V. I. Fal'ko, *Phys. Rev. B*, vol. 82, p. 201408, 2010.

[101] O. Vafek and K. Yang, *Phys. Rev. B*, vol. 81, p. 041401, 2010.

[102] A. H. Castro Neto, F. Guinea, N. M. R. Peres, K. S. Novoselov, and A. K. Geim, *Rev. Mod. Phys.*, vol. 81, p. 109, 2009.

[103] M. Kharitonov, *Phys. Rev. B*, vol. 86, p. 195435, 2012.

[104] R. Nandkishore and L. Levitov, *Phys. Rev. B*, vol. 82, p. 115124, 2010.

[105] V. Cvetkovic, R. E. Throckmorton, and O. Vafek, *Phys. Rev. B*, vol. 86, p. 075467, 2012.

[106] L. M. Zhang, Z. Q. Li, D. N. Basov, M. M. Fogler, Z. Hao, and M. C. Martin, *Phys. Rev. B*, vol. 78, p. 235408, 2008.

[107] J. Nilsson, A. H. C. Neto, F. Guinea, and N. M. R. Peres, *Phys. Rev. B*, vol. 78, p. 045405, 2008.

[108] O. Vafek, *Phys. Rev. B*, vol. 82, p. 205106, 2010.

[109] R. E. Throckmorton and O. Vafek, *Phys. Rev. B*, vol. 86, p. 075467, 2012.

[110] J. Polchinski, *arXiv:9210046*, 1992.

[111] R. Shankar, *Rev. Mod. Phys.*, vol. 66, p. 129, 1994.

[112] P. Fulde and A. Ferrel, *Phys. Rev.*, vol. 135, p. A550, 1964.

[113] A. Larkin and Y. Ovchinnikov, *Sov. Phys. JETP*, vol. 20, p. 762, 1965.

[114] J. C. Wheatley, *Rev. Mod. Phys.*, vol. 47, p. 415, 1975.

[115] Y. Maeno, S. Kittaka, T. Nomura, S. Yonezawa, and K. Ishida, *J. Phys. Soc. Japan*, vol. 81, p. 011009, 2012.

[116] R. B. Laughlin, *Phys. Rev. Lett.*, vol. 80, p. 5188, 1998.

[117] V. Stanev and Z. Tešanović, *Phys. Rev. B*, vol. 81, p. 134522, 2010.

[118] S. Maiti and A. V. Chubukov, *Phys. Rev. B*, vol. 87, p. 144511, 2013.

[119] R. Nandkishore, L. S. Levitov, and A. V. Chubukov, *Nature Physics*, vol. 8, p. 158, 2012.

[120] J. Vučičević, M. O. Goerbig, and M. V. Milovanović, *Phys. Rev. B*, vol. 86, p. 214505, 2012.

[121] V. P. Mineev and K. V. Samokhin, *Introduction to Unconventional Superconductivity.* Gordon and Breach Science Publishers, 1998.

[122] S. Raghu, S. A. Kivelson, and D. J. Scalapino, *Phys. Rev. B*, vol. 81, p. 224505, 2010.

Vita

James Murray was born and raised in Montana, where he received a B. S. degree in Physics from Montana State University in 2006, which included a year of study at Eberhard–Karls Universität in Tübingen, Germany. He began his Ph.D. study at Johns Hopkins University in 2007, where his research focused on theoretical descriptions of quantum many-body phases of matter. He plans to begin work as a postdoctoral researcher at the National High Magnetic Field Laboratory in Tallahassee in Fall, 2013.